Radar-Based Investigation of Pulse Wave and Heart Sound Propagation

Master's Thesis in Medical Engineering

submitted
by

Marie Oesten

born 10.05.1997 in Ingolstadt

Written at

Machine Learning and Data Analytics Lab
Department Artificial Intelligence in Biomedical Engineering
Friedrich-Alexander-Universität Erlangen-Nürnberg (FAU)

in Cooperation with

Institute of High-Frequency Technology, Hamburg University of Technology (TUHH)
Department of Palliative Medicine, University Hospital Erlangen (UK)

Advisors: Luca Abel M. Sc., Robert Richer M. Sc., Prof. Dr. Bjoern Eskofier (FAU)
Nils Albrecht M. Sc., Prof. Dr. Alexander Koelpin (TUHH)
Stefan Grießhammer Dipl.-Ing., Dr. Tobias Steigleder (UK)

Started: 15.07.2023

Finished: 15.01.2024

Ich versichere, dass ich die Arbeit ohne fremde Hilfe und ohne Benutzung anderer als der angegebenen Quellen angefertigt habe und dass die Arbeit in gleicher oder ähnlicher Form noch keiner anderen Prüfungsbehörde vorgelegen hat und von dieser als Teil einer Prüfungsleistung angenommen wurde. Alle Ausführungen, die wörtlich oder sinngemäß übernommen wurden, sind als solche gekennzeichnet.
Die Richtlinien des Lehrstuhls für Bachelor- und Masterarbeiten habe ich gelesen und anerkannt, insbesondere die Regelung des Nutzungsrechts.

Erlangen, den 15.01.2024

Übersicht

Eine große Anzahl an Menschen weltweit leidet an Herz-Kreislauf-Erkrankungen, die eine ernsthafte Bedrohung für ihre Gesundheit darstellen. Das Herz generiert einen pulsierenden Blutfluss, der die Versorgung aller Organe sicherstellt. Die Bewertung von damit zusammenhängenden Signalen wie Pulswellen oder Herztöne ermöglicht Ärzten die Diagnose und Überwachung von Krankheiten. Aktuelle Goldstandardmethoden erfordern einen dauerhaften Hautkontakt, um Parameter wie die Herzfrequenz abzuleiten. Da die Anwendbarkeit kontaktbasierter Methoden in einer Vielzahl von medizinischen Anwendungen begrenzt ist, ist die Nachfrage nach kontaktlosen Methoden hoch. Die radarbasierte Überwachung von Vitalparametern ist ein Ansatz, der bereits intensiv erforscht wurde. Eine Vielzahl an Systemen und Verarbeitungstechniken wurde entwickelt, um die kontaktlose und kontinuierliche Überwachung der Herzfunktion zu ermöglichen. Diese Lösungen konzentrieren sich jedoch ausschließlich auf die Ableitung von Parametern von der Brustregion und untersuchen nicht die Ausbreitung kardialer Signale im Körper, obwohl diese das Potenzial haben, wertvolle Informationen über den aktuellen Zustand eines Patienten zu liefern.

Um die Erkenntnisse über die mittels Radar Technologie erfasste Ausbreitung von Pulswellen und Herztönen im Körper zu erweitern, wurde eine Studie mit 22 jungen und gesunden Probanden durchgeführt. Gleichzeitige globale und lokale Signalaufnahmen wurden an elf arteriellen Messstellen am gesamten Körper durchgeführt, die mithilfe von Landmarken oder Ultraschall identifiziert wurden. Globale Referenzaufnahmen umfassten das Elektrokardiogram für die elektrische Aktivität und das Impedanzkardiogram für die Atmung. An jedem der ausgewählten Messorte wurden lokale Radar sowie Photoplethysmogram und Phonokardiogram Aufnahmen als Referenzen für Pulswellen und Herztöne durchgeführt. Nach Anwendung von Signalverarbeitungstechniken wurden die Formen von Radar- und Referenzdaten durch visuelle Inspektion analysiert. An allen Messstellen wurden in beiden Modalitäten periodische und charakteristische Formen identifiziert. Wegen verschiedener Unstimmigkeiten in den Pulswellen Daten wurden diese nicht weiter ausgewertet. Da die Herztöne davon nicht betroffen waren, wurden zeitliche und morphologische Merkmale extrahiert, um ihre Ausbreitung zu analysieren.

Die Ergebnisse betonen, dass Unterschiede zwischen Körperregionen beobachtet werden können. Nicht nur der Zeitpunkt des Auftretens unterscheidet sich, sondern auch Konfigurationsparameter wie Amplitude und Dauer hängen von der gemessenen Region ab. Durch eine Erweiterung dieses Ansatzes könnten Radar Systeme zu einem vielversprechenden Werkzeug für die berührungslose Bewertung des kardiovaskulären Zustands eines Patienten werden. Zusammenfassend stellt diese Arbeit die radarbasierte Detektion von Pulswellen und Herztönen an peripheren Körperstellen vor und liefert erste Einblicke in die Ausbreitung der Herztöne im gesamten Körper.

Abstract

A large number of people around the world suffer from cardiovascular diseases, which pose a serious threat to their physiological well-being. Throughout the cardiac cycle, the heart generates a pulsatile blood flow that ensures the supply of all organs and tissues. Assessing related signals, such as pulse waves (PWs) or heart sounds (HSs), enables physicians to diagnose and monitor diseases and their progression. Current gold standard methods require permanent contact with the patient's skin to derive parameters such as heart rate (HR) or breathing rate (BR). Since the usability of contact-based methods is limited in a wide range of medical applications, the demand for contactless methods is high. Radar-based vital sign monitoring is one solution that has been intensively investigated in the last four decades. A large number of systems and processing techniques were developed to allow the contactless and continuous monitoring of the cardiac function. However, these solutions are solely focused on deriving parameters from the chest region and do not investigate the propagation of cardiac signals in the body, despite their potential in providing valuable information about a patient's current status.

To enhance the knowledge about radar-sensed PW and HS propagation within the body, a study was conducted with 22 young and healthy participants. Simultaneous global and local signal recordings were performed at 11 arterial measurement sites across the whole body, identified using landmarks or ultrasonography. Global reference recordings included the electrocardiogram (ECG) for electrical activity and the impedancecardiogram (ICG) for respiration. At each selected measurement location, local radar recordings, as well as photoplethysmogram (PPG) and phonocardiogram (PCG) as references for PWs and HSs recordings, were conducted. After applying signal processing techniques, the radar and reference PW and HS shapes were analyzed through visual inspection. At all sites, periodic and characteristic shapes were identified in both modalities. However, the PW data presented several discrepancies and were, therefore, not further evaluated. Since the HSs were not affected, temporal and morphological features were extracted to assess their propagation within the human body.

The results emphasize that differences between body locations can be observed. Not only does the timing of occurrence differ between body regions, but configuration parameters such as amplitude and duration also depend on the measured region of interest. By expanding on this work, radar technology may become a promising tool for the comprehensive, contactless assessment of a patient's cardiovascular state. In summary, this work introduces the radar-based detection of PWs and HSs at peripheral body locations and provides initial insights into HS propagation throughout the entire body.

Contents

Chapter 1

Introduction

Aging populations worldwide are contributing to an increasing number of people suffering from cardiovascular diseases [Nag15; Rot18]. The term cardiovascular disease comprises a group of disorders affecting the heart and blood vessels, with risk factors contributing to their development and progression [Mil90]. For instance, elevated blood pressure (BP), recognized as a predominant risk factor [Mur20], can induce arterial wall stiffening leading to an increased workload for the heart, which may contribute to the development of heart failure [Bra19]. The heart is a central organ in the human organism, that generates with each contraction a mechanical PW that propagates through the vessels and supplies all organs with oxygen and nutrients [Bra19].

A variety of diagnostic tools is available for the detection, diagnosis, and monitoring of cardiovascular disorders. While auscultation enables the identification of heart valve malfunctioning and carotid artery stenosis based on sound assessment [Kah18], arterial stiffness is evaluated by measuring the PW transition time between two vessels [Lau06]. Another tool is the ECG, which not only enables the detection of cardiac arrhythmias or heart attacks [Bra19] but also plays a crucial role in vital sign monitoring. In vital sign monitoring several parameters such as HR and BR are continuously extracted from physiological signals acquired through sensors to evaluate a patient's health status [Eva01]. Analyzing trends in these parameters [Chu16] and calculating early warning scores, enables the identification of patients at risk for deterioration and the initiation of timely interventions [Bun19].

Current gold standard methods demand permanent skin contact and wiring to diagnostic machines. Besides the evident limitations on patient autonomy and participation in daily activities, contact-based methods encounter several challenges. While electrodes may cause skin irritations in long-term measurements [Wu21], sensor placement for patients with burns can be challenging or even impossible [Gar24]. Furthermore, the workload for nurses is aggravated not only by the

sensor attachment itself, but also by the necessity to respond frequently to false alarms, due to the high incidence of contact and transmission issues [Dur20]. Given these restrictions, it is evident that the demand for innovative vital sign monitoring approaches, also to enable its application on general wards [McG16] or in home care scenarios [Mar06], is high.

One potential solution which has been extensively researched for the last four decades, is vital sign monitoring using radar systems [Pat23]. Leveraging the body's ability to reflect electromagnetic waves due to its electrical conductivity, radar systems analyze the distance between the antenna and the body surface. As the distance is modulated by both respiration movements and vibrations from heart activity, this approach offers to simultaneously evaluate multiple physiological signals in a contactless manner. The primary focus in this research area is the development of systems and algorithms to robustly extract parameters such as HR and BR from signals acquired at the chest region [Pat23]. Consequently, limited insights currently exist regarding the radar-sensed PW and HS propagation, despite their potential in providing valuable physiological information.

Therefore the objective of this master's thesis is to extend the knowledge about radar-sensed PW and HS propagation within the human body. In the scope of this work, a study with healthy and young participants was conducted as part of the EmpkinS collaborative research center [Emp23]. Radar recordings were performed at distinct locations across the body, alongside concurrent measurements of PPG as reference for PWs and PCG as reference for HSs. Simultaneously, ECG served as reference for heart activity, and ICG was recorded for respiratory assessments. Using this multimodal dataset, the feasibility of detecting cardiac activity at peripheral body locations using radar was analyzed. If feasible, morphological and temporal properties among measurement locations were investigated to derive descriptive parameters capable of effectively characterizing the observed alterations.

This thesis is structured as follows: Chapter 2 provides the necessary medical and technical background, covering the fundamentals of cardiovascular physiology and radar systems. In Chapter 3, relevant research in the domains of PW and HS propagation, as well as radar-based vital sign detection, is presented. While Chapter 4 outlines the data acquisition process and describes the methods used for propagation assessment, Chapter 5 presents and analyzes the obtained results. The thesis concludes with Chapter 6, in which the findings are summarized and an outlook about future work is provided.

Chapter 2

Background

2.1 Cardiovascular Physiology

2.1.1 Cardiovascular System

The primary function of the cardiovascular system is the distribution of oxygen and nutrients to all organs and the removal of metabolic waste products. Blood as the medium of transportation is pumped through the blood vessels of the circulatory system by the heart. Comprising two separate intermittent pumping systems, the heart's left and right sides consist of two chambers, the atrium and ventricle, which are connected by atrioventricular valves. The right heart directs deoxygenated blood into the pulmonary circulation, while the left heart propels oxygenated blood returning from the lungs into the arteries of the systemic circulation. From the peripheral organs and tissues, the blood is propagated back to the right heart through the veins. Both cardiac systems are connected to the respective arteries by semilunar valves, which prevent the backflow of the blood. A schematic overview of the heart's anatomy and blood flow can be found in Figure 2.1. [Mil90; Lev13; Ste14]

The heart's rhythmic contractions are regulated by an electrical conduction system, comprising a network of specialized cells and pathways. The Sinoatrial node, located in the right atrium, operates as a pacemaker, initiating a stimulus that propagates through the atria to the Atrioventricular node. From there, the Bundle of His transmits the signal to the Purkinje fibers that rapidly distribute the impulse throughout the ventricles, ensuring a synchronized mechanical muscle contraction. Whereas the phase characterized by muscle contraction and blood ejection is called systole within the cardiac cycle, the subsequent time of muscle relaxation and refilling of the ventricles is called diastole. [Mil90; Ste14]

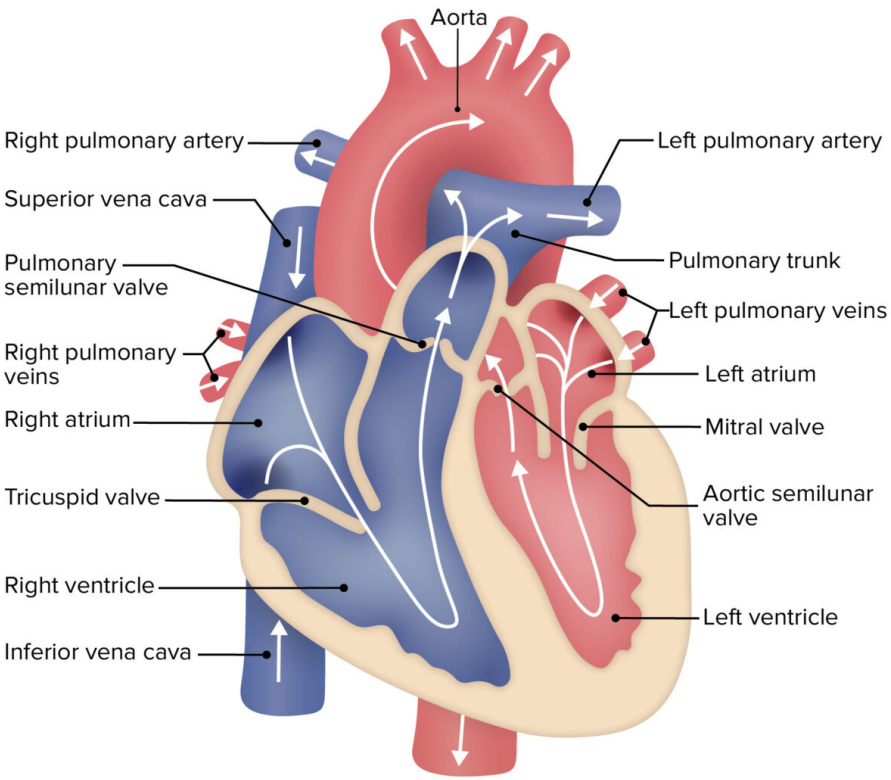

Figure 2.1: Schematic representation of the anatomy of the human heart and the blood circulation throughout the cardiac cycle [Lec23]

With the systolic ejection into the aorta, the left ventricle initiates a convective transport of oxygen and nutrients to all the organ regions through the branching of the aorta into arteries. High BP with an average arterial pressure of ≈ 85 mmHg prevails both in the aorta and in the arteries, which ensures adequate blood flow in the organs. On the organ level, arteries further branch into arterioles, increasing the number of vessels and the collective diameter while decreasing individual vessel diameter. Arterioles regulate organ blood flow through active diameter adjustments, leading to a change in local resistance and a distinct drop in BP and blood flow velocity. Subsequently, the exchange of substances through diffusion between blood and organs takes place in the capillaries at an average pressure of ≈ 20 mmHg. The decline in pressure continues within the capillaries, reaching an average of ≈ 5 mmHg in the veins. Functioning as an expandable blood reservoir, the veins collect and return blood to the right atrium by converging into vessels with an increasing diameter. With a decreasing diameter, the vessels oppose the blood with a resistance to flow. The total peripheral resistance (TPR), the sum of all resistances in the circulatory system, is generated by approximately half from terminal arteries and arterioles as well as by a quarter from

the capillaries. Since the blood vessels are exposed to different pressures and are designed for different functions, varying vessel wall thickness and composition are observed. In large vessels, elastic and firm connective tissue predominate, while arterioles feature a high proportion of smooth muscle cells. In a clinical context, the ability of individual blood vessel sections or the entire vascular system to expand is characterized by compliance C

$$C = \frac{\Delta V}{\Delta P} \tag{2.1}$$

where ΔV depicts a change in volume and ΔP a change in pressure. Within the arterial system, the aorta shows the highest compliance. [Bra19; Ste14]

2.1.2 Pulse Wave Generation and Propagation

In each cardiac cycle, the ejection of the stroke volume induces the acceleration of blood and a subsequent increase in pressure within the initial segment of the aorta. Due to its high proportion of elastic fibers, the volume can be partially stored in a local widening of the cross-section. This so-called Windkessel effect thereby reduces the pressure increase in the vessel. The local pressure gradient along the vessel causes a time-delayed acceleration and movement of the stored blood volume. This concurrent storage and release of blood generate PWs, which propagate throughout the vascular system into the capillaries. Figure 2.2 illustrates the fundamental principle of PW propagation in the arterial system. [Bra19; Vla11]

At each location along the vascular system, the PW manifests as pressure pulse, flow pulse, and cross-section pulse. In a unidirectional PW system, these three pulses maintain consistent shapes. In the arterial system, this uniformity is disrupted due to wave reflections induced by changes in wave resistance. Variations in vessel diameter, wall thickness, or elasticity alter the wave resistance, causing PWs to be reflected at points of increased wave impedance. The reflection results in a superposition of peripherally and centrally propagating waves leading to an increase in the pressure pulse amplitude and a reduction of the flow pulse amplitude in peripheral pulses. Consequently, this phenomenon leads to a two-peak PW for peripheral pressure pulses. [Bra19]

Depending on arterial properties such as stiffness and filling status, PWs propagate with different velocities. In an adolescent, the pulse wave velocity (PWV) ranges from 4 to $6\,\mathrm{m\,s^{-1}}$ in the aorta, approximately $7\,\mathrm{m\,s^{-1}}$ in the femoral artery, and about 9 to $10\,\mathrm{m\,s^{-1}}$ in the tibial artery. These velocities are notably higher than the average blood flow velocity, which typically ranges from 0.15 to $0.20\,\mathrm{m\,s^{-1}}$ and can reach a maximum of $1.20\,\mathrm{m\,s^{-1}}$. [Bra19]

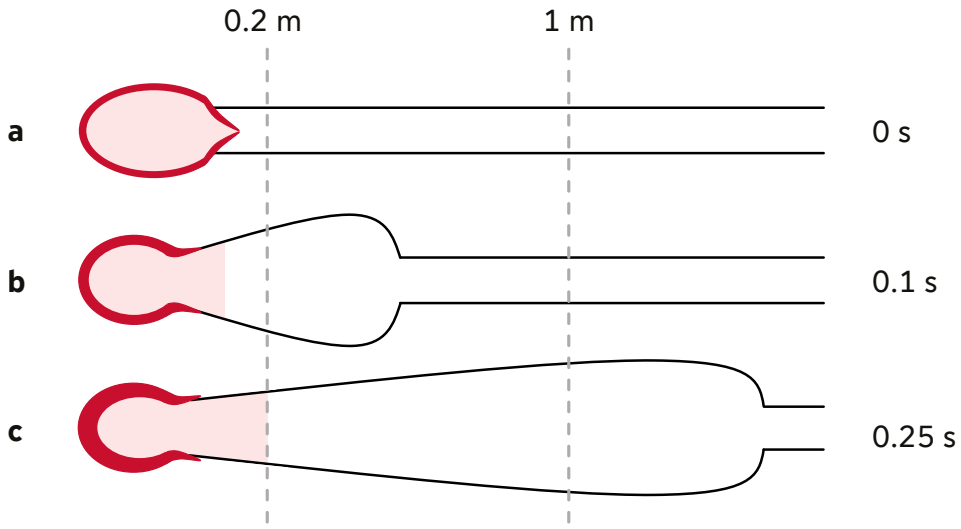

Figure 2.2: Schematic representation of the PW propagation in the arterial system (modified from [Bra19]); a: immediately before the beginning of the systole; b: $0.1\,\mathrm{s}$ after the beginning of the systole; c: $0.25\,\mathrm{s}$ after the beginning of the systole. Marked in light red is the blood volume ejected in the current stroke.

2.1.3 Biomedical Signals

Electrocardiogram

The ECG is a widely employed, non-invasive procedure for evaluating the heart's electrical activity. By placing electrodes typically on the chest, arms, and legs, a comprehensive set of views on the heart vector can be generated using 12 leads. The leads include three bipolar limb leads (I, II, III) by Einthoven, three augmented unipolar limb leads (aVR, aVL, aVF) devised by Goldberger, and six unipolar precordial leads (V1 to V6) by Wilson. [Ger07]

Figure 2.3 illustrates a schematic representation of Einthoven's lead II alongside the ECG nomenclature. The distinct waveforms observed in an ECG directly correspond to specific phases within the cardiac cycle. While the P-wave marks atrial depolarization, signifying the propagation of the electrical impulse across the atria, the QRS-complex reflects the ventricular depolarization, indicating the rapid and synchronized activation of the ventricular muscle. During the T-wave the ventricle repolarizes, preparing the heart muscle for the next cardiac cycle. Although the origin of the U-wave is not fully understood yet, it is assumed that it is linked to the repolarization of the Purkinje fibers. Analyzing the shapes, timings, and intervals between the waves, offers valuable insights for diagnosing heart diseases or abnormalities of its conduction system. [Ger07]

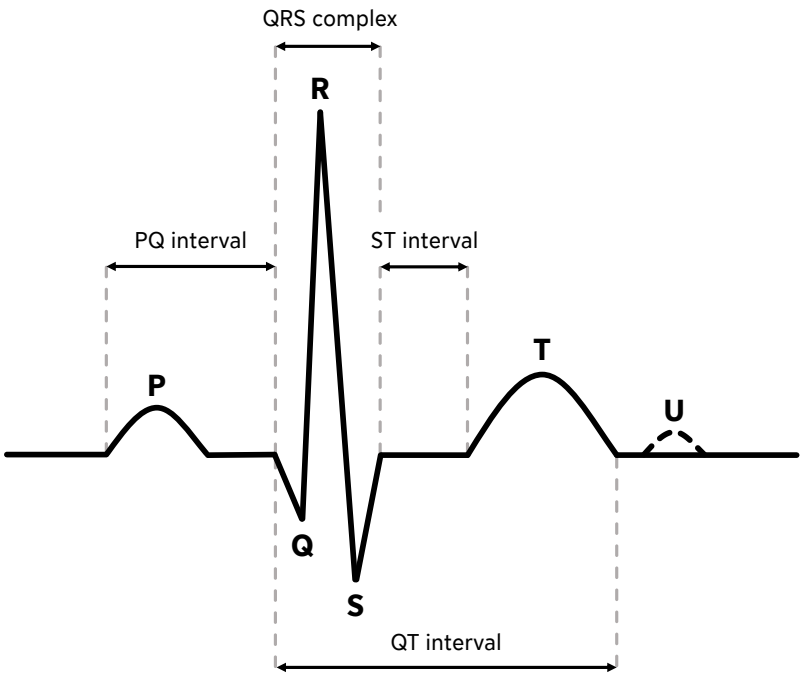

Figure 2.3: Schematic representation of an ECG according to Einthoven's lead II (modified from [Ger07])

Photoplethysmogram

Another non-invasive method for evaluating the cardiovascular system is the PPG. By leveraging the human body's optical characteristics, the PPG measures alterations in blood volume within the skin's microvascular bed by recording the intensity of transmitted or reflected light. A typical PPG device consists of a light-emitting diode (LED) and a photodetector, with the latter capturing the light emitted by the LED. In transmissive-mode PPG, the LED and the photodetector are placed on opposite sides of the tissue of interest, establishing a straight optical pathway. To access pulsatile arteries which are found in the dermis or subcutaneous tissue, PPG devices primarily employ red wavelengths (640 to 660 nm) and infrared wavelengths (880 to 940 nm). The measured transmitted light intensity I follows Beer-Lambert law, expressed as

$$I = I_0 \cdot e^A, \tag{2.2}$$

where the initial light intensity I_0 is attenuated due to the total absorbance A. As the light traverses through skin components like arteries, veins, and tissues, A is dependent on the distinct properties of each layer. This dependence is modeled as $A = \sum(-\varepsilon_k \cdot l_k \cdot c_k)$, with ε_k representing the absorption coefficient, l_k the optical path length, and c_k the medium's concentration in the k_{th}

layer. In reflective-mode PPG, both the LED and the photodetector are positioned on the same side. Consequently, the optical pathway becomes nonlinear, necessitating a more complex physical model, which is not covered in this context. [Par22]

The PPG waveform delineates into non-pulsatile and pulsatile components, as depicted in Figure 2.4 a. The non-pulsatile section encompasses elements beyond pulsatile arterial blood and is influenced by factors such as tissue composition and ambient light. The pulsatile component is synchronized with the cardiac cycle and affected by aspects like blood volume and arterial diameter. Consequently, in the diastolic phase, the blood's optical density is minimized, resulting in maximum measured light intensity, and vice versa in the systolic phase. Inverting intensity values produces a distinctive PPG waveform, as shown in Figure 2.4 b, which can be divided at the dicrotic notch in a systolic and diastolic phase. The dicrotic notch and the diastolic peak are a result from the superposition of the forward and reflected PWs. [Par22; Loh22]

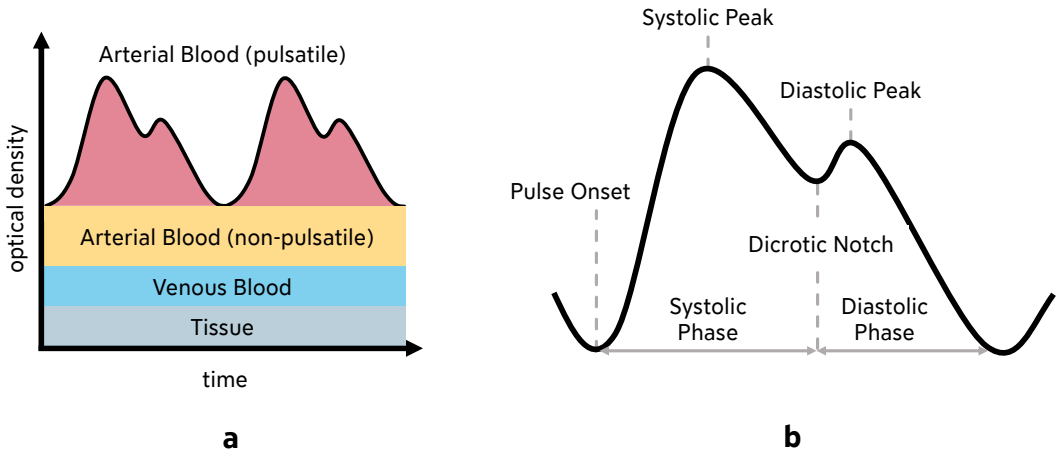

Figure 2.4: Schematic representations of a: the non-pulsatile and pulsatile components of a PPG (modified from [Loh22]); b: the PPG waveform (modified from [Par22])

Phonocardiogram

The mechanical activity of the heart during the cardiac cycle generates vibrations transmitted through the heart and arteries to the chest wall. In clinical examinations, healthcare professionals employ a stethoscope to analyze these HSs at distinct auscultation areas on the chest. An alternative method for detecting the sounds is through the use of a PCG, which utilizes a microphone to record the vibrations. [Bra19; Lev13]

In healthy adults, two primary HSs are commonly observed. The first HS (S1), associated with the contraction of the ventricular muscle and the closure of the atrioventricular valves, marks the beginning of ventricular systole. It is physiologically split, with the mitral valve closing slightly before the tricuspid valve. Due to the very brief time interval between these components, the split can not be perceived with the stethoscope. The second HS (S2) is related to the closure of the semilunar valves, denoting the end of systole. This sound exhibits physiological splitting during inspiration, resulting in an aortic and a slightly delayed pulmonary component. S1 and S2 as well as their relation to the ECG is depicted in Figure 2.5. Additional HSs, such as S3 and S4, have clinical relevance. S3, manifesting in early diastole and linked to rapid ventricular filling, is common in adolescents but may indicate ventricular dilation in adults. S4, occurring in the latter part of diastole and related to atrial systole, is observed when there is a decrease in ventricular compliance, as evident in cases of ventricular hypertrophy. [Lev13; Kla11]

HSs also play a crucial role in identifying cardiovascular valve defects. The two fundamental types stenosis, constriction of the valve requiring higher pressure for blood flow, and insufficiency, lacking complete closure resulting in a blood backflow, cause a high-frequency vibration, that can be heard as heart murmur. [Lev13]

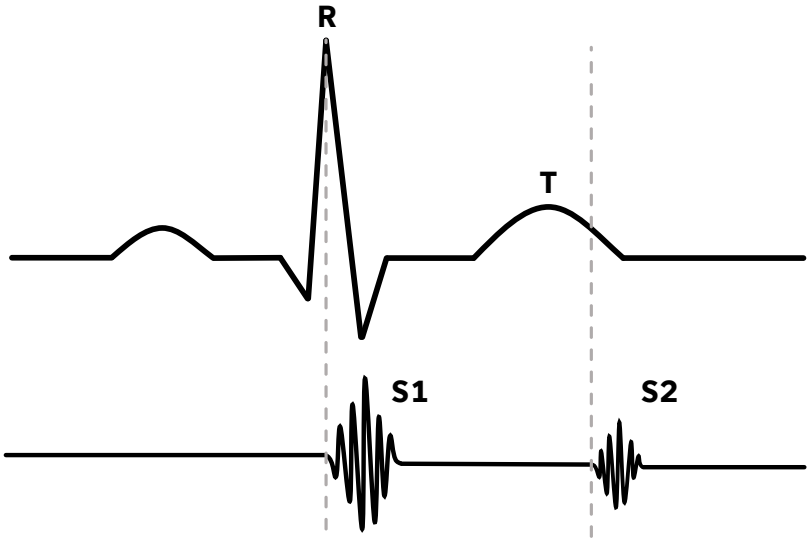

Figure 2.5: S1 and S2 HSs in relation to ECG (modified from [Fra14])

Impedancecardiogram

The ICG is a non-invasive approach for assessing cardiac mechanical function by measuring changes in electrical impedance across the thorax. Its measurement principle relies on Ohm's law. An ICG device induces an alternating current with a constant magnitude along the thorax, achieved through electrodes placed at the neck and chest. Simultaneously recording the voltage using an additional set of electrodes allows the computation of impedance. Given that blood serves as an electrical conductor, the increase in blood volume with each heartbeat induces detectable changes in the thoracic impedance. Since the impedance is also influenced by breathing, the ICG allows for deriving cardiac parameters such as cardiac output and systemic vascular resistance, as well as parameters related to respiration. [Kub70; She90; Wol97]

2.2 Radar Systems in Vital Sign Monitoring

A system designed for radio detection and ranging (RADAR), in the following referred to as radar system, is an electronic system that allows for determining the frontal distance as well as the velocity of targets in the context of a single-input-single-output (SISO) system. In the case of a multiple-input-multiple-output (MIMO) system, it also supports the estimation of angular coordinates. The operational principle of the radar system relies on the capability of targets to reflect the electromagnetic waves generated by the system, facilitated by their electrical conductivity. Every radar system is composed of two essential components: a transmitter and a receiver. While the transmitter is responsible for generating radio waves with known properties and directing them along a predefined path using a TX antenna, the receiver detects the reflected waves using a RX antenna. When employing a SISO radar system, the system is equipped with single TX/RX antennas. In contrast, a MIMO system is assembled by antenna arrays. Radar systems that are used in the context of vital sign monitoring operate in the microwave spectrum, especially from 1 to 100 GHz. [Pat23]

Radar systems applied in vital sign monitoring operate under the assumption that the electromagnetic waves reflected from an individual's chest undergo modulations due to quasi-periodic vibrations caused by respiration and heart activity. Consequently, the displacement of the chest, denoted as $\Delta R(t)$ and observed under minimal physical movements, can be expressed as Equation 2.3. [Nos19; Pat23]

$$\Delta R(t) \widehat{=} R(t) - R_0 = \delta_b(t) + \delta_h(t) \tag{2.3}$$

In this context, $R(t)$ symbolizes the distance between radar and chest at time t, while R_0 denotes the distance offset, representing the distance in the absence of respiration and heart activity [Pat23]. The terms $\delta_b(t)$ and $\delta_h(t)$ characterize the impact of respiration and heart activity on $\Delta R(t)$. It is assumed, that both $\delta_b(t)$ and $\delta_h(t)$ vary periodically with periods T_{BR} and T_{HR}, respectively, with $T_{BR} > T_{HR}$. Compared to $\delta_b(t)$, the influence of $\delta_h(t)$ on $\Delta R(t)$ is typically small, with $\delta_b(t)$ ranging from 4 to $12\,\text{mm}$ [Kon97] and $\delta_h(t)$ ranging from 0.2 to $0.5\,\text{mm}$ [Ram89].

Radar systems can be categorized based on the mechanism used for waveform generation, distinguishing between continuous wave (CW) and pulsed radars. In CW radar systems, the signal is continuously transmitted, while in pulsed systems, signals are radiated over short periods of time. Regardless of the mechanism chosen, the transmitted signal can be either modulated or unmodulated. [Pat23]

One frequently utilized architecture for monitoring vital signs is the CW Doppler radar, operated as SISO system [Li13; Lin14]. Within this approach, the transmitted electromagnetic waves remain unmodulated and are characterized by a defined stable carrier frequency, denoted as f_0. The chest movement induces phase variations in the reflected wave, allowing for the displacement calculation by demodulating the phase shift between the transmitted and received signals. All CW Doppler systems are structured according to the generic principle in Figure 2.6. The transmitter generates

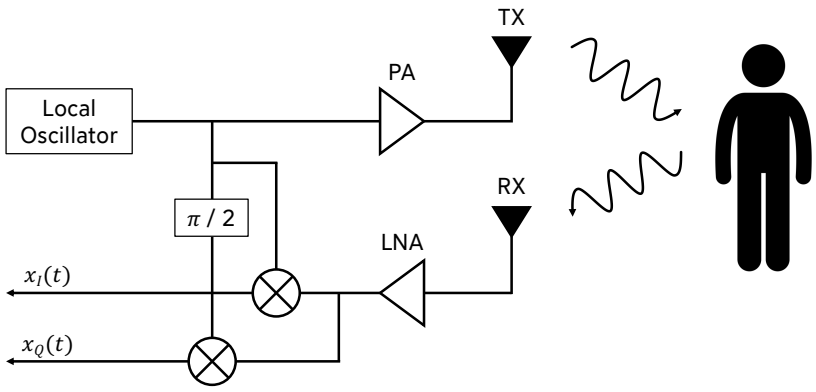

Figure 2.6: General setup of a CW Doppler radar (modified from [Pat23])

a radio-frequency signal through a local oscillator. This signal undergoes amplification using a power amplifier (PA) and is directed towards the human chest by the TX antenna. Upon reflection and reception by the RX antenna, the signal is amplified using a low noise amplifier (LNA). Subsequently, mixers extract its in-phase (I) and quadrature (Q), denoted as $x_I(t)$ and $x_Q(t)$. These signals are filtered separately through a lowpass filter, followed by further amplification using a voltage gain amplifier. Finally, the signals are sampled by an analog-to-digital converter

operating at frequency $f_S = \frac{1}{T_S}$, where T_S represents the sampling period. The quantified I and Q components are expressed as $x_I[n] \mathrel{\widehat{=}} x_I(nT_s)$ (Equation 2.4) and $x_Q[n] \mathrel{\widehat{=}} x_Q(nT_s)$ (Equation 2.5), respectively. In these equations, a denotes the signal amplitude and $w_I[n]$ and $w_Q[n]$ the additive

$$x_I[n] = a\cos\left(\psi[n]\right) + w_I[n] \qquad (2.4) \qquad\qquad x_Q[n] = a\sin\left(\psi[n]\right) + w_Q[n] \qquad (2.5)$$

white Gaussian noise, impacting the respective component. $\psi[n]$ (Equation 2.6) represents the phase information, comprised by the constant phase shift ψ_0 (Equation 2.7), resulting from the (constant) distance R_0 between radar and target, and phase variation $\Delta\psi[n]$ (Equation 2.8), resulting from the displacement $\Delta R(t = nT_s)$ (Equation 2.3). $\lambda = c/f_0$ denotes the signal's wavelength, with c being the speed of light. Based on that, evaluating the phase variations of the

$$\psi[n] \mathrel{\widehat{=}} \psi_0 + \Delta\psi[n] \qquad (2.6)$$

$$\psi_0 = 4\pi\frac{R_0}{\lambda} \qquad (2.7)$$

$$\Delta\psi[n] = 4\pi\frac{\Delta R[n]}{\lambda} \qquad (2.8)$$

complex sequence $x[n]$ (Equation 2.9) allows the estimation of the chest displacement, where $w[n]$ (Equation 2.10) denotes the noise component. [Pat23]

$$x[n] \mathrel{\widehat{=}} x_I[n] + jx_Q[n] = a\exp\left(j\psi[n]\right) + w[n] \qquad (2.9)$$

$$w[n] \mathrel{\widehat{=}} w_I[n] + jw_Q[n] \qquad (2.10)$$

Chapter 3

Related Work

The natural aging process as well as pathological conditions contribute to the loss of elastic fibers in the arterial wall, leading to a reduction of arterial compliance. Consequently, there is an elevation in the pressure load on the heart and the PW propagation velocity. Since PWs carry valuable information about the system they traverse, evaluating their properties allows for drawing conclusions about a person's health status. [Bra19]

Pulse Wave Propagation

The carotid-femoral pulse wave velocity (cfPWV) is considered the gold standard for assessing arterial stiffness [Lau06] and is recommended as a marker for risk stratification in cardiovascular mortality by the task force of the management of arterial hypertension [Man13]. Measured as the distance and transit time delay between the feet of the right common carotid artery and the right femoral artery waveforms [Lau06], it provides information across a long segment of the arterial tree, encompassing arteries with different biomechanical characteristics [Her07].

Given that routine clinical cfPWV measurements have been considered impractical, Yao et al. investigated estimating cfPWV through a single radial PW measurement. They recorded the radial waveform using a sphygmomanometer, extracting features in both the time and frequency domains, as well as through wave separation analysis. Employing several regression approaches on these features, they obtained correlation coefficients between the measured and estimated cfPWV equal to or greater than 0.8. [Yao22]

Apart from impracticality concerns, the cfPWV method has faced criticism for its inability to assess the properties of a small segment or determine the position of arterial abnormalities [Dar15]. To address these challenges, various methods have been developed to explore the potential of local PWV measurement, focusing on a short segment of a single artery [Nab20; Per15].

A study by Wang et al. compared ultrasonography-based local PWV measurements at the left common carotid artery of hypertensive patients and an age- and gender-matched healthy control group. The results revealed a significantly higher PWV in hypertensive patients ($6.29 \pm 1.04\,\mathrm{m\,s^{-1}}$) than in the control group ($5.31 \pm 0.72\,\mathrm{m\,s^{-1}}$), with a p-value of 0.019. [Wan15]

Van der Meer et al. utilized magnetic resonance velocity mapping at two predefined positions in the ascending and abdominal aorta to determine the PWV. They compared the values of a group consisting of patients with well-controlled and uncomplicated type 2 diabetes mellitus to those of a group comprising age- and gender-matched healthy subjects. Their findings showed a significantly higher mean PWV in the diabetic group ($6.83 \pm 1.60\,\mathrm{m\,s^{-1}}$) than in the healthy controls ($5.65 \pm 0.75\,\mathrm{m\,s^{-1}}$), with a p-value less than 0.05. [Van07]

Besides the PWV assessment, PW propagation analysis can provide additional insights. Allen et al. conducted PPG recordings at ears, thumbs, and big toes on both sides of the body, aiming to assess the left-right PW characteristics. Analyzing the pulse waveforms using root mean square error (RMSE) and cross-correlation, healthy subjects exhibited low RMSE and high correlations (> 0.98) between both body halves. In contrast, a patient with an occlusion of the left iliac artery showed higher RMSE and lower right-to-left correlation between the PPG waveforms measured at the toes, indicating differences in pulse shape and timing. This approach can identify asymmetric vascular diseases and detect deviations from normal pulse shape even in cases of similar left and right abnormalities. [All00]

Radar-based Pulse Wave and Heart Sound Detection

In a recent study, Will et al. introduced HS detection using radar technology [Wil18]. Their method involved comparing higher frequency components of the radar signal with reference PCG and ECG signals, revealing a significant correlation in morphology and timing of occurrence. Utilizing a dataset encompassing measurements at multiple thoracic sites and both common carotid arteries [Shi20b], the researchers not only identified HSs at the thorax but also successfully detected them at the neck, measuring an amplitude within the micrometer range. This observation is feasible due to the underlying principle, that HSs propagate as transverse vibrations of the arterial and ventricular wall, rather than solely as acoustic waves [Far63; Fab64]. Faber et al.'s experiments revealed an analogy between HS transmission and PW propagation in arteries. They measured an average HS propagation velocity of $5.7\,\mathrm{m\,s^{-1}}$ in the thoracic aorta, a value approximately matching the PWV in this segment.

Despite recent advancements, CW radar systems still encounter several challenges in extracting cardiac and respiratory information from the acquired signals [Keb20]. For instance, random body movements cause signal artifacts, thereby influencing robust vital sign detection [Her22]. One approach aimed at addressing this challenge within a continuous in-bed monitoring setup is the work by Schellenberger et al. [Sch20a]. Their two-step process initially detected the presence of the patient and categorized the movements. Subsequently, vital sign parameters were extracted from sections where the patient remained calm. Additionally, the extraction of actual parameters poses challenges. Many studies rely on the Fast Fourier Transform as the fundamental algorithm [Has22]. However, this approach faces drawbacks, such as the lengthy observation window and the inability to analyze signals on a beat/breath level. To overcome these limitations, various approaches have been developed. Will et al., for instance, employed multiple heterogeneous templates, determining the appropriate template type through prior feature extraction [Wil17b]. In a follow-up work, they applied a logistic regression hidden semi-Markov model (HSMM) to divide the HS signal into the phases of the cardiac cycle [Wil18]. Their results implicated, that the detection of HSs contributes to improving radar-based heartbeat monitoring. Building on this, Shi et al. devised an approach that segmented HSs using a Long Short-Term Memory architecture [Shi19].

The predominant focus in this research field revolves around the development of systems or algorithms dedicated to extracting vital information from a person's chest [Vin13; Shi18; Mic19; Sch20b]. However, by examining and comparing signals obtained from different locations on the human body, locally specific characteristics were explored. Will et al.'s work concentrated on examining the PW shapes at carotid, venous, and ventricle locations, demonstrating that a radar system can capture diverging signal shapes [Wil17a]. Furthermore, in the research performed by Shi et al. [Shi20b] and Will et al. [Wil18] based on a dataset measuring HSs at multiple thoracic sites and both common carotid arteries, various aspects of HS characteristics were identified. In terms of amplitude, they observed a general pattern that the amplitude of S1 was typically larger than that of S2. At specific locations, such as the carotid artery and the second intercostal space on the right side, i.e. when measuring closer to the aortic and pulmonary valves than to the ventricle muscle, they noted the amplitude of S2 exceeding that of S1. Additionally, they identified the inspiration-induced S2 split and observed a decrease in amplitude changes between heartbeats during breath holding. Regarding the HS timing compared to ECG reference points, the intervals between R-peak and S1, as well as T-peak and S2, were larger at the carotid artery than at the thorax, with a more pronounced increase between R-peak and S1. Despite these variations, all positions generally allowed for good measurability of HSs, although measurability can vary between people due to differences, for instance, in anatomy and fat distribution.

Chapter 4

Methods

4.1 Data Acquisition

To investigate PW and HS propagation in the human body using radar technology, a study was conducted in November 2023 as part of the EmpkinS collaborative research center [Emp23].

4.1.1 Study Population

A total of 22 participants (11 female, 11 male) were recruited for the study. Demographic and anthropometric data of the study participants are presented in Table 4.1.

Table 4.1: Demographic and anthropometric data of the study participants (Mean ± SD)

	Age [years]	**Height** [cm]	**Weight** [kg]	**BMI** [kg/m^2]
Female	24.36 ± 1.80	168.09 ± 5.54	66.58 ± 5.68	23.61 ± 2.25
Male	25.00 ± 2.68	181.91 ± 7.25	76.62 ± 10.51	23.14 ± 2.86
All	24.68 ± 2.25	175.00 ± 9.47	71.60 ± 9.71	23.37 ± 2.52

Participants were recruited through electronic flyers distributed via social media platforms among students. Their eligibility for study participation was determined by asking them to complete a screening questionnaire before the study. Exclusion criteria comprised an age or Body-Mass-Index (BMI) below 18 and above 30 as well as being diagnosed with a cardiovascular disease. All participants were remunerated with 75 € for their involvement in the study.

4.1.2 Measurement Locations

Eleven locations, illustrated in Figure 4.1, were chosen for PW and HS measurements according to the following criteria. Firstly, the total coverage of the body was prioritized over a high level of granularity. Therefore the measurement points were distributed across all body regions. Furthermore, since PWs and HSs propagate along arteries, it was presumed that measurements above arteries exhibit a higher Signal-to-Noise Ratio (SNR). Consequently, only arteries were selected as measurement locations and larger arteries were preferred over small ones. As overlying tissue was suspected to influence the signal, the distance between the artery and body surface was attempted to keep as small as possible. Lastly, the accessibility by radar technology was taken into consideration when selecting locations. All points, with the exception of those at the aorta, were consistently situated on the right side of the body. The measurement point in the Ao. proximalis was specifically designated as the auscultation area at the third intercostal space parasternal left, commonly known as Erb's point, where valves are perceived with equal intensity [Kah18].

In accordance with the direction of blood flow, the measurement locations were categorized into three groups: head and neck, upper extremity, as well as trunk and lower extremity, as described in Table 4.2.

Table 4.2: Group definitions of measurement locations

Group	Measurement Locations
Head, Neck	A. temporalis, A. carotis communis
Upper Extremity	A. brachialis, A. radialis proximalis, A. radialis medialis
	A. radialis distalis
Trunk, Lower Extremity	Ao. proximalis, Ao. medialis, Ao. distalis
	A. poplitea, A. dorsalis pedis

4.1.3 Measurements

Reference Measurements

The reference signal recording was conducted using a BIOPAC MP36 device (BIOPAC Systems Inc., Goleta, CA 93117, USA), which is equipped with one digital and four analog input ports [Sys22a]. The system converts the analog signals into a digital format with a sampling frequency of 2 kHz. For ECG measurements, the SS2LB module was utilized, capturing a single-channel ECG following Lead II according to Einthoven [Sys13; Bra19]. Three electrodes were placed on the skin below the right clavicle and at the right and left lower thorax. The electrodes

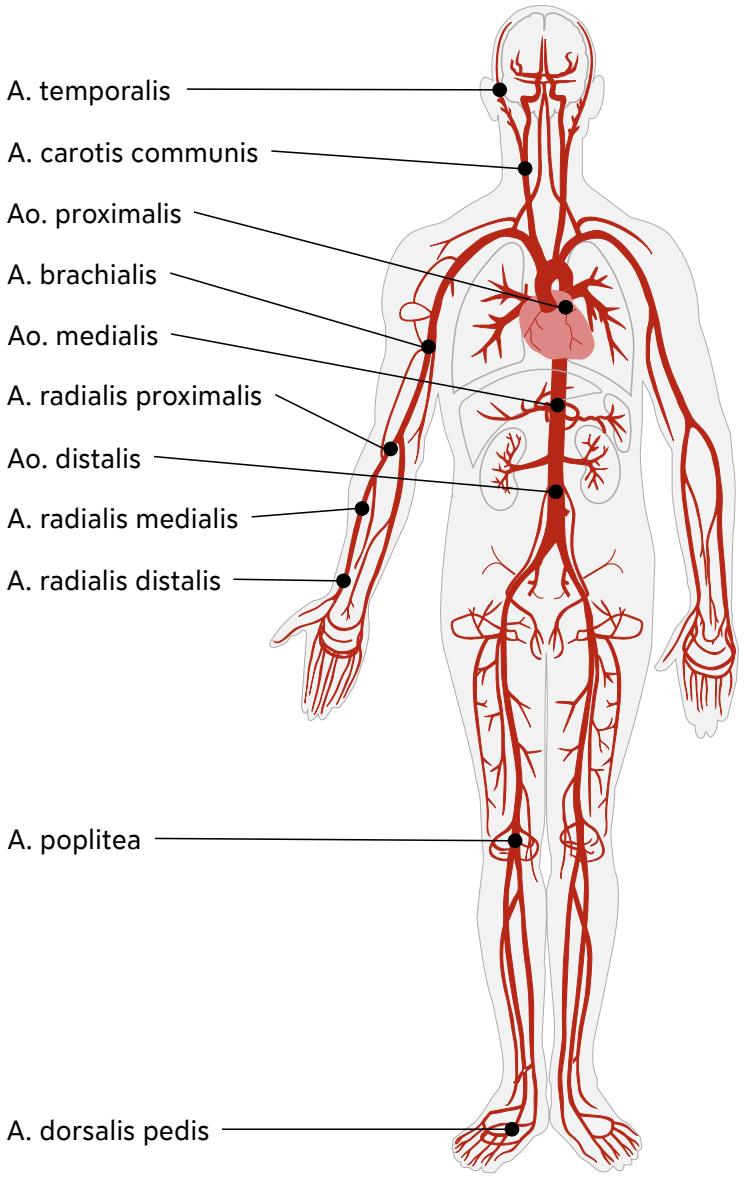

Figure 4.1: Schematic representation of the 11 selected measurement locations within the arterial tree (modified from [Rui09])

were connected to the measurement device via cables. The ICG acquisition used the SS31LA module, equipped with two output channels for impedance (Z) and the derivative of impedance (dZ) [Sys21]. Due to the limited number of analog input channels on the BIOPAC MP36 device, only the derivative dZ was captured. The signal was recorded using an eight-spot electrode lead configuration, arranged in pairs along the right and left mid-axillary lines [Deh19]. Two electrodes each were positioned on the right and left sides of the neck, as well as on the right and left lower thorax. The ECG and ICG electrode placement can be found in Figure 4.2.

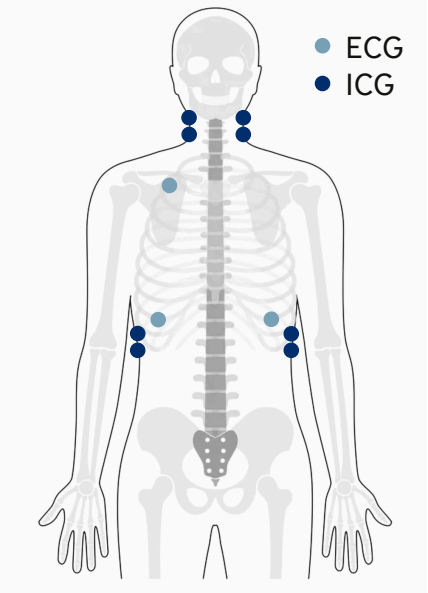

Figure 4.2: Electrode placement for ECG (light blue) and ICG (dark blue) recordings

For PPG measurements, the SS4LA module was employed, a reflective-mode PPG that can be placed on any body part [Sys18]. The system includes a matched infrared emitter and a photodiode detector with a wavelength of 860 ± 60 nm. The PCG signal was acquired utilizing the SS17LA contact acoustical transducer [Sys22b]. This module is based on a piezoelectric ceramic disk bonded to the interior of a plastic circular housing, with the measurement bandwidth ranging from 1 to 1250 Hz. All reference data acquisitions were managed through the Acqknowledge® software (BIOPAC Systems Inc., Goleta, CA 93117, USA), with signals recorded in raw format and no additional filters applied [Sys23]. From there, the data were exported and stored as an ACQ file, which is a specialized BIOPAC Acqknowledge® file format.

Radar Measurement Setup

A specialized measurement setup was developed for the radar data acquisition within the A04 EmpkinS subproject [Emp23]. The constructed frame, composed of aluminum profiles and tripods, was placed over a mattress. It was equipped with two motors that enable precise movement of the radar antenna along the x and y axes above the participant. Navigation of the antenna was achieved through an external controller. The radar antenna utilized a CW Doppler architecture with a carrier frequency of 61 GHz, resulting in a wavelength of $\approx$5 mm. To achieve a precise physiological waveform reconstruction, the emitted electromagnetic waves were focused using a lens, which concentrated the energy on a relatively small spot. The minimal spot size was achieved

within a measurement distance of approximately 10 to 15 cm. The resulting I and Q components were sampled at a frequency of 1953.125 Hz and transmitted to the synchronization node. The synchronization node was configured to collect and synchronize data from up to four radar nodes, although, for the purposes of this thesis, only one radar node was utilized. Additionally, the synchronization node was equipped with an output port capable of distributing the synchronization signal to other external systems. The collected data were transmitted to a computer via Ethernet and stored in a database. Using a Python application, data recordings were managed and extracted from the database, resulting in a file with HDF5 format.

Integrated Measurement Setup

The complete measurement setup, as illustrated in Figure 4.3 a, included the radar measurement setup, the BIOPAC system, a study laptop for recording management, and a smartphone with an application to log the start and end times of the measurements. Each measurement involved the recording of five signals, which can be categorized into global and local recordings. ECG and ICG were considered global recordings as they were continuously measured without changes in their configuration. Radar, PPG, and PCG were classified as local recordings, as they were applied to each measurement location individually. The x-marker in Figure 4.3 corresponds to the radar antenna position. An exemplary data recording at A. carotis communis is presented in Figure 4.3 b.

Throughout the entire data acquisition process, three files were generated. The radar and BIOPAC files, each containing the complete time series signals of the respective modality, and a CSV file containing the start and end times of each individual measurement.

4.1.4 Study Procedure

The study procedure was structured into three phases. In the initial pre-test phase, organizational and preparatory tasks were performed. The second phase focused on identifying measurement locations, while the final part encompassed radar and reference measurements. Participants were instructed to refrain from consuming caffeinated drinks or having large meals between the second and third phases. The first and second phases were conducted in the *Department of Palliative Medicine* at the *University Hospital Erlangen*, situated at the *Klinikum am Europakanal* site, while the concluding part was carried out at the *Machine Learning and Data Analytics Lab* of *Friedrich-Alexander University Erlangen-Nürnberg*.

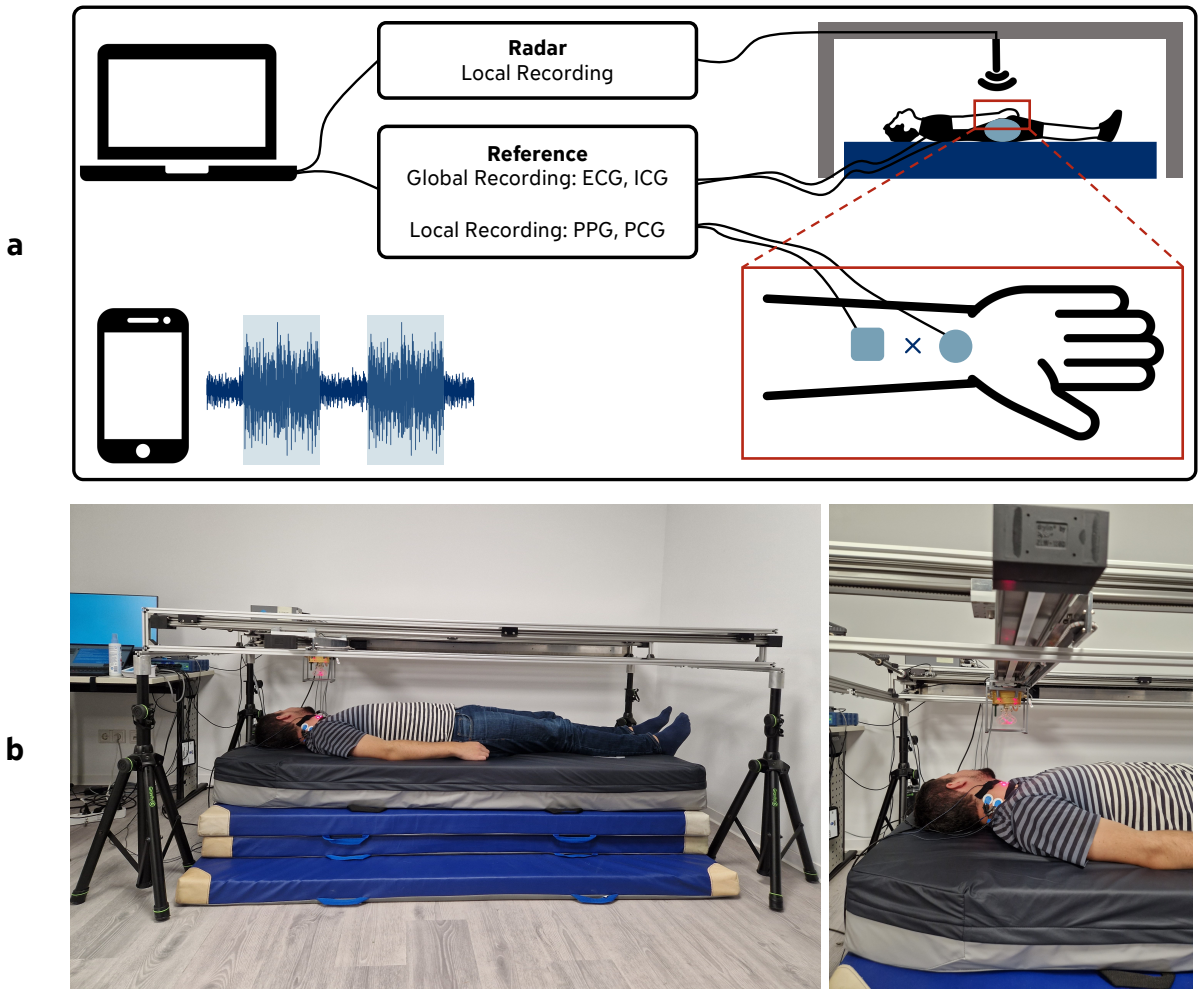

Figure 4.3: Integrated measurement setup for radar and reference signal recording; a: schematic representation; b: exemplary data recording at A. carotis communis

Pre-Test Phase

Upon arriving at the *Department of Palliative Medicine* the study leader explained the study's timeline. Afterward, the participants were asked to sign the declaration of consent. Subsequently, a physician conducted an auscultation to ensure the proper functioning of the heart. Upon clearance, several body measurements were performed, including determining the body weight and body fat percentage using a body scale, along with measurements of waist and hip circumference using a measuring tape. Following this, the participants were questioned about pre-existing conditions, regular and irregular medications, physical activity, and consumption in the last 18 hours. Additionally, female participants were asked for the first day of their last menstruation cycle. The questionnaire is depicted in Figure A.1.

Identification of Measurement Locations

To ensure accurate placement of the radar antenna above the designated measurement locations, all sites were identified either through ultrasonography or based on anatomical landmarks prior to the signal recording. The examination was conducted using a TOSHIBA Xario 200 ultrasonography device (TOSHIBA Medical Systems GmbH Deutschland, Neuss, Germany) by professionals with medical training. Each identified location was marked using a skin marker. Comprehensive details regarding participants' positions, body part placements, and additional instructions for precise identification can be found in Table 4.3.

Table 4.3: Identification of Measurement Locations; column **I** indicates whether the identification was performed based on ultrasonography (U) or landmarks (L); column **P** indicates whether the participant was in a supine (S) or prone (P) position.

Measurement Location	**I**	**P**	**Position Body Part**	**Identification**
A. temporalis	U	S	Head 90° rotated left	Distal of the ear
A. carotis communis	U	S	Head 90° rotated left	Proximal of the glomus caroticum
A. brachialis	U	S	Arm abducted and externally rotated	Distal of the pectoralis muscle
A. radialis proximalis	U	S	Palm facing upwards	Distal of the bifurcation of A. brachialis
A. radialis medialis	U	S	Palm facing upwards	Middle between A. radialis proximalis and A. radialis distalis
A. radialis distalis	U	S	Palm facing upwards	Proximal of the wrist
Ao. proximalis	L	S	-	Erb's point
Ao. medialis	L	S	-	2 cm distal of the xiphoid
Ao. distalis	L	S	-	2 cm proximal of the umbilicus
A. dorsalis pedis	U	S	Knee bent and foot laid flat	Lateral to the extensor tendon of the extensor hallucis longus muscle
A. poplitea	U	P	-	Within the fossa poplitea

For locations identified using ultrasonography, both the flow profile (Figure 4.4 a) and the B-Mode ultrasound image (Figure 4.4 b) were captured and stored in the Digital Imaging and Communications in Medicine (DICOM) format. Additionally, the measured flow rate f, vessel diameter $\varnothing$, and distance d between the artery and the body surface were documented, as depicted in Figure 4.4.

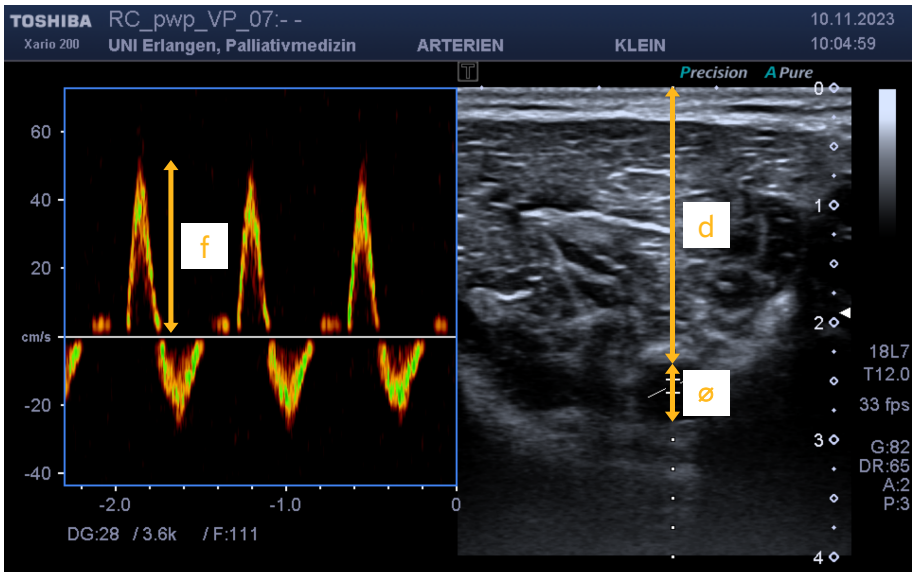

Figure 4.4: Exemplary ultrasonography examination at A. poplitea; a: flow profile measured in $\mathrm{cm\,s^{-1}}$; b: B-Mode ultrasound image

To enable PWV calcuation, distance measurements between the A. brachialis and A. radialis proximalis, A. radialis proximalis and A. radialis medialis, A. radialis medialis and A. radialis distalis, Ao. medialis and Ao. distalis, as well as A. poplitea and A. dorsalis pedis were conducted using a measuring tape. However, the PWV evaluation is not part of this thesis.

Signal Recording

After arriving at the *Machine Learning and Data Analytics Lab*, electrodes were attached to the participants' skin according to Figure 4.2, and an initial BP measurement was conducted. Subsequently, the participants were instructed to lay down in a supine position on the mattress within the radar measurement setup. Afterward, the cables for ECG and ICG recordings were connected to the electrodes. For an initial comparison of the system times of the laptop and the smartphone, a so-called event marker was set on the laptop in the Acqknowledge® software using a key combination. Simultaneously, the smartphone's system time was recorded by creating a measurement in the time logger application.

During the subsequent data acquisition, the participants were instructed to remain as calm as possible and to breathe at leisure. The purpose of this instruction was to ensure that no significant changes in the physiological state of the participants occurred and thus the BR, HR, and TPR remained constant throughout the data recording.

Table 4.4: Procedure for signal recording

Measurement Location	Position Participant	Position PPG	Position PCG	Breathing Normal	Breathing Hold
Baseline	Supine	-	-	✓	
A. temporalis	Supine	-	-	✓	
A. carotis communis	Supine	Proximal	Distal	✓	
A. brachialis	Supine	Proximal	Distal	✓	
A. radialis proximalis	Supine	Proximal	Distal	✓	
A. radialis medialis	Supine	Proximal	Distal	✓	
A. radialis distalis	Supine	Proximal	Distal	✓	
Ao. proximalis	Supine	Proximal	Distal	✓	✓
Ao. medialis	Supine	Proximal	Distal	✓	✓
Ao. distalis	Supine	Proximal	Distal	✓	✓
A. dorsalis pedis	Supine	Proximal	Distal	✓	
A. poplitea	Prone	Proximal	Distal	✓	

A total of 15 measurements, each lasting 2 min, were conducted in the sequence outlined in Table 4.4. For the first 14 measurements, participants were in a supine position, while for the last measurement at the A. poplitea, they had to turn into a prone position. The initial baseline served as a measurement for participants to adjust to the general setup, with no local recordings performed. For all other measurements, the radar antenna was focused on the skin marking placed in the previous study phase. The PPG sensor was consistently placed proximal and the PCG sensor distal with regard to the radar antenna, with one exception being the A. temporalis. As there is only limited space available, no local reference signals were recorded at this measurement location. As respiration was expected to influence the signal quality at the three locations on the trunk, the recording was conducted twice with different breathing patterns. In the first recording, participants were instructed to maintain normal breathing, while in the second recording, they were asked to hold their breath. Participants were allowed to interrupt breath-holding during the measurement. The sensor setup remained unchanged between the two recordings.

The procedure for data acquisition at each measurement location followed a consistent protocol. Initially, the corresponding body part was positioned according to Table 4.3 and adjusted to ensure the body surface was as horizontal as possible. Pillows were used if necessary to support this process, aiming to counteract the reflection of electromagnetic waves in a direction other than the antenna. Subsequently, the PPG and PCG sensors were attached to the skin using elastic adhesive tape, and the radar antenna was placed in the correct position. Following a check of the signal quality and potential repositioning of the body part or radar antenna, the measurement was

initiated, and the start and end times were documented using the smartphone. After completing all measurements, the subject was disconnected from the BIOPAC device, and a second BP assessment was conducted.

4.2 Data Processing

In the following sections, the different data processing steps are explained. From the recorded dataset, one measurement at A. temporalis had to be excluded from further processing, as the ECG recording failed due to inexplicable issues.

4.2.1 Data Synchronization and Alignment

Data synchronization and alignment is a crucial step to ensure temporal alignment of data recorded through separate data acquisition systems.

One synchronization issue arose from the potential deviation between the system times of the study laptop and smartphone. When segmenting the signal into individual measurements, this constant time offset could lead to segments that do not accurately correspond to the actual measurements. This issue was resolved through the synchronization procedure conducted during the signal recording phase of the study. By comparing the timing of the placed BIOPAC event marker with the start time of the logged synchronization measurement on the smartphone, the shift between both systems was determined. Subsequently, the logged start and end times of the individual measurements were corrected by adding the shift value.

Due to the total duration of the data recording, additional data synchronization issues could arise from clock inaccuracies in the radar or BIOPAC system. To counteract this potential problem, the data from both systems were synchronized using the following procedure. The synchronization node, integrated into the radar measurement setup as described in Chapter 4.1.3, generated an m-sequence synchronization signal which was transmitted to the digital input port of the BIOPAC system. As a result, both datasets incorporated the same synchronization sequence. By transforming both synchronization signals into the frequency domain, the actual sampling frequency was determined. Using this measured sampling frequency, radar and reference signals were resampled to the same frequency of 1 kHz. The offset between both signal types was determined through the calculation of cross-correlation between the resampled synchronization signals. Subsequently, the alignment was achieved by segmenting the time series data into individual measurements based on the corrected start and end times and shifting them according to the calculated offset.

4.2.2 Data Preprocessing

As the data were segmented into individual measurements in the data synchronization and alignment step, all subsequent processing steps were applied on a single measurement level.

Radar Preprocessing

By utilizing the measured phase changes $\Delta\psi$, the relative distance changes ΔR of the target were calculated following a similar procedure as outlined in [Wil18]. ΔR was determined by incorporating $\Delta\psi$ into

$$\Delta R = \frac{\Delta\psi}{2\pi} \cdot \frac{\lambda}{2}, \tag{4.1}$$

where $\lambda = c/f_0$ denotes the wavelength of the carrier frequency f_0, with c representing the speed of light. The ideal unit circle representation of a moving target in the complex plane is distorted to an offset ellipse due to nonidealities in the radio frequency front end. To obtain an undistorted distance signal, the first step involved determining the ellipse barycenter and subtracting it from the I and Q components, as depicted in Figure 4.5 a. A subsequent arctangent demodulation yielded in phase values within the range $[-\pi, +\pi)$, illustrated in Figure 4.5 b, representing a target movement range equivalent to $\lambda/2$. Since a phase value of $+\pi$ is equivalent to $-\pi$, phase jumps occurred for movements beyond the initial unambiguous range. Therefore, phase jumps larger than $+\pi$ or $-\pi$ were corrected by adding or subtracting 2π. By converting the resultant signal from radiant to meter, the final displacement vector was obtained, presented in Figure 4.5 c.

Following the reconstruction process, the displacement vector was filtered to extract PW and HS waveforms. As highlighted by Will et al., conventional narrow bandpass filter characteristics may distort local PW shapes into simpler waveforms [Wil17a]. To address this, they proposed a fourth-order Butterworth bandpass filter with a passband ranging from 0.75 to 20 Hz for local PW extraction. This filter was applied to the displacement vector with a slight modification of reducing the lower cutoff to 0.5 Hz to support lower HRs. According to [Wil18; Mic19], the HS signal was obtained through filtering using a fourth-order Butterworth bandpass with a passband ranging from 16 to 80 Hz. In the following, the obtained radar PW signal is denoted as PW_{RAD} and the radar HS signal as HS_{RAD}, respectively.

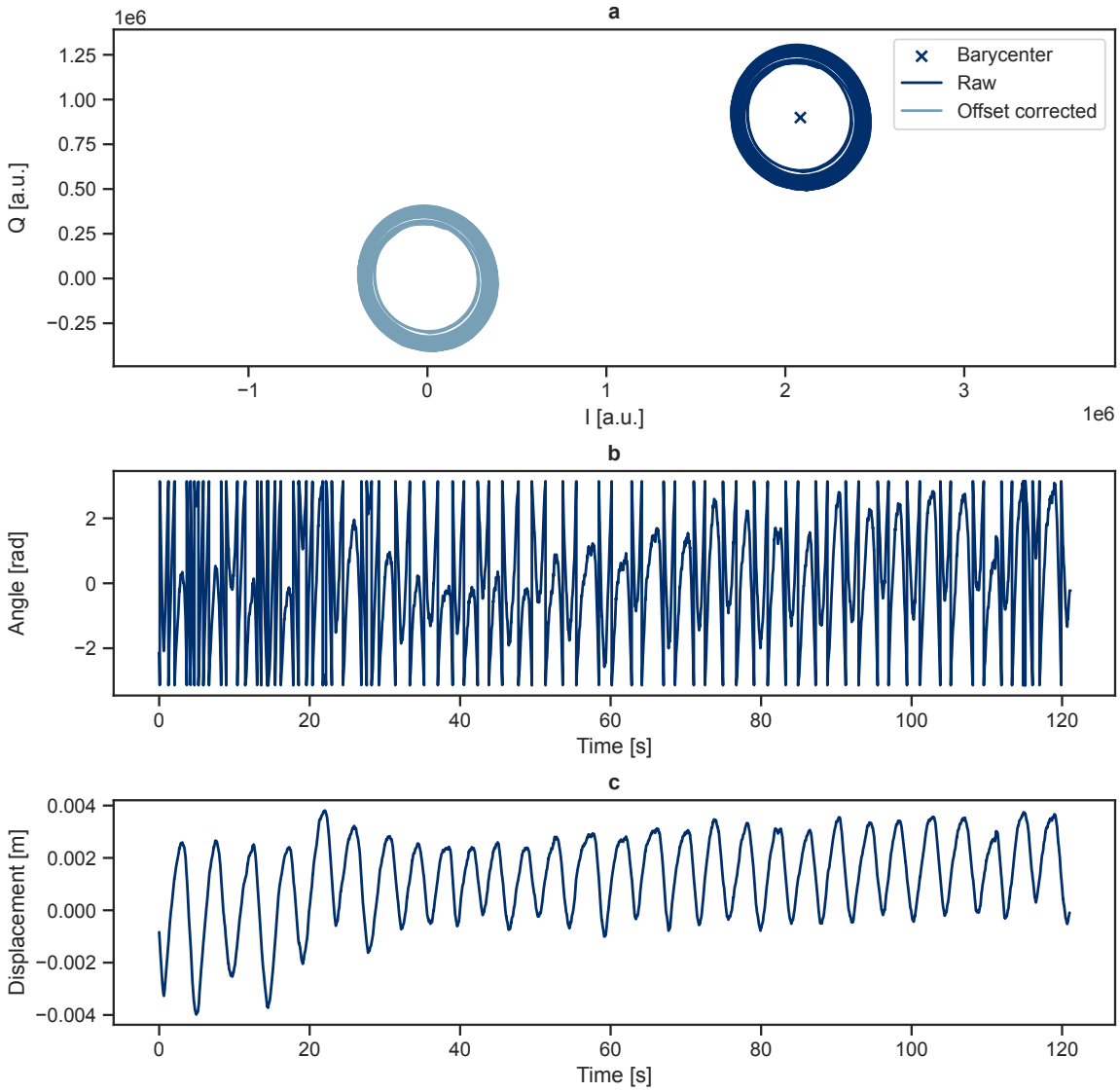

Figure 4.5: Exemplary reconstruction process of the relative distance changes at Ao. proximalis; a: complex representation of the raw and offset corrected I and Q values; b: phase values obtained by arctangent demodulation; c: displacement after phase jump correction and conversion to meters

Reference Signal Preprocessing

The ECG preprocessing was conducted using the *neurokit* library [Mak21]. A fifth-order Butterworth highpass filter with a cutoff frequency of 0.5 Hz was applied to reduce baseline artifacts, followed by a moving average filter with the width of one period of 50 Hz to diminish powerline artifacts. Subsequently, R-peaks were extracted based on the cleaned signal.

As the PPG measures light intensity values and not the absorption, the recorded PPG signal was inverted as a first step [Par22]. Following the inversion, the same filter, a fourth-order Butterworth bandpass filter with a passband ranging from 0.5 to 20 Hz, as used for radar PW extraction, was applied. Similarly, the PCG underwent filtering using a fourth-order Butterworth bandpass filter with a passband ranging from 16 to 80 Hz. Additionally, the *neurokit* 50 Hz powerline filter was applied, considering the microphone's susceptibility to powerline interference [Mak21; Sys22b]. In the following, the obtained reference PW signal (PPG) is denoted as PW_{REF} and the reference HS signal (PCG) as HS_{REF}, respectively.

As only the dZ component was recorded, the ICG needed to be integrated to extract the respiration pattern. Before integration, the signal was filtered using a fourth-order Butterworth lowpass filter with a cutoff frequency of 25 Hz. This method was recommended by Forouzanfar et al. because it preserves the dZ signal shape while effectively eliminating influences from higher frequencies and powerline interference [For19]. Originally, the authors proposed a bandpass filter with a passband ranging from 0.5 to 25 Hz. However, since in this use case the focus was on the respiration component of the ICG, a lowpass filter was applied in place of the initially suggested bandpass filter. Following the filtering step, the mean was subtracted and the resultant signal was integrated over time. In the final step, the reconstructed Z signal was filtered for respiration extraction. In measurements involving a regular breathing pattern, a fourth-order Butterworth bandpass filter with a passband spanning from 0.05 to 0.5 Hz was applied [Mic19]. This choice facilitates a BR range of 3 to 30 breaths per minute. Conversely, for measurements where participants held their breath, a fourth-order Butterworth lowpass filter with a 0.5 Hz cutoff frequency was applied for signal cleaning [Mic19]. For regular breathing measurements, the respiration was segmented into inspiration and expiration phases utilizing the *neurokit* library [Mak21].

Figure 4.6 illustrates the preprocessed ECG, PPG, PCG, and respiration signals, along with the respective segmentations, for a 10 s segment measured at the A. carotis communis. As in the cases of the breath-holding measurements no consistent pattern could be observed, an automatic segmentation was not feasible. Consequently, a manual segmentation process was employed to identify the phases of breath-holding, as depicted in Figure 4.7. All filters employed in the radar and reference data preprocessing were applied in forward and backward directions to avoid the induction of any phase shift.

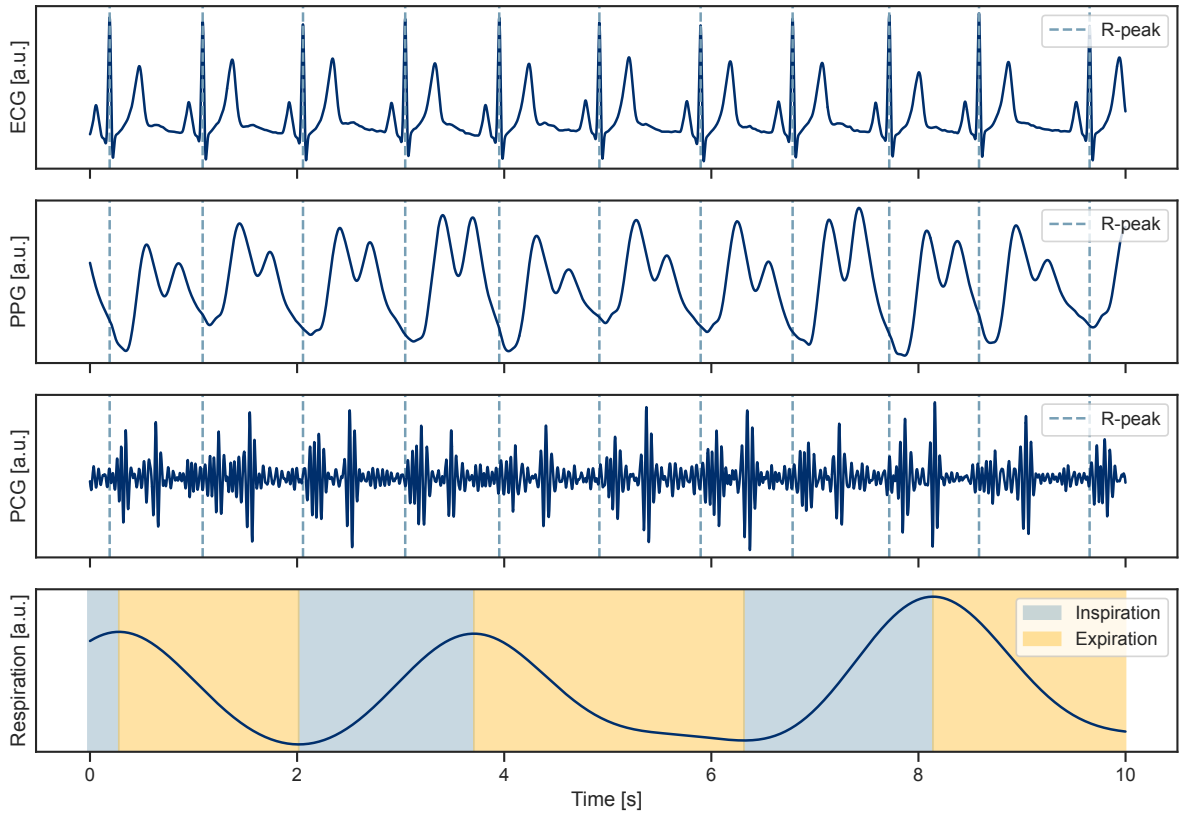

Figure 4.6: Exemplary preprocessed ECG, PPG, PCG, and respiration reference signals including respective segmentations at A. carotis communis

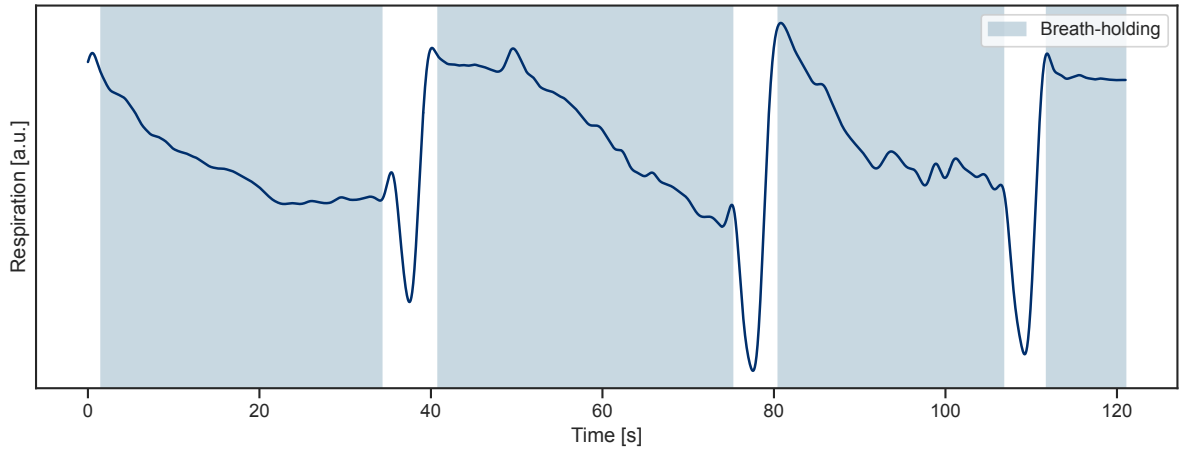

Figure 4.7: Exemplary manual segmentation of the breath-holding respiration signal measured at the Ao. proximalis

4.2.3 Ensemble Averaging

To further enhance the underlying signal and reduce random noise, ensemble averaging (EA) was applied to PW_{RAD} and HS_{RAD}, as well as PW_{REF} and HS_{REF}. In general, the data for each measurement, i. e. the signal recorded at an individual measurement location, was segmented into interbeat intervals (IBIs) based on the R-peaks detected in the ECG signal. For normal-breathing measurements, all IBIs were utilized, while for breath-holding measurements, only IBIs completely within a segment without respiration were considered. After resizing the IBIs to the same length, outliers were detected, and the average was computed. To explore variations in the shapes of the respective signals over time, the EA procedure was repeated for windows of $N = 30$ IBIs, shifted by one IBI. Based on the signal properties and the specific requirements of subsequent processing steps, the EA procedures differ for PWs and HSs. These variations include differences in the type of input signal, IBI extraction method, and the resizing approach, as explained below.

For EA of PW_{RAD} and PW_{REF}, the respective preprocessed signals served as the base signals. The signals were segmented into IBIs using the procedure visualized in Figure 4.8 a. Each segment was defined as the current IBI and 70 % of the subsequent IBI to account for PW runtimes. All segments determined for PW_{REF} measured at the A. carotis communis can be found in Figure 4.9 a. As evident from this visualization, the physiological heart rate variability (HRV) results in segments of varying lengths, leading to a blurring of the original morphology when applying EA. To address HRV, the segments were resampled to a common length of twice the sampling frequency

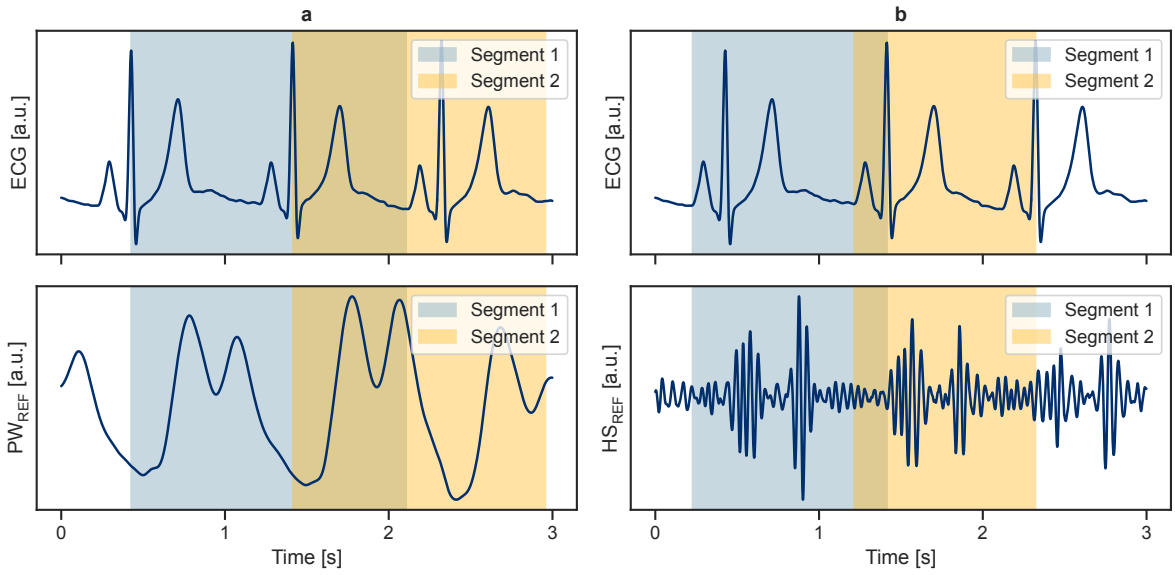

Figure 4.8: IBI segmentation methods for EA; a: PW IBI segmentation; b: HS IBI segmentation

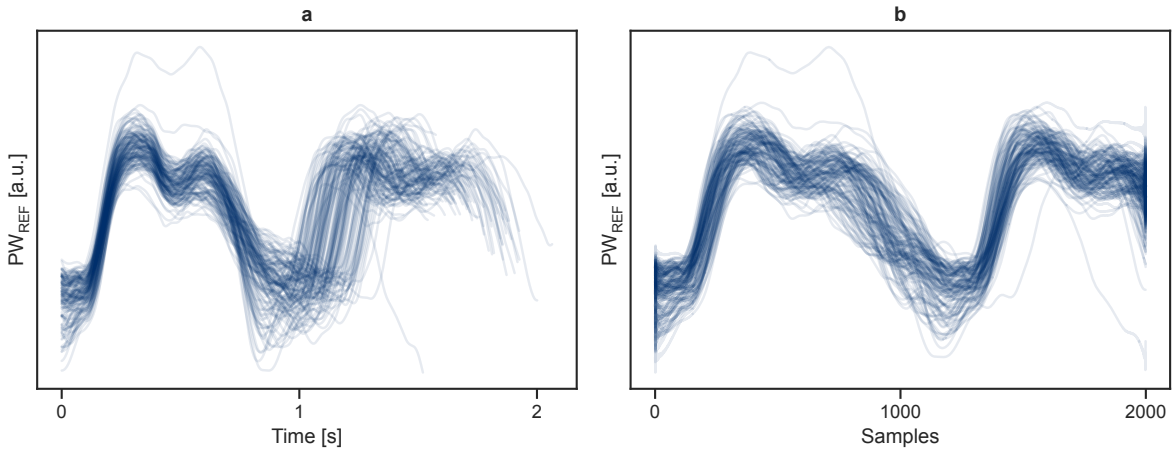

Figure 4.9: Exemplary EA intermediate steps at A. carotis communis; a: all segments for PW_{REF}; b: all resampled segments for PW_{REF}

($f_s = 1\,\text{kHz}$) to obtain an accurate signal morphology, as illustrated in Figure 4.9 b. As due to this procedure the time information was lost, a second version of EA was conducted, where the segments were simply resized to the same length. The resizing was performed as follows: The median signal length of all considered segments was determined. If the individual segment was shorter, it was padded at the end with its edge value; if the individual segment was longer, the segment was cut to the median length. For outlier correction, the RMSE between each individual segment and the average over all considered segments was computed. Segments with an error larger than two standard deviations (SDs) from the average error were excluded. Finally, the average over all considered segments was computed. In the following, resampled PW ensemble averages are referred to as PW_{RAD_MORPH} and PW_{REF_MORPH}, while the resized ensemble averages are denoted as PW_{RAD_TEMP} and PW_{REF_TEMP}.

The EA procedure for HS_{RAD} and HS_{REF} follows a similar approach. As averaging the preprocessed HS signal over multiple segments could lead to signal cancellation due to phase shifts and imperfect alignment, two types of envelopes were used in addition to the preprocessed signal as input signals.

The first envelope employed as input signal for EA was the Hilbert envelope (HE), calculated as the absolute value of the Hilbert transform [Niz22]. The HE is frequently used in the context of HS analysis and employed in this context due to its amplitude-preserving characteristic. As second envelope, the second order Shannon energy (SE) was computed according to Giordano et al. [Gio19] following Equation 4.2.

$$E_S = -\frac{1}{N}\sum_{i=1}^{N} x^2(i) \cdot \log x^2(i) \tag{4.2}$$

In this context, x denotes the normalized and filtered HS signal and N corresponds to the length in samples of the moving integration window [Gio19]. The window size is set to 20 ms, corresponding to 20 samples at a sampling frequency of 1 kHz, with an overlap of 1 ms. Contrary to Giordano et al., the HS signal was padded with its edge value and half the window size at both ends and averaged over a window of 21 samples to obtain an envelope signal with the same length as the original signal. As the normalization procedure was not further specified in [Gio19], the HS signal was normalized according to Equation 4.3 [Sai16].

$$x(i) = \frac{x(i)}{\max(|x|)} \tag{4.3}$$

For all three signals, the segments were extracted from the respective input signal based on a fixed time interval. One segment consists of the current IBI and 200 ms of the preceding IBI, as visualized in Figure 4.8 b. Subsequently, the segments were resized without resampling, outlier corrected, and averaged, as described before. In the following, the ensemble averages computed from the preprocessed HS signals are denoted as HS_{RAD_SIG} and HS_{REF_SIG}, while the SE ensemble averages are referred to as HS_{RAD_SE} and HS_{REF_SE} and the HE ensemble averages as HS_{RAD_HE} and HS_{REF_HE}.

Exemplary results obtained for the reference signals of one participant at A. carotis communis are presented in Figure 4.10.

4.3 Visual Data Inspection

In order to better understand at which measurement locations it is feasible to detect PWs and HSs, the signals generated through EA were visually inspected. Timing and morphology were compared within and between radar and reference signals on a location as well as participant level. For PWs, several inconsistencies were identified during the visual inspection. Therefore, their propagation was not further analyzed in the scope of this work. HS signals did not seem to be affected by these issues and were therefore further investigated.

To gain insights into the feasibility of detecting HSs at peripheral locations, the first two HSs (S1 and S2) were manually labeled in the HS_{RAD_SIG}, HS_{REF_SIG} and HS_{RAD_SE}, HS_{REF_SE} signals, as depicted in Figure 4.11.

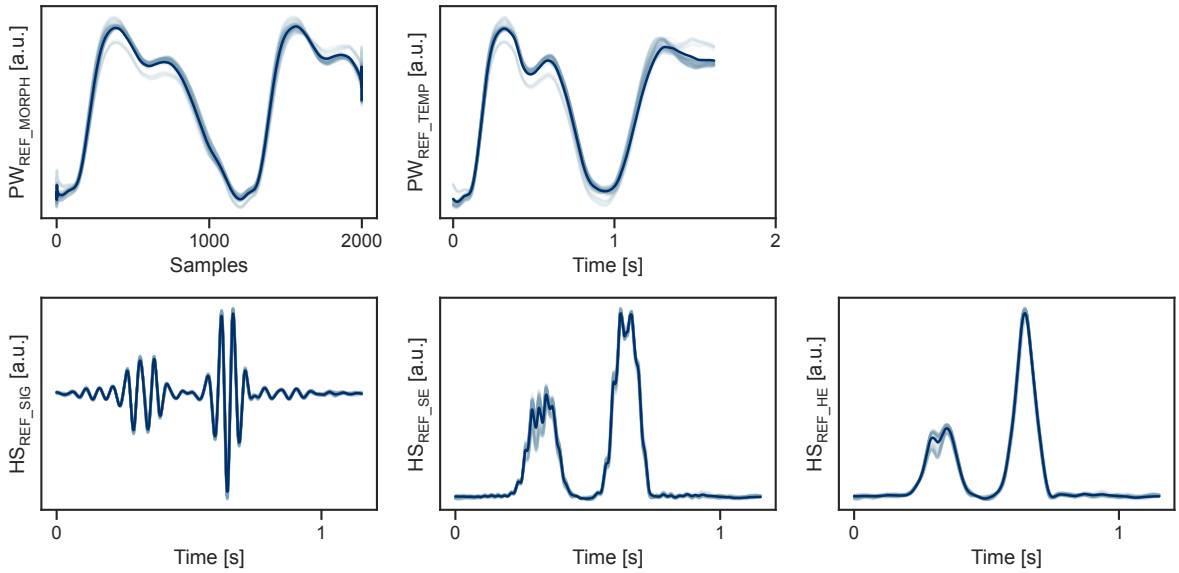

Figure 4.10: Exemplary EA results at A. carotis communis; EA windowed over time are presented in the background of each subfigure.

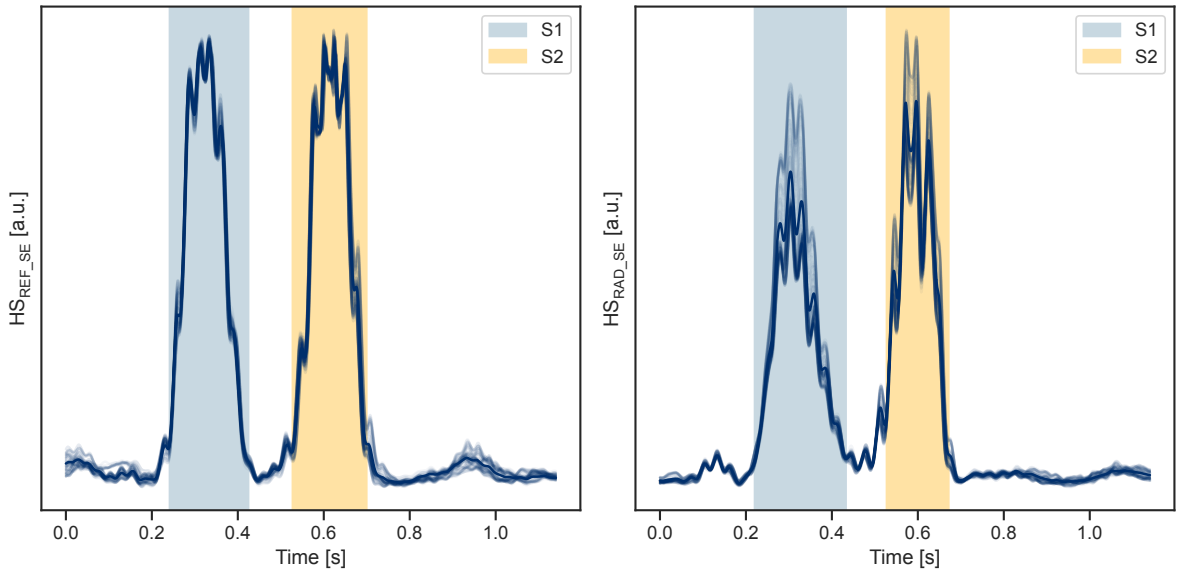

Figure 4.11: Exemplary manual HS detection in HS_{REF_SE} and HS_{RAD_SE} at A. carotis communis; The ensemble averages over time of the respective signal are visualized in the background.

4.4 Feature Engineering

This section describes the processing steps conducted to derive a set of meaningful features from the radar-recorded HSs. As robust segmentation into individual HSs is a crucial step for feature extraction [Dis20], a HS segmentation algorithm was applied in advance.

4.4.1 Heart Sound Segmentation

Will et al. and Schellenberger et al. utilized a logistic regression HSMM approach based on the work by Springer et al. [Spr15] to segment their radar-recorded HS signal into the phases of the cardiac cycle (S1, systole, S2, diastole) [Wil18; Sch20b]. However, this method relies on the R-peak and end of the T-wave as reference points for S1 and S2 [Spr15], making it unsuitable in this context, where different runtimes between measurement locations need to be considered.

HS segmentation algorithms based on PCG envelopes are widely employed in the literature, with the second-order SE providing the highest accuracy [Mil22]. The algorithm proposed by Giordano et al. relies on a moving window integration of the second-order SE [Gio19]. With a 1 ms overlap, equivalent to one sample at a sampling frequency of 1 kHz, it preserves the original time resolution, allowing for accurate HS detection. The envelogram computation was already performed in the EA step in Chapter 4.2.3. Therefore, only the remaining steps of the algorithms are described here.

Originally, Giordano et al. employed a moving window normalization, as expressed in Equation 4.4,

$$E_S(t) = \frac{E_S(t) - \overline{E_S(t)}}{\sigma_{E_S(t)}} \tag{4.4}$$

to normalize the obtained SE E_S, where $\overline{E_S(t)}$ denotes the mean and $\sigma_{E_S(t)}$ represents the SD calculated within a sliding 1 s window [Gio19]. In the computation of $\text{HS}_{\text{RAD\_SE}}$, the input signal was already divided into individual IBIs. Therefore, the normalization was applied on the whole $\text{HS}_{\text{RAD\_SE}}$ signal instead. Subsequently, negative values were set to zero. The initial HS segmentation was then obtained by thresholding with a threshold set to 5 % of the maximum SE.

Since the initial segmentation of one HS could be divided into multiple segments (Figure 4.12 a) or the segmentation could include false positives, Giordano et al. use known temporal relationships between HSs and with regard to the ECG to clean the segmentation [Gio19]. Due to known reasons, this is not feasible in this context. Therefore, the knowledge about the HS locations obtained during visual inspection was incorporated into the cleaning process. All segments that lie within, start, or end within the segmentation identified by visual inspection were associated with the respective HS.

All other segments were excluded. In cases where no HS was detected during visual inspection, all segments were discarded. This results in a segmentation visualized in Figure 4.12 b. In the following, the HS segmentation is denoted as HS_{RAD_SEG}.

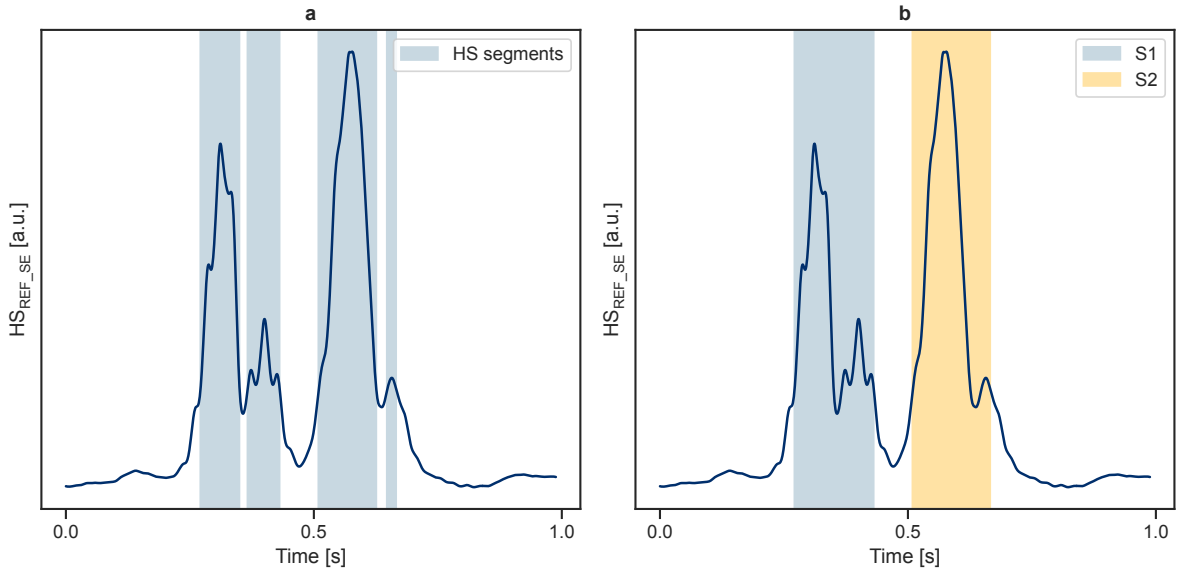

Figure 4.12: Exemplary HS segmentation at A. carotis communis; a: HS segments obtained from algorithm by Giordano et al. [Gio19]; b: cleaned HS segmentation

4.4.2 Feature Extraction

The feature computation was conducted to investigate differences in temporal and morphological properties of HSs across the measurement locations. Features can be divided into two distinct categories. While generic features do not demand prior knowledge and encompass basic signal characteristics like mean and variance, expert features are designed based on domain expertise to describe HS propagation.

Generic Features

The generic features computed are partially included in the feature set utilized by Shi et al. for the automated assessment of HS quality [Shi20a]. The features were derived from HS_{RAD_SIG}, regardless of whether a HS was detected. Since the amplitude is evaluated in the expert feature set, the signals were normalized before computation following Equation 4.5. A summary of the generic feature set is provided in Table 4.5.

$$x(i) = \frac{x(i) - \min(x)}{\max(x) - \min(x)} \tag{4.5}$$

Table 4.5: Overview of generic features

Feature Name	Explanation	Unit
Mean	Mean of the signal	m
Variance	Variance of the signal	m^2
Kurtosis	Measure for the tailedness of the probability distribution	a.u.
Skewness	Measure for the asymmetry of the probability distribution	a.u.
Entropy	Measure for the uncertainty in the signal	bit
Spectral Entropy	Measure for the spectral power distribution	a.u.

Expert Features

Expert features were derived based on HS_{RAD_SEG}, HS_{RAD_HE}, HS_{RAD_SIG}, and the R-peak location to describe the morphological and temporal properties of HSs.

Within the group of temporal features, the durations of S1 and S2 were computed in seconds, as depicted in Figure 4.13 a. Furthermore, the HS duration normalized with respect to the HS_{RAD_SIG} signal length was calculated to account for possible differences in HRs among participants. Additionally, the ratio between the durations of S1 and S2 was determined. To assess the propagation of HSs, intervals between the R-peak and the onset, maximum, center, and offset were calculated for both HSs (Figure 4.13 b). Normalized values were also obtained, following the same procedure as described for the duration features. The relation between both HSs was evaluated within the inter-HS feature group. Intervals between S1 and S2 landmarks (Figure 4.13 c), were calculated as time intervals and in the normalized manner. An overview of the temporal features can be found in Table 4.6. In this context *HS* serves as a placeholder for S1 and S2, respectively.

The morphological group includes features related to the signal amplitude (Figure 4.13 d). Amplitudes of S1 and S2 were calculated between the signal's baseline and the maximum positive value, as well as the peak-to-peak (P2P) amplitude. Additionally, the ratios between S1 and S2 amplitudes were derived. Furthermore, the envelope amplitude between the segmentation threshold and the maximum value (Figure 4.13 e), the area under the curve (AUC) (Figure 4.13 f), and the zero crossing rate (ZCR) (Figure 4.13 g), were computed for S1 and S2, as well as their ratio. Lastly, the HS symmetry was evaluated by computing the ratio between onset-maximum and maximum-offset intervals (Figure 4.13 h). An overview of the morphological features can be found in Table 4.7, with *HS* serving as a placeholder for S1 and S2.

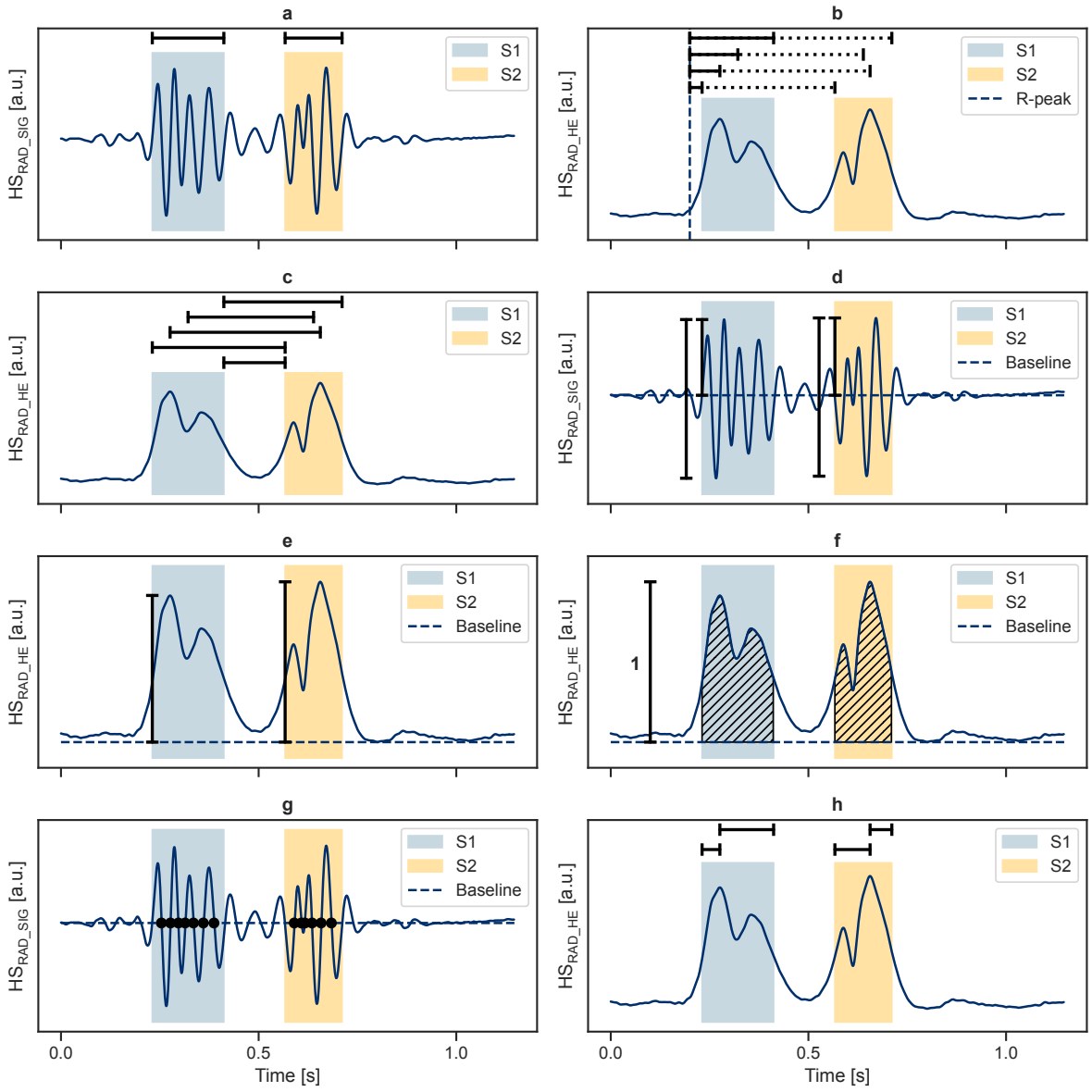

Figure 4.13: Expert feature extraction visualized at A. carotis communis; a: duration features; b: propagation features; c: inter-HS features; d: signal amplitude features; e: envelope amplitude features; f: AUC features; g: zero crossing features; h: symmetry features

Table 4.6: Overview of temporal features

Feature Group	Explanation	Unit
Duration	*HS* duration	s
	HS duration normalized	a.u.
	Duration ratio between S1 and S2	a.u.
Propagation	Interval between R-peak and *HS* onset	s
	Interval between R-peak and *HS* onset normalized	a.u.
	Interval between R-peak and *HS* maximum	s
	Interval between R-peak and *HS* maximum normalized	a.u.
	Interval between R-peak and *HS* center	s
	Interval between R-peak and *HS* center normalized	a.u.
	Interval between R-peak and *HS* offset	s
	Interval between R-peak and *HS* offset normalized	a.u.
Inter-HS	Interval between S1 onset and S2 onset	s
	Interval between S1 onset and S2 onset normalized	a.u.
	Interval between S1 maximum and S2 maximum	s
	Interval between S1 maximum and S2 maximum normalized	a.u.
	Interval between S1 center and S2 center	s
	Interval between S1 center and S2 center normalized	a.u.
	Interval between S1 offset and S2 offset	s
	Interval between S1 offset and S2 offset normalized	a.u.
	Interval between S1 offset and S2 onset	s
	Interval between S1 offset and S2 onset normalized	a.u.

Table 4.7: Overview of morphological features

Feature Group	Explanation	Unit
Signal Amplitude	*HS* amplitude	m
	HS P2P amplitude	m
	Amplitude ratio between S1 and S2	a.u.
	P2P amplitude ratio between S1 and S2	a.u.
Envelope Amplitude	*HS* envelope amplitude	m
	Envelope amplitude ratio between S1 and S2	a.u.
AUC	*HS* AUC	a.u.
	AUC ratio between S1 and S2	a.u.
Zero Crossing	*HS* ZCR	Hz
	ZCR ratio between S1 and S2	a.u.
Symmetry	*HS* ratio between onset-peak and peak-offset	a.u.

Chapter 5

Results and Discussion

This chapter presents and discusses the obtained results. One participant was excluded from the dataset due to failed ECG segmentation. Elevated T-wave amplitudes led to an almost consistently present mismatch of T-waves as R-peaks, corrupting the segmentation into single IBIs and, therefore, the EA procedure. In the following, single participants are denoted as VP_XX, e. g. VP_01. VP stands for the German ”Versuchsperson” (participant).

5.1 Peripheral Pulse Wave Detection

During the visual data inspection, the PW_{REF_MORPH} and PW_{RAD_MORPH} signals were compared extensively within the modality, but also between the measurement locations and participants.

Generally, good signal quality was observed for peripheral PW_{REF_MORPH} measurements, while the signal shapes recorded at the trunk were more distorted, exhibiting greater variation between participants and over time. Consequently, atypical waveforms, diverging from the well-established signal shape described in Chapter 2, were recorded. In addition, it was observed that the orientation changed for some participants within one measurement, visualized in Figure 5.1 a. Upon closer inspection of the underlying PW_{REF} signal in this particular case (Figure B.1), it was determined that the change in orientation occurred after a phase with a corrupted signal shape and reduced amplitude. The different phases of the signal were separated by a signal artifact. Furthermore, changes in orientation occurred within one location and between participants (Figure 5.1 b), within one participant and between locations (Figure 5.1 c), as well as within one location between measurements (Figure 5.1 d). No consistent pattern explaining the occurrence of these flips was found. Additionally, it was noted that for some participants, the signal shapes deviated between measurements at the same location when the breathing pattern was changed (Figure 5.1 e).

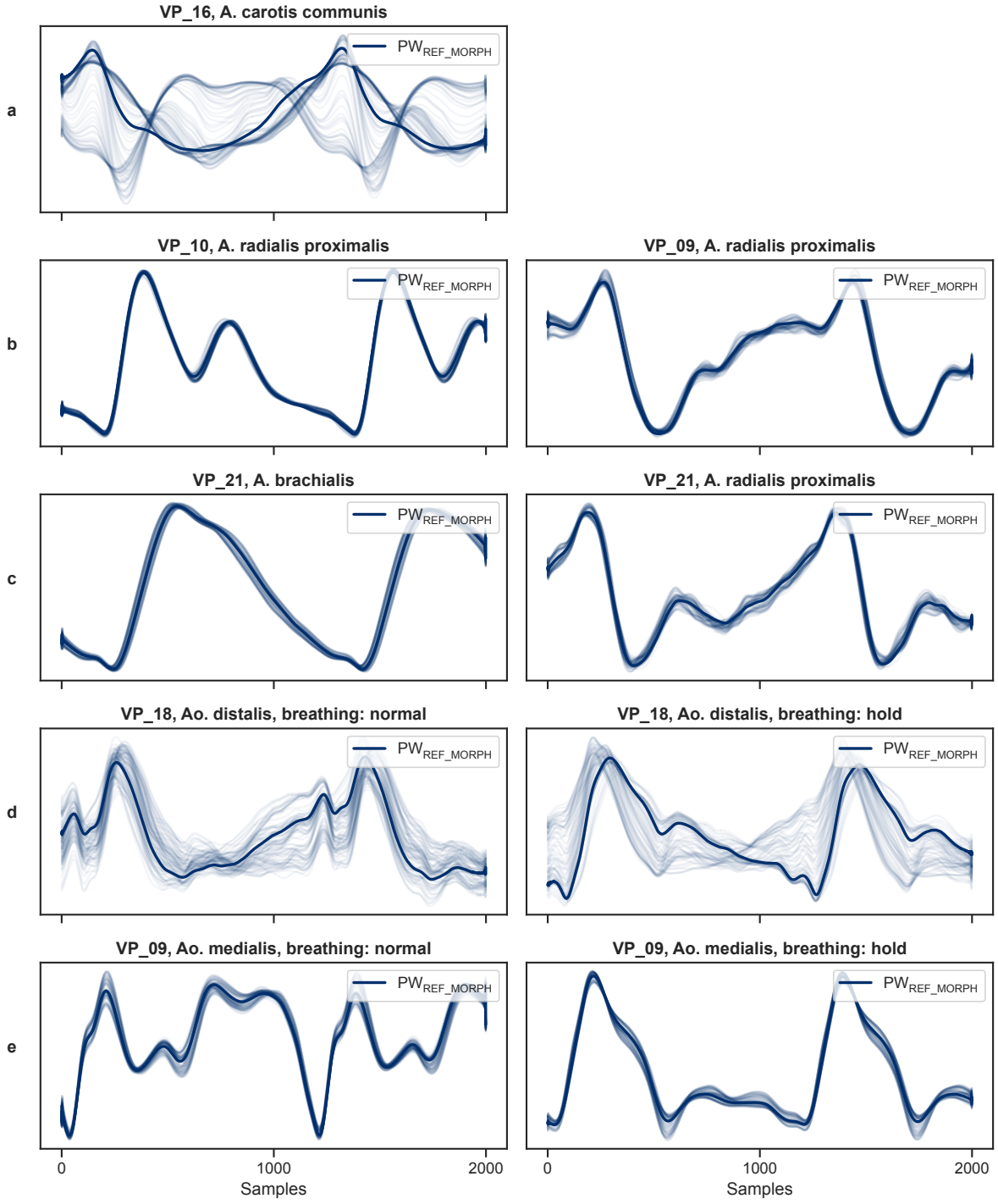

Figure 5.1: Discrepancies in PW_{REF} recordings; change in orientation a: within one measurement, b: within one location, c: within one participant, d: within one location between measurements; e: deviating signal shapes within one location between measurements

By inspecting the PW_{RAD_MORPH} signals, periodic waveforms were observed for all locations, with signal quality varying between participants and locations. A collection of PW_{RAD_MORPH} signals across all locations and most of the participants is depicted in Figure 5.2. Good measurability was perceived for measurements at the trunk, A. carotis communis, A. radialis proximalis, and A. poplitea, while medium or poor signal quality was noted at the remaining locations.

Through the comparison of PW_{RAD_MORPH} signal shapes between locations and participants, it was observed that changes in signal orientation occurred within a few measurements, as depicted in Figure 5.3 a. Upon inspecting the underlying I and Q signals (Figure B.2), it was recognized that their complex representation highly deviated from a circle. Furthermore, changes in orientation were observed within one location between participants (Figure 5.3 b), within one participant between locations (Figure 5.3 c), as well as within one location between measurements, when the breathing pattern was changed (Figure 5.3 d). Moreover, altered signal shapes were identified for measurements at the same locations under different breathing patterns (Figure 5.3 e). Additionally, PW shapes that highly deviated from the well-established PW shapes were detected.

Based on comparisons of PW_{REF_MORPH} and PW_{RAD_MORPH} at the participant level, multiple possible relations between the modalities were observed. On the one hand, signal shapes at one location were temporally and morphologically almost perfectly aligned (Figure 5.4 a). On the other hand, temporal shifts (Figure 5.4 c) and morphological differences (Figure 5.4 d) were detected. Furthermore, measurements with inverted signal shapes were present (Figure 5.4 b).

All PW_{REF_MORPH} and PW_{RAD_MORPH} signals grouped in locations are presented in Appendix B.

Discussion

The noted decrease in signal quality at trunk measurements aligns with existing literature, which states that PPG only captures reliable information at peripheral sites [Per15]. However, this finding is not related to the observed changes in signal orientation. One possible explanation for the inversion behavior between locations of PW_{REF_MORPH} could be the impact of ambient light on the PPG sensor. In most of the PW_{REF_MORPH} signals, the signal orientation seems consistent over the measurement, as the ensemble averages over time do not notably deviate from each other. Since the sensor is detached between measurements to relocate it to the subsequent location, ambient light may fall onto the photodetector, influencing its internal calibration. Contradictory to this conjecture is that the inverting behavior also occurred between measurements where the sensor setup remained unchanged. This was the case at the aorta, where only the breathing pattern changed between subsequent measurements.

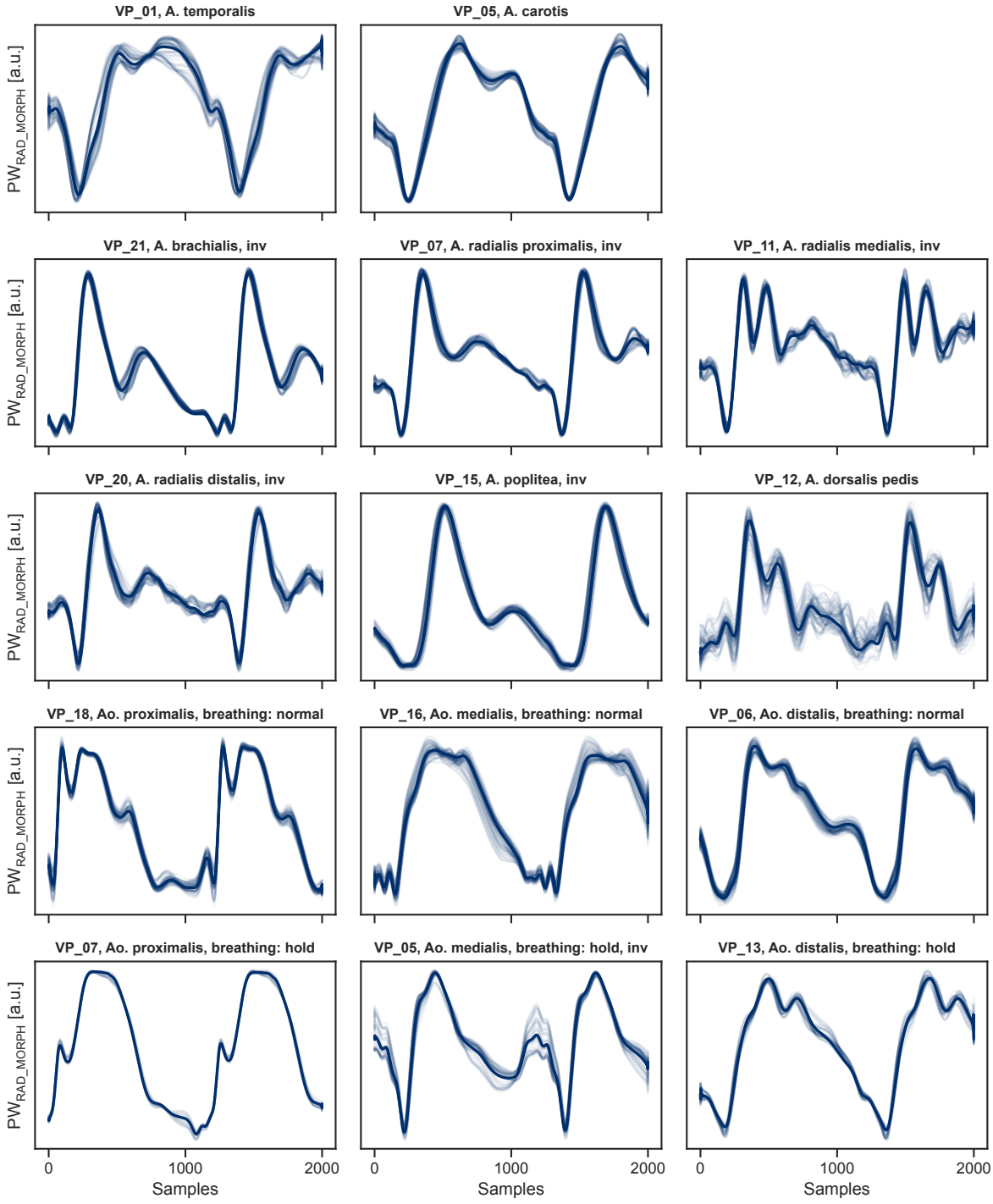

Figure 5.2: Selection of PW_{RAD_MORPH} signals across locations and participants; **inv**: signal was inverted for visualization

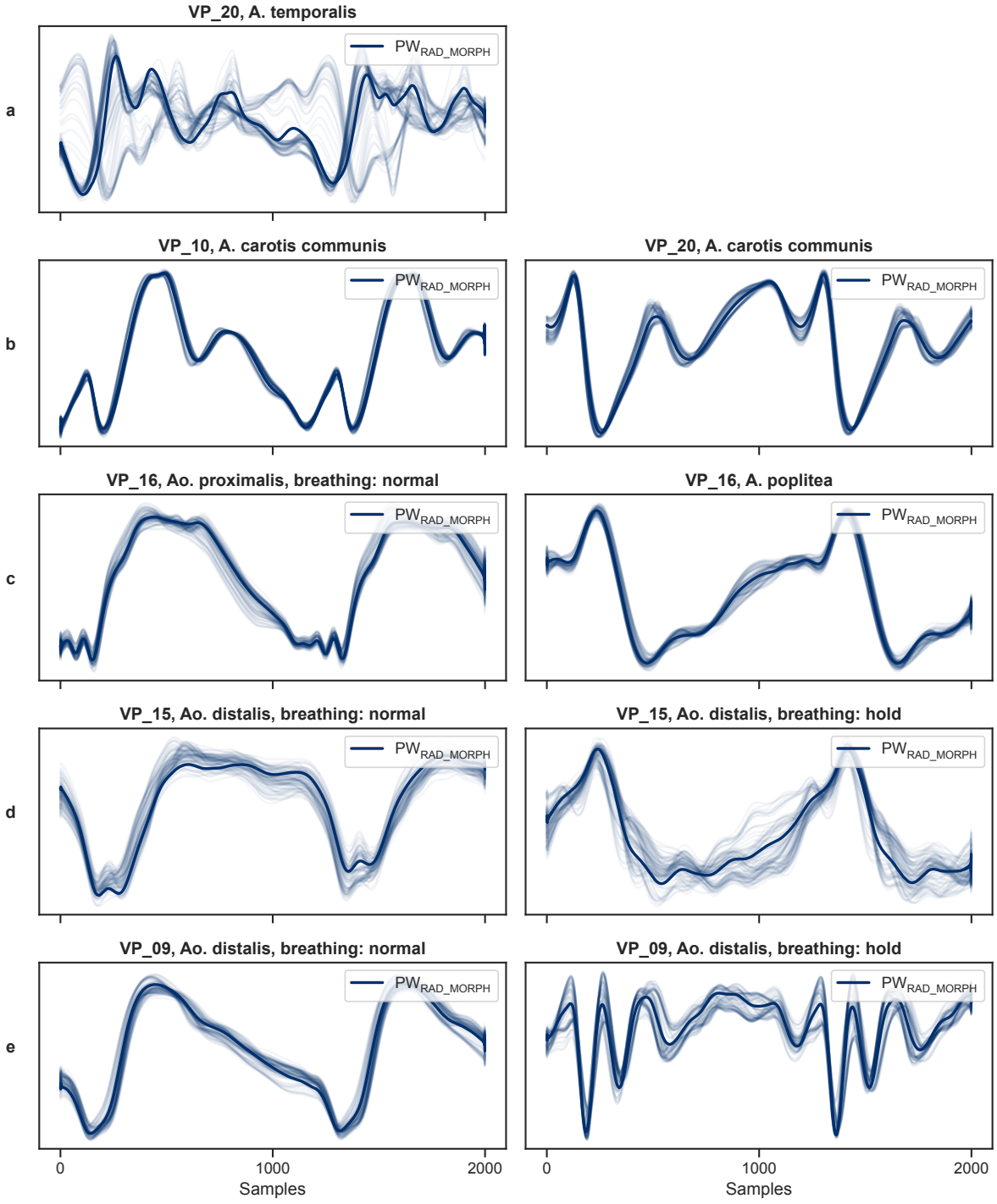

Figure 5.3: Discrepancies in PW_{RAD} recordings; change in orientation a: within one measurement, b: within one location, c: within one participant, d: within one location between measurements; e: deviating signal shapes within one location between measurements

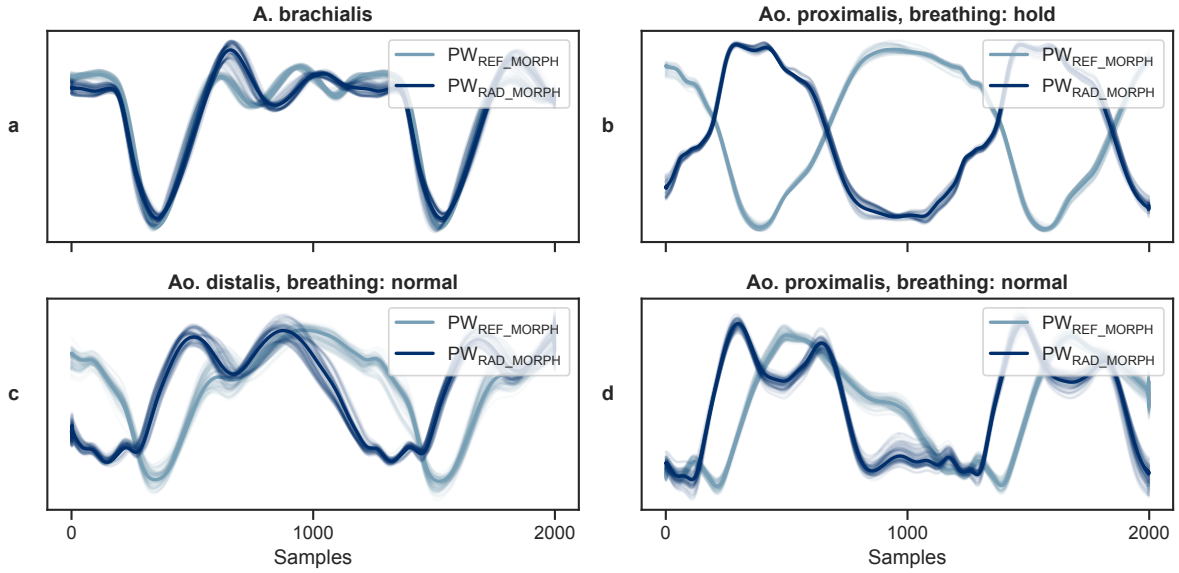

Figure 5.4: Observed possible relations of PW_{REF_MORPH} and PW_{RAD_MORPH} at different locations for VP_14; a: good temporal and morphological alignment; b: inverted signal shapes; c: temporal shift; d: temporal shift and morphological disagreement

In the measurement presented with internal inversion, it appears that either internal or external influences on the body led to a signal distortion. After an artifact, which could occur through movement or reattachment of the sensor, the signal quality improved, but with inverted characteristics. Unfortunately, a possible detachment of the sensor or similar complications during the signal recording can no longer be reconstructed.

Despite the restrictions, it seems that PW detection using radar technology is possible at several body locations over large distances to the heart. It appears that the signal quality decreases with increasing distance to the heart. Since the underlying correct signal shape of the radar-sensed PW is unknown, the observed atypical waveforms make it even more challenging to determine whether the current orientation is correct. From a physiological perspective, the signal shape measured, for example, for VP_16 at A. poplitea is contradictory to the known PW generation and propagation characteristics. A slowly increasing slope with the maximum peak right before the onset of the next PW contradicts these characteristics. By inverting the waveform, a steep increase at the beginning with a slower decrease and local maxima due to reflected waves corresponds closely to the known PW waveform. A conjecture for the inverting behavior within the measurement is that it originates from the reconstruction of the displacement vector. As its complex representation does not even remotely resemble a circle or an ellipse, fitting the barycenter into the data for

offset correction will not provide reasonable results, corrupting the subsequent processing steps. For the orientation changes between measurements, no coherence between the inversion and the reconstruction process was found. The deviating signal shapes within one location between measurements with different breathing patterns suggest that the PW characteristic may not be independent of internal physiological changes.

PW_{REF} and PW_{RAD} show similar behaviors independently from one another, as it seems. The almost perfect temporal and morphological alignment reinforces the assumption that PPG and radar can measure the same physiological principle. However, before quantifying any temporal and morphological properties, the reasons for the inconsistencies within and between modalities, participants, locations, and measurements need to be determined. It needs to be investigated whether the discrepancy results from physiological principles, data acquisition techniques, utilized processing methods, or the manner of application.

5.2 Peripheral Heart Sound Detection

During visual data inspection, two distinct periodically occurring vibrations were observed at all measurement sites, with signal quality varying between participants and locations. Figure 5.5 presents a selection of HS_{RAD_SIG} signals for all locations across participants. Additionally, HSs were manually labeled in the HS_{REF} and HS_{RAD} signals. The dataset consisted of $N = 21$ participants for all locations except A. temporalis, where only $N = 20$ valid signals were available. Furthermore, the A. temporalis signals were only assessed for HS_{RAD}, as no reference data recording was performed at this location. The measurements with different respiration patterns (Ao. proximalis, Ao. medialis, Ao. distalis) were handled separately.

Figure 5.6 presents the number of detected HSs grouped for modality, HS, and measurement location group as defined in Chapter 4.1.2. At all measurement locations, S1 and S2 HSs were identified for HS_{REF} and HS_{RAD} signals, with higher detection rates for the head, neck, and trunk than for the upper and lower extremities. The number of detected HS was comparable between the head and neck versus the trunk, while more HS were identified in the upper extremities than in the lower extremities. When comparing HS_{REF} and HS_{RAD}, they exhibited comparable detection rates for the head and trunk, with a slight advantage for HS_{REF} over HS_{RAD}. For the extremities, HS_{RAD} outperformed HS_{REF}. Within the head and neck, as well as trunk and lower extremity groups, detection rates decreased with increasing distance from the heart, while in the upper extremity, different patterns were present.

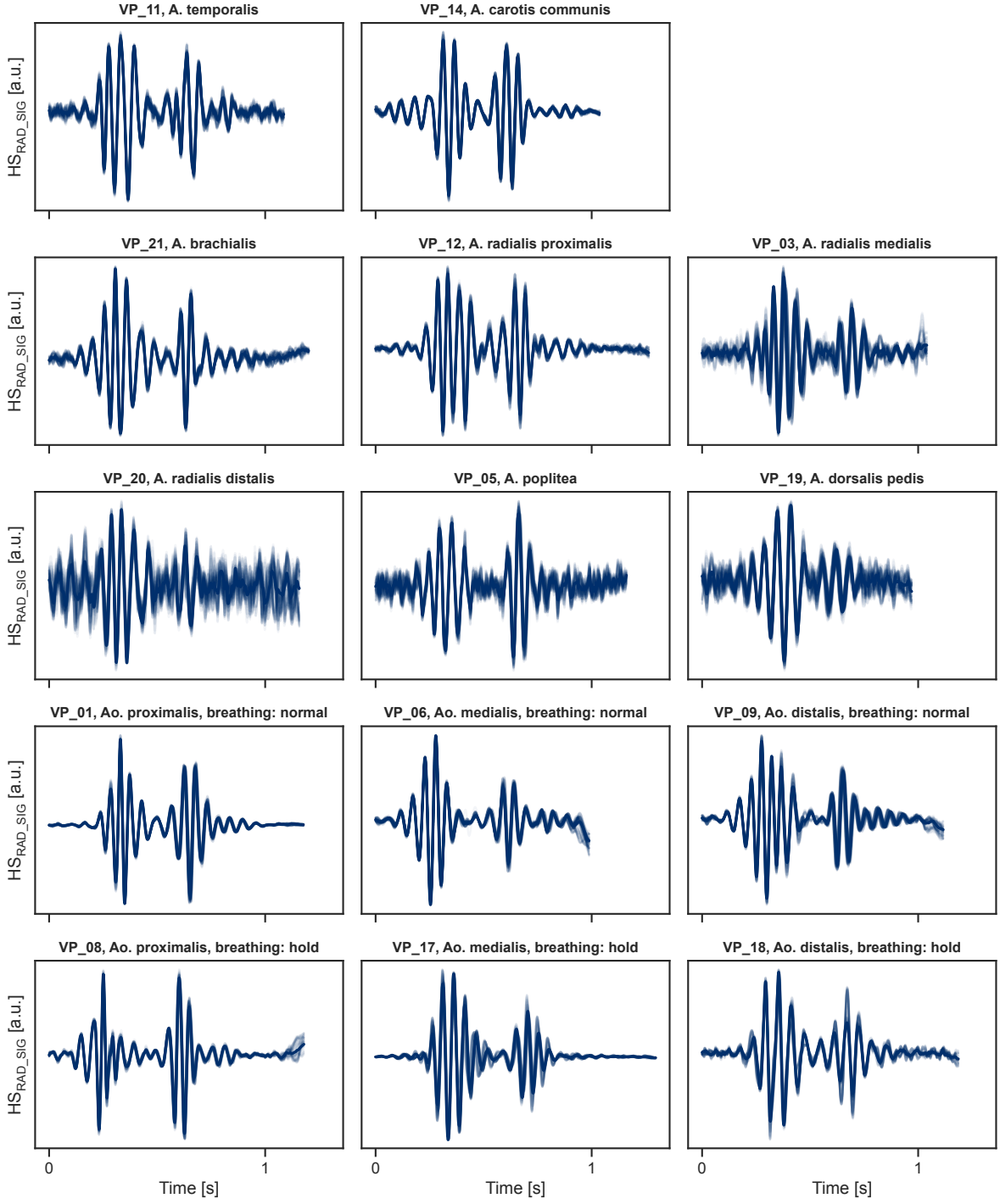

Figure 5.5: Selection of HS_{RAD_SIG} signals across locations and participants

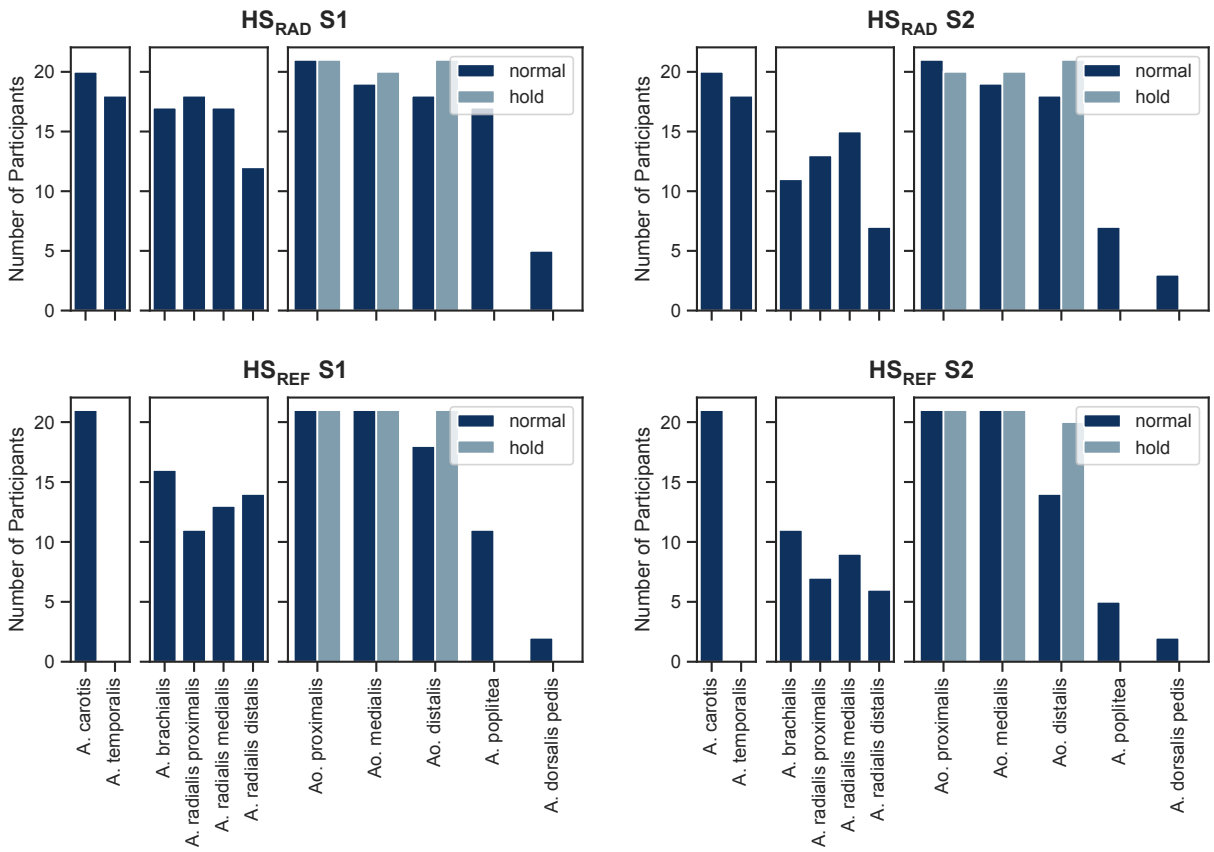

Figure 5.6: Number of detected HSs grouped for modality, HS, measurement location group, and respiration pattern

For HS_{RAD}, the detection rates for A. radialis proximalis and medialis were higher than for A. brachialis for both HSs, while A. radialis distalis was worse. For HS_{REF}, the detection rates for measurements at A. radialis were generally lower than at A. brachialis. Between measurements at the trunk, the recordings with breath-holding mostly showed higher detection rates than when a normal breathing pattern was performed. When comparing S1 and S2, they exhibited similar patterns in both modalities as well as within the groups, with S2 showing lower detection rates.

Throughout the visual inspection, different patterns in the signal quality of HS_{RAD_SIG} were identified, as illustrated in Figure 5.7 a. In measurements, such as at A. carotis communis for VP_14, the temporal ensemble averages and the complete average exhibited only slight differences between each other. In contrast, compared to this measurement, the signal measured at A. temporalis for VP_16 showed notably higher differences over time. Furthermore, a split was detected in HS_{RAD_HE} at several peripheral locations, as illustrated in Figure 5.7 b. Additionally, it was found that at more distal measurement sites, identifiable HS characteristics can be observed, even if the preceding more proximal measurement did not show HS characteristics (Figure 5.7 c).

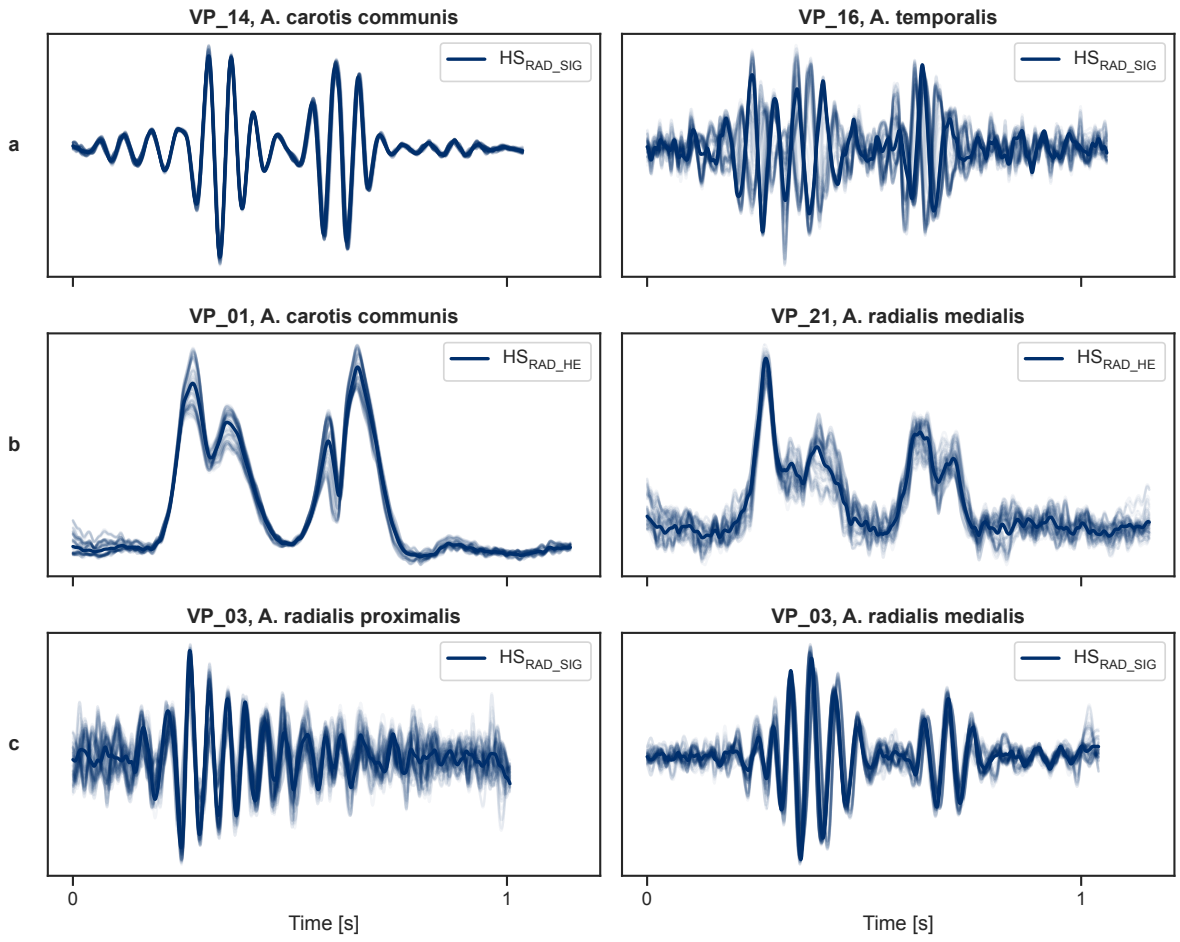

Figure 5.7: Observed HS characteristics during visual inspection; a: different signal quality; b: split detected in envelope; b: different signal characteristics in subsequent measurements

Discussion

The manual labeling process revealed that HSs can be detected at all selected measurement sites. Detection rates, highest at the neck and trunk, decrease with increasing distance from the heart, reaching the lowest performance at the farthest site, the A. dorsalis pedis. The better detectability of S1 compared to S2, particularly at the extremities, requires consideration. During manual labeling, if only one recognizable HS was present in the measurement, it was labeled as S1 for simplicity and due to the lack of knowledge about expected run times. Therefore, such HSs could be either S1, S2, or a combination of both. Consequently, S1 might be slightly overrepresented, while the results for S2 might be underestimated in this results. However, this also allows the conclusion that at extremities, there is a higher likelihood of only one HS being present.

Examining the characteristics over time, some measurements exhibited almost perfect temporal and morphological alignment, while notable changes were observed in others. Given that temporal shifts can result in signal cancellations, these effects need to be considered in the selection of processing steps. Currently, the reasons for the variability in alignment properties between measurements have not been evaluated. Therefore, it is necessary to investigate influencing factors and their evolution over time to determine whether this effect increases with a greater distance to the heart or occurs at specific locations. Additionally, potential inaccuracies due to mismatches during ECG segmentation cannot be excluded.

Regarding the detected split in the HS envelope, Giordano et al., for example, identified the physiological split of S1 into the mitral and tricuspid components and S2 into aortic and pulmonary components within the PCG envelope [Gio19]. Furthermore, Will et al. reported a split in S2 during inspiration in radar-recorded HS signals [Wil18]. Consequently, the observed splits in HS_{RAD_HE} may correspond to the physiological splits of S1 and S2. Remarkably, this characteristic appears not only in measurements at the trunk but also at peripheral measurement sites.

The results, which demonstrate an improvement in signal quality at more distal measurement sites on the upper extremity, may suggest that the detection probability of HSs is not solely dependent on the distance to the heart or related to the signal quality of more proximal sites. The measurement location at the A. brachialis, situated on the inner side of the upper arm, poses challenges due to the limited range of motion of the shoulder, making the horizontal placement of the site often infeasible during signal recording. Additionally, since the placement between A. radialis proximalis and A. radialis medialis remained relatively unchanged between measurements, also the correct identification by ultrasonography or antenna placement could influence the signal quality. Given that tissue properties and physiological phenomena may also contribute, it is evident that the varying signal quality among participants and locations requires further investigation.

5.3 Heart Sound Propagation

In total, 54 features were extracted from the HS_{RAD} signals, comprising 6 generic, 31 temporal, and 17 morphological features. Only the ensemble averages built from the entire signal were evaluated. For the subsequent analysis, all values larger than two SDs from the mean were excluded.

For the generic features calculated from HS_{RAD_SIG}, differences in variance (Figure 5.8) and kurtosis (Figure 5.9) were observed within and between measurement location groups. While trends were noticeable between locations in the head and neck as well as trunk and lower extremity groups, values remained relatively constant at the upper extremity. The variance increased with

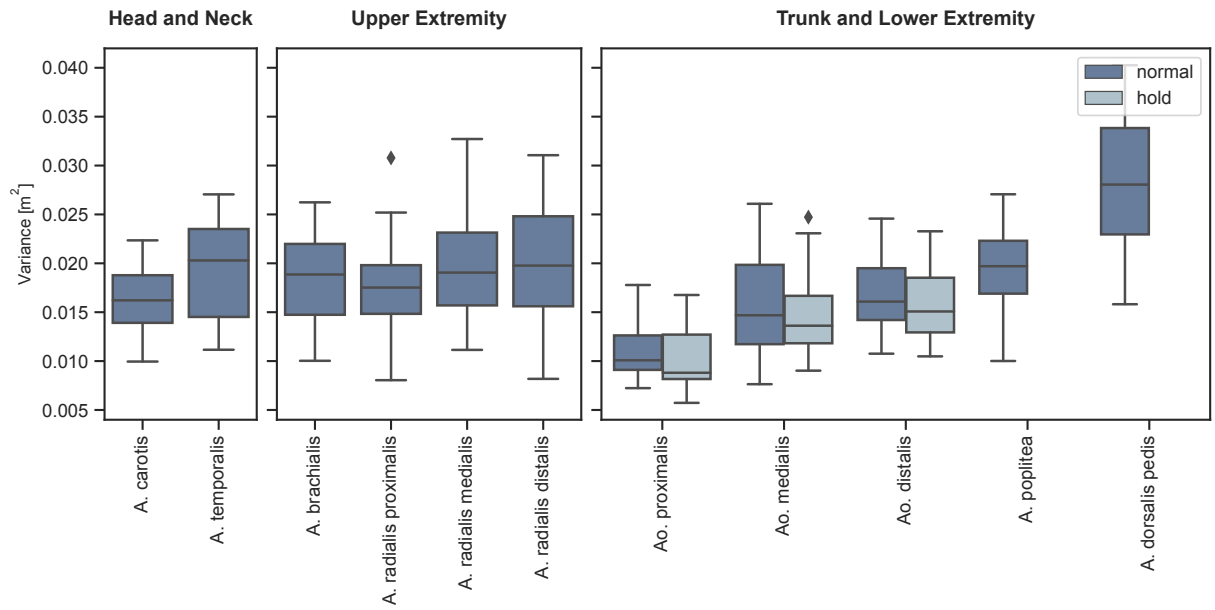

Figure 5.8: Variance derived from HS_{RAD_SIG}

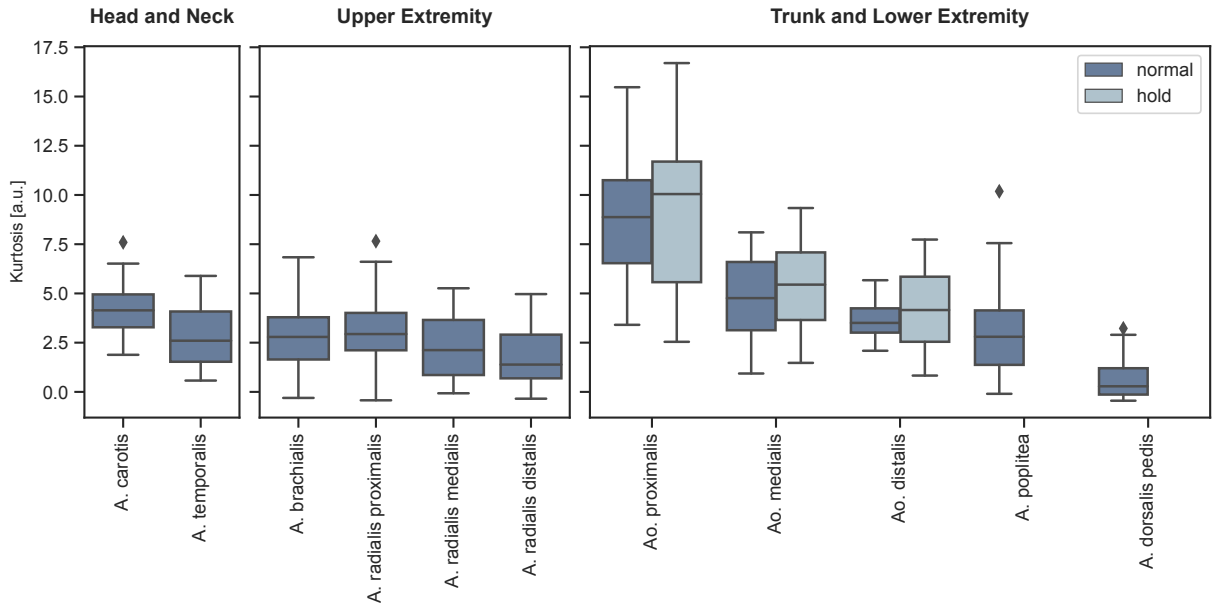

Figure 5.9: Kurtosis derived from HS_{RAD_SIG}

greater distance from the heart, with the lowest average values at Ao. proximalis and highest at A. dorsalis pedis. In contrast, the kurtosis values were higher at more proximal sites, with the average values ranging from 0.68 at A. dorsalis pedis to 9.06 at Ao. proximalis. Slightly lower variance and higher kurtosis values were observed within the breath-holding compared to the normal-breathing measurements.

During the assessment of the S1 duration, which averaged 180 ms, an increase was observed in the periphery within the head and neck as well as trunk and lower extremity groups, with the exception of A. poplitea. Between Ao. proximalis and A. dorsalis pedis, the increase averaged to 57 ms, approximately 40 %. In breath-holding measurements, smaller S1 durations were observed compared to measurements comprising the normal respiration pattern. Within the upper extremity group, no discernible trends between locations were detected. The normalized S1 duration is illustrated in Figure 5.10.

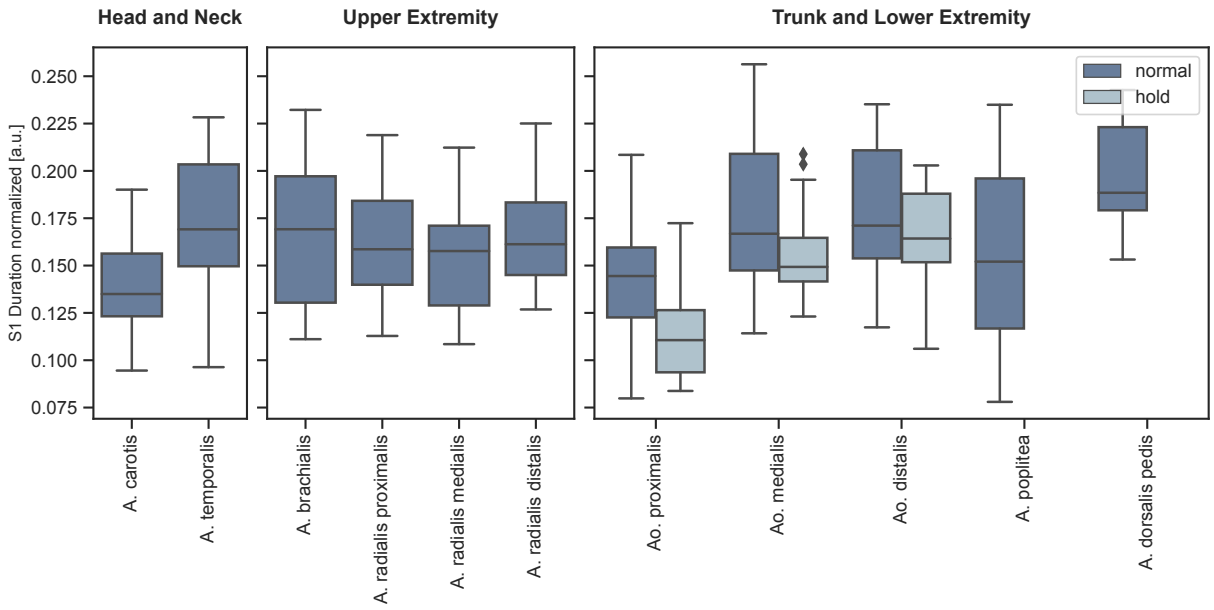

Figure 5.10: Normalized duration of S1

In contrast, the duration of the second HS, averaging 106 ms, showed an increase at the trunk, upper extremities, and lower extremities. From Ao. proximalis to A. dorsalis pedis, the duration increased on average by 30 ms, approximately 38 %. Within the head and neck group, the S2 HSs detected at A. carotis communis lasted longer than those at A. temporalis. Furthermore, higher S2 durations were detected in measurements with the breath-holding respiration pattern than in the comparison group. The duration ratio between S1 and S2 was on average above one at all locations, with the smallest average value of 1.15 at A. carotis communis. While the ratio increased in the periphery for the head and neck, trunk and lower extremities, with A. poplitea as an exception, it decreased between sites located at the upper extremity. For breath-holding measurements, the ratio was smaller than in the respective normal-breathing measurements. No major differences in trends were detected between the normalized and non-normalized duration values.

Within the propagation feature group, individual features yielded similar results for the respective HS. The interval between the R-peak and S1 center, illustrated in Figure 5.11, was relatively constant within the head and neck as well as upper extremity groups. The average propagation times were 120 ms for the head and neck and 165 ms for the upper extremity. At the trunk and lower extremity, the interval increased with distance from the heart, ranging from the lowest value of 54 ms at Ao. proximalis to the highest value of 193 ms at A. dorsalis pedis. A high increase in propagation time was noted in the aorta, with an interval of 97 ms between Ao. proximalis and Ao. distalis. Furthermore, the propagation time between Ao. distalis and A. dorsalis pedis was approximately 42 ms. Interestingly, the interval between the R-peak and S1 onset was shorter at A. temporalis than at A. carotis communis. Additionally, A. temporalis exhibited a higher SD than A. carotis communis in the remaining features.

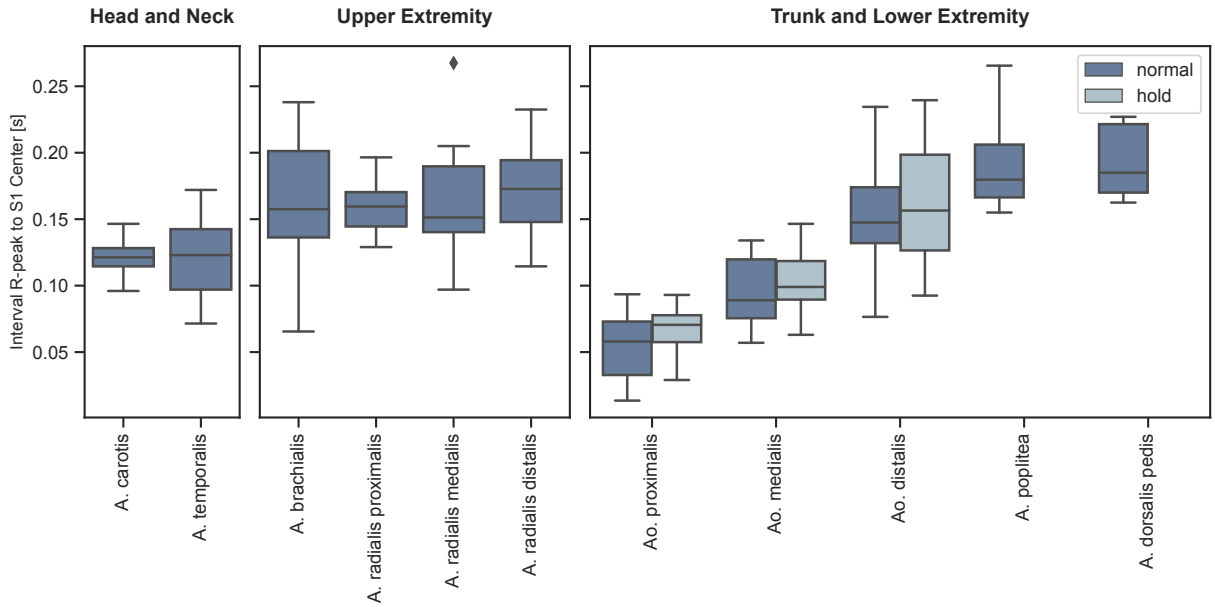

Figure 5.11: Time interval between R-peak and S1 center

Concerning the interval between the R-peak and S2 center, the lowest value of 415 ms was observed at the A. carotis communis, while the highest value of 501 ms was detected at Ao. distalis. Between the neck and head as well as at the trunk, the interval increased peripherally. The span was 20 ms between A. carotis communis and A. temporalis, with an average propagation time of 78 ms between Ao. proximalis and Ao. distalis. No further increase was detected for both A. poplitea and A. dorsalis pedis, but smaller time intervals were measured. At the upper extremity, the interval remained relatively constant. Comparable trends were identified in the normalized intervals, with the lowest value observed at Ao. proximalis rather than A. carotis communis.

When comparing the propagation between HSs, the interval between S1 offset and S2 onset remained relatively constant in the normalized values across the head, neck, and upper extremity. In the non-normalized feature, the values did not exhibit a consistent pattern. Within the trunk and lower extremity group, a negative trend manifested from proximal to distal measurement sites, as illustrated in Figure 5.12. The time interval shortened from Ao. proximalis to Ao. distalis by an average of 59 ms, and another 33 ms from Ao. distalis to A. dorsalis pedis. In contrast, in the feature representing the interval between S1 and S2 onset, the time interval increased between A. carotis and A. temporalis. Furthermore, in the latter measure, the breath-holding measurements showed lower intervals compared to the respective measurements with a normal breathing pattern.

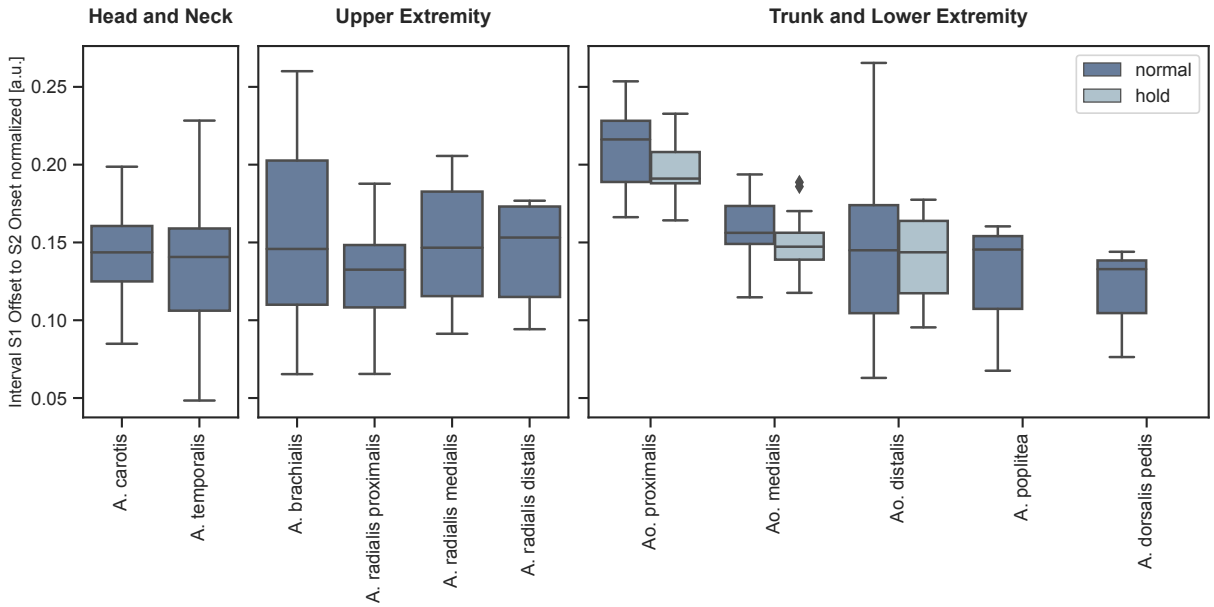

Figure 5.12: Normalized time interval between S1 offset and S2 onset

Considering the amplitude features, P2P amplitudes were roughly twice as high as the amplitude values but did not show any distinct differences in trends. The S1 P2P amplitude, ranging from 0.24 to 46.24 µm, exhibited its highest values at Ao. medialis and decreased in the periphery for all three location groups, presented in Figure 5.13. In contrast, the S2 P2P amplitude ranged from 0.15 to 25.19 µm, with its highest value at A. carotis communis. At the latter site, S2 exhibited a 15-fold higher P2P amplitude compared to A. temporalis, whereas S1 displayed a P2P amplitude of ten times higher. The ratio between S1 and S2 P2P amplitudes, illustrated in Figure 5.14, was on average above one at all locations, with the smallest value at A. carotis communis (1.02) and the highest value at Ao. proximalis (2.27). In general, the head and neck group experienced smaller values than the upper extremities, while the trunk showed higher median values and SDs.

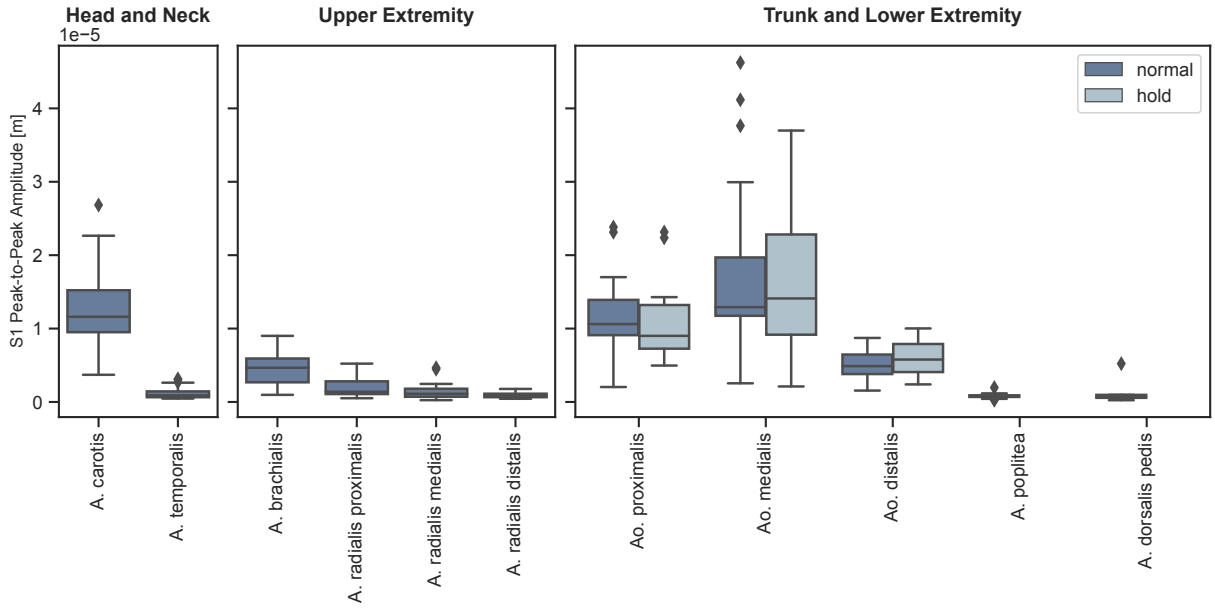

Figure 5.13: P2P amplitude of S1

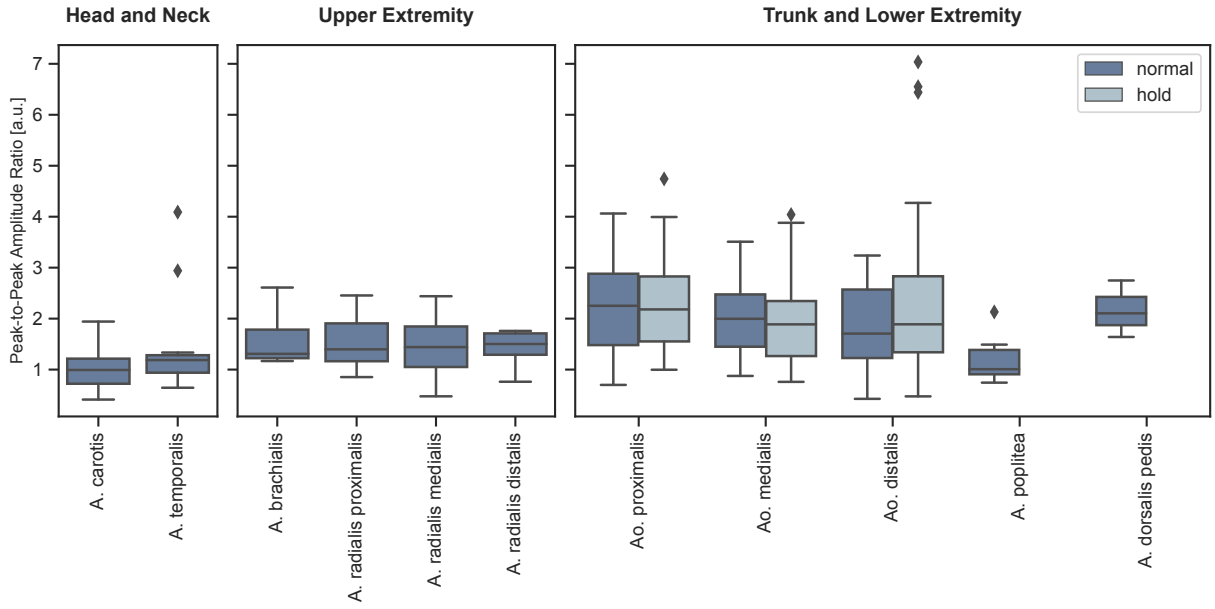

Figure 5.14: P2P amplitude ratio between S1 and S2

The envelope amplitudes for S1 and S2 were within the same ranges as the respective amplitudes and exhibited similar patterns for the locations and the ratio.

The AUC of S1, as shown in Figure 5.15, was, on average over all locations, twice as high as that of S2. For S1, the AUC increased with distance from the heart for all three groups, except at A. poplitea, and reached its maximum values at A. dorsalis pedis. S2 AUC showed a similar pattern, except that the highest value was measured at A. carotis communis, resulting in a negative trend within the head and neck group. Additionally, the AUC increase in the upper extremity group was more pronounced. The ratio between AUC for S1 and S2 was, on average, above one for all locations, with the smallest value at A. carotis communis (1.15).

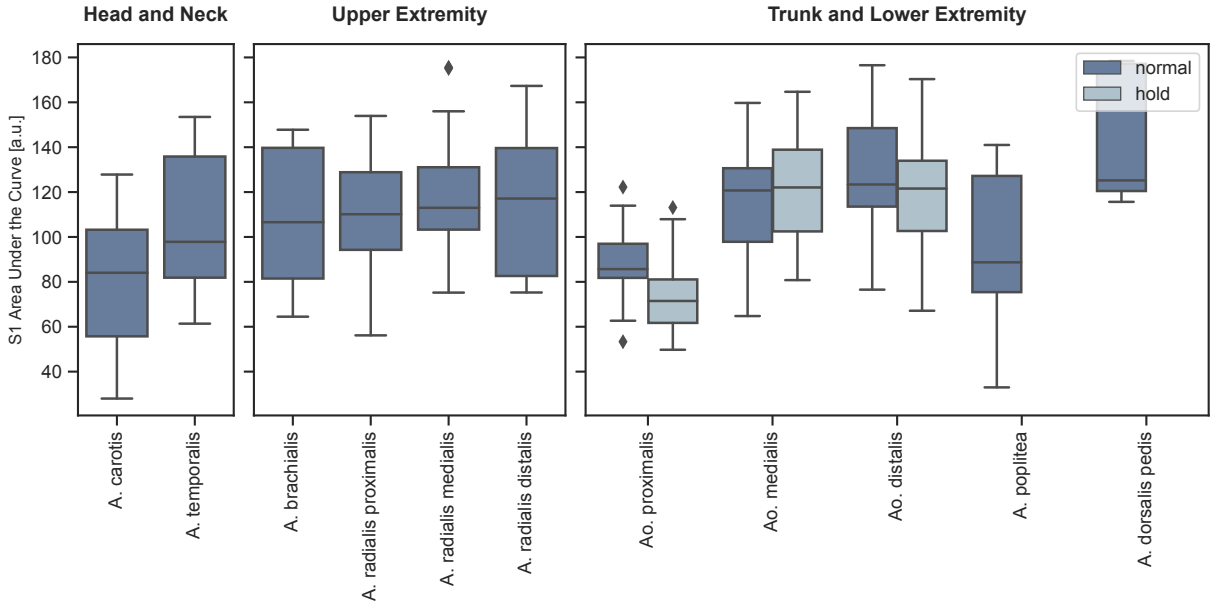

Figure 5.15: AUC of S1

For zero-crossing and symmetry features, no distinct pattern was observable between locations, with the ZCR ratio at all locations averaging one, and symmetry values ranging from 0.2 to 2.6 within the locations. All remaining features are illustrated in Appendix C.

Discussion

Differences in both temporal and morphological properties were evident across the measurement sites. The increase in variance at more distal locations corresponds to the decrease in kurtosis, as both indicate a greater dispersion of the data points and, therefore, a more uniform and less concentrated pattern. In their work, Springer et al. utilized kurtosis as an indicator to assess the quality of phone-recorded HS signals [Spr16]. They anticipated that noisy signals would exhibit

kurtosis values close to those of a Gaussian distribution, while signals with good quality would demonstrate larger values. Given that a kurtosis value of zero aligns with a Gaussian distribution, all locations exhibited higher average values. Since the generic features were calculated on all signals, both variance and kurtosis could potentially serve as indicators of a general lower peripheral signal quality and a lower HS detection rate. Conversely, the varying average values between aortic measurement sites could also suggest less distinct, broader HSs in the periphery. This conjecture is supported by the distally increasing S1 and S2 duration and AUC features, with the broadening effect being more pronounced for S1, as indicated by the duration ratio. When comparing both HSs, not only the duration and AUC are larger for S1 than S2, but also the amplitude is higher for S1. This leads to the inference that, in general, S1 is more prominent in the radar-recorded signal.

Both S1 and S2 exhibited different propagation times at the measurement locations, with the times somehow being related to the expected distances to the heart. Consequently, it is evident that global arterial compliance velocity assessments would be feasible. Concerning the local velocity evaluation, a straightforward approach appears possible at the trunk and lower extremities. However, since the propagation times between the head and neck, as well as within the upper extremity group, did not notably deviate from each other, the local assessment seems more challenging in those regions. To assess feasibility, features need to be evaluated on a participant level and between locations to determine if local velocity calculation is possible and yields consistent results.

Furthermore, different propagation times of S1 and S2 were measured between Ao. proximalis and Ao. distalis. On average, S2 required less time to propagate the same distance as S1. This finding aligns with the decreasing time interval between the HSs in the aortic region. Whether S2 propagates with a different velocity than S1 needs further evaluation in future work. By including, for example, S2 propagation features with the T-wave as reference, S1 and S2 propagation could be reviewed separately.

Regarding the properties of S2, a consistent pattern associated with A. carotis communis was identified. Not only was the duration at A. carotis communis higher than at A. temporalis, but also the highest S2 amplitude and AUC were measured. Additionally, the time interval between the R-peak and the center was the shortest at A. carotis communis. Furthermore, the respective feature ratios exhibited the lowest values around one at this location. Consequently, A. carotis communis appears to be the site where S2 can be detected most prominently, and the characteristics of both HSs are most similar across all measured locations. This observation is consistent with the findings of Will et al., who showed a higher amplitude of S2 at A. carotis communis compared to thoracic sites [Wil18].

Moreover, the average symmetry values and their range across locations may suggest the presence of the physiological split into the valve components, although not consistently. The three options of split not being present, split present with either the first or second component being more distinct, may contribute to the detected unspecific symmetry pattern. To address this, future work should incorporate split detection and investigations to enhance the understanding of the underlying patterns.

Certain limitations need to be acknowledged when interpreting the findings. The presence of HSs varied among participants, resulting in a discrepancy in the number of samples incorporated into the feature extraction across different locations and individual HSs. While the trunk, neck, and head benefitted from an almost complete dataset, the extremities, particularly for S2 and in the lower extremities, faced limitations in the number of available samples. Consequently, features derived for S2 in the extremities, as well as ratios or features describing the relationship between both HSs, might present an inaccurate representation due to reliance on a limited number of observations.

Furthermore, the feature extraction is influenced by the subjective segmentation of HSs during visual data inspection, as this was incorporated as prior knowledge into the HS segmentation. Consequently, to enhance the objectivity of the segmentation ground truth, the manual labeling process should be repeated by experts. Additionally, the representation of features is impacted by the classification of a single present HS as S1. This classification can result in features exhibiting different average values or higher SDs, potentially leading to incorrect conclusions. Therefore, in future work, observations with two present HSs should be assessed separately from those with only one. By comparing the results, it may be possible to identify which phenomenon was detected; S1, S2, or a combination of both.

Finally, since the evaluation is performed on a single signal derived from the entire recording at a specific location, physiologically induced changes, such as those caused by respiration, might be averaged. To better understand the potential impact of physiological factors on temporal and morphological properties, in future work, HS signals should be assessed in shorter time segments as well.

5.4 General Discussion and Limitations

Despite the limitations regarding PW assessment, the results indicate that PWs and HSs can be detected using the proposed measurement setup and processing steps across the whole body by radar technology.

Upon comparing the average HR across different body locations, it was observed that the heart's activity was higher at the beginning of the signal recording, particularly during the baseline and measurements at A. carotis and A. temporalis. Moreover, an increased HR was also noted during the measurement at A. poplitea. Consequently, the assumption that the physiological state of a participant remains constant throughout the entire data recording is not valid. The study procedure systematically introduced a higher HR at certain locations, potentially influencing the propagation evaluation. Given that features related to S2 or those assessing the relationship between S1 and S2 appeared to be influenced by the underlying HR, it is advisable to address this effect. One possible approach is to both extend the baseline duration and introduce an additional baseline time interval after the participant transitions from a supine to a prone position for the last measurement.

Moreover, the preparatory tasks preceding signal recording presented additional challenges. Although the identification of most measurement sites was straightforward, locating the A. dorsalis pedis using ultrasonography proved to be particularly challenging. Additionally, the positioning of the radar antenna and placement of the reference sensor were in some cases not trivial due to interindividual differences, resulting in variations among participants. Furthermore, some participants experienced difficulty holding their breath and performed irregular, shallow breathing patterns instead. In conclusion, the integral components of signal recording should be further investigated and standardized in future work.

Another limitation of the proposed work is the lack of an automatic process for HS segmentation. In this work, prior knowledge generated through manual labeling was incorporated. However, this approach is not feasible for large-scale data evaluation. Since segmentation plays an integral role in evaluating signal characteristics, there is a need to explore and develop algorithms not only for HS segmentation but also for PW segmentation.

Finally, the data acquisition included only participants from a restricted, young, and healthy population. Consequently, no conclusions can be drawn regarding the applicability of this measurement procedure to investigate the health status of patients. In general, the acquisition was carried out in a highly standardized laboratory setting, which is currently not applicable in a real-world scenario.

Chapter 6

Conclusion and Outlook

In the scope of this thesis, a dataset was recorded to assess the feasibility of detecting PWs and HSs at peripheral body locations. In total, 11 measurement sites above arteries were selected from the head down to the foot. Reference and radar signals were recorded at each location.

At all locations, PWs were detected in the reference and radar signal through visual inspection of ensemble averages built from the entire recording at each site. Despite this promising result, several inconsistencies were found, making further evaluation infeasible. The reference PPG and radar PW shapes exhibited an inverting behavior with a seemingly random occurrence pattern. Additionally, the alignment between both modalities varied. On the one hand, a temporal shift was observed, while on the other hand, signal shapes between the modalities were detected as diverging and inverted to one another. Since perfect temporal and morphological alignment was observed as well, it is assumed that both modalities captured the same physiological phenomenon.

Similar to the PW detection approach, the HS radar and reference signals were visually inspected. HSs were detected in both modalities at all investigated sites. The results indicated high detection rates at the trunk and neck, while the rates at upper and lower extremities were lower. After establishing feasibility, the characteristics of radar-sensed HS propagation were assessed. Features related to timing and morphology revealed notable differences in propagation times between body parts. Additionally, the HS amplitude, duration, and AUC were found to be highly dependent on the measurement region.

To achieve a more comprehensive understanding of the propagation of PWs and HSs within the human body, it is essential to first investigate the underlying reasons for the data discrepancies within and between modalities. The entire process, starting from fundamental aspects of physiology to the devices and procedures employed for data acquisition, along with the associated processing techniques, requires critical analysis. Additionally, factors influencing signal quality need to be

thoroughly investigated. Given the reduced number of available samples, especially in the lower extremities, the information contained is limited. In this process, both the acquired anthropometric data and the information generated during the ultrasonography examination should be included. Gaining insights into tissue properties might offer valuable perspectives. In any case, consideration should be given to increasing the size of the dataset.

Additionally, the feature set describing the propagation characteristics should be extended in future work. Not only should properties regarding PW timing and configuration be added, but the HS signal should also be evaluated more closely. This could involve deriving properties from shorter time frames, different respiration phases, and between measurement locations. Furthermore, the coherence between PW and HS propagation, as well as the coherence between individual HSs, still requires investigation. To achieve this, algorithms, such as those for segmentation, need to be developed. These algorithms need to account for signals with varying run times and shapes.

Furthermore, future studies could aim to extend knowledge about the applicability of radar technology in providing information about a patient's health status beyond obtaining BR, HR, and HRV. The evaluation of PWV generates essential information about arterial properties. The use of a radar-based system could potentially reduce procedural burden while providing information in a contactless manner. As this work demonstrated that HS propagation measurement is feasible, not only global PWV assessment but also HS velocity evaluation could be the focus of future work. The prerequisites for radar-based local velocity assessment were already included in the data acquisition for this study. Additionally, data with higher granularity could provide valuable insights. In general, a dataset with participants suffering from cardiovascular pathologies should be generated. One research approach could involve comparing velocities between the already recorded healthy control group and a group of patients suffering from hypertension. Through this comparison, it would be feasible to assess whether radar technology can evaluate arterial compliance and can be used as a diagnostic tool. Another study could focus on the contactless diagnosis and monitoring of cardiac valve abnormalities, as automatic identification and classification of abnormal HSs is an ongoing research area. In summary, further investigation of PW and HS propagation and morphology using radar technology could allow for the contactless assessment of various medical conditions beyond the current scope.

List of Figures

List of Tables

Bibliography

[All00] John Allen and Alan Murray. “Similarity in Bilateral Photoplethysmographic Peripheral Pulse Wave Characteristics at the Ears, Thumbs and Toes”. In: *Physiological Measurement* 21.3 (Aug. 1, 2000), pp. 369–377. ISSN: 0967-3334, 1361-6579. DOI: 10.1088/0967-3334/21/3/303. URL: https://iopscience.iop.org/article/10.1088/0967-3334/21/3/303 (visited on 12/27/2023).

[Bra19] Ralf Brandes, Florian Lang, and Robert F. Schmidt, eds. *Physiologie des Menschen: mit Pathophysiologie*. Springer-Lehrbuch. Berlin, Heidelberg: Springer Berlin Heidelberg, 2019. ISBN: 978-3-662-56468-4. DOI: 10.1007/978-3-662-56468-4. URL: http://link.springer.com/10.1007/978-3-662-56468-4 (visited on 08/01/2023).

[Bun19] Gitte Bunkenborg, Ingrid Poulsen, Karin Samuelson, Steen Ladelund, and Jonas Akeson. “Bedside Vital Parameters That Indicate Early Deterioration”. In: *International Journal of Health Care Quality Assurance* 32.1 (Feb. 11, 2019), pp. 262–272. ISSN: 0952-6862. DOI: 10.1108/IJHCQA-10-2017-0206. URL: https://www.emerald.com/insight/content/doi/10.1108/IJHCQA-10-2017-0206/full/html (visited on 12/29/2023).

[Chu16] Matthew M. Churpek, Richa Adhikari, and Dana P. Edelson. “The Value of Vital Sign Trends for Detecting Clinical Deterioration on the Wards”. In: *Resuscitation* 102 (May 2016), pp. 1–5. ISSN: 03009572. DOI: 10.1016/j.resuscitation.2016.02.005. URL: https://linkinghub.elsevier.com/retrieve/pii/S0300957216000770 (visited on 12/30/2023).

[Dar15] Mohamad Ayham Darwich, François Langevin, and Khaldoun Darwich. “Local Pulse Wave Velocity Estimation in the Carotids Using Dynamic MR Sequences”. In: *Journal of Biomedical Science and Engineering* 08.04 (2015), pp. 227–236. ISSN: 1937-6871, 1937-688X. DOI: 10.4236/jbise.2015.84022. URL: http://www.scirp.org/journal/doi.aspx?DOI=10.4236/jbise.2015.84022 (visited on 12/26/2023).

[Deh19] Parastoo Dehkordi, Farzad Khosrow-Khavar, Marco Di Rienzo, Omer T. Inan, Samuel E. Schmidt, Andrew P. Blaber, Kasper Sørensen, Johannes J. Struijk, Vahid Zakeri, Prospero Lombardi, Md. Mobashir H. Shandhi, Mojtaba Borairi, John M. Zanetti, and Kouhyar Tavakolian. "Comparison of Different Methods for Estimating Cardiac Timings: A Comprehensive Multimodal Echocardiography Investigation". In: *Frontiers in Physiology* 10 (Aug. 22, 2019), p. 1057. ISSN: 1664-042X. DOI: 10.3389/fphys.2019.01057. URL: https://www.frontiersin.org/article/10.3389/fphys.2019.01057/full (visited on 12/31/2023).

[Dis20] Theekshana Dissanayake, Tharindu Fernando, Simon Denman, Sridha Sridharan, Houman Ghaemmaghami, and Clinton Fookes. *A Robust Interpretable Deep Learning Classifier for Heart Anomaly Detection Without Segmentation*. Sept. 29, 2020. DOI: 10.48550/arXiv.2005.10480. arXiv: 2005.10480 [cs, eess, q-bio]. URL: http://arxiv.org/abs/2005.10480 (visited on 11/27/2023). preprint.

[Dur20] Fatma Dursun Ergezen and Emine Kol. "Nurses' Responses to Monitor Alarms in an Intensive Care Unit: An Observational Study". In: *Intensive and Critical Care Nursing* 59 (Aug. 2020), p. 102845. ISSN: 09643397. DOI: 10.1016/j.iccn.2020.102845. URL: https://linkinghub.elsevier.com/retrieve/pii/S0964339720300483 (visited on 12/29/2023).

[Emp23] EmpkinS. *Website of the CRC 1483 EmpkinS*. 2023. URL: https://www.empkins.de/ (visited on 11/24/2023).

[Eva01] David Evans, Brent Hodgkinson, and Judith Berry. "Vital Signs in Hospital Patients: A Systematic Review". In: *International Journal of Nursing Studies* 38.6 (Dec. 2001), pp. 643–650. ISSN: 00207489. DOI: 10.1016/S0020-7489(00)00119-X. URL: https://linkinghub.elsevier.com/retrieve/pii/S002074890000119X (visited on 12/30/2023).

[Fab64] J. Jab Faber. "Origin and Conduction of the Mitral Sound in the Heart". In: *Circulation Research* 14.5 (May 1964), pp. 426–435. ISSN: 0009-7330, 1524-4571. DOI: 10.1161/01.RES.14.5.426. URL: https://www.ahajournals.org/doi/10.1161/01.RES.14.5.426 (visited on 12/28/2023).

[Far63] J. Job Farber and James H. Purvis. "Conduction of Cardiovascular Sound Along Arteries". In: *Circulation Research* 12.3 (Mar. 1963), pp. 308–316. ISSN: 0009-7330, 1524-4571. DOI: 10.1161/01.RES.12.3.308. URL: https://www.ahajournals.org/doi/10.1161/01.RES.12.3.308 (visited on 07/31/2023).

[For19] Mohamad Forouzanfar, Fiona C. Baker, Ian M. Colrain, Aimée Goldstone, and Massimiliano De Zambotti. "Automatic Analysis of Pre-ejection Period during Sleep Using Impedance Cardiogram". In: *Psychophysiology* 56.7 (July 2019), e13355. ISSN: 0048-5772, 1469-8986. DOI: 10.1111/psyp.13355. URL: https://onlinelibrary.wiley.com/doi/10.1111/psyp.13355 (visited on 01/02/2024).

[Fra14] Piero Colli Franzone, Luca Franco Pavarino, and Simone Scacchi. *Mathematical Cardiac Electrophysiology*. Springer, Oct. 30, 2014. 410 pp. ISBN: 978-3-319-04801-7. Google Books: H7shBQAAQBAJ.

[Gar24] Kenneth E. Gard, David Dries, and Chad House. "Performing Accurate Standard 12 Lead ECGs on Patients with Burns to the Chest". In: *Air Medical Journal* 43.1 (Jan. 2024), pp. 8–10. ISSN: 1067991X. DOI: 10.1016/j.amj.2023.11.001. URL: https://linkinghub.elsevier.com/retrieve/pii/S1067991X23002444 (visited on 12/30/2023).

[Ger07] Marc Gertsch. *Das EKG: Auf einen Blick und im Detail*. Berlin, Heidelberg: Springer Berlin Heidelberg, 2007. ISBN: 978-3-540-34372-1. DOI: 10.1007/978-3-540-34372-1. URL: https://link.springer.com/10.1007/978-3-540-34372-1 (visited on 07/30/2023).

[Gio19] Noemi Giordano and Marco Knaflitz. "A Novel Method for Measuring the Timing of Heart Sound Components through Digital Phonocardiography". In: *Sensors* 19.8 (Apr. 19, 2019), p. 1868. ISSN: 1424-8220. DOI: 10.3390/s19081868. URL: https://www.mdpi.com/1424-8220/19/8/1868 (visited on 11/28/2023).

[Has22] Kareeb Hasan, Malikeh P. Ebrahim, Hongqiang Xu, and Mehmet R. Yuce. "Analysis of Spectral Estimation Algorithms for Accurate Heart Rate and Respiration Rate Estimation Using an Ultra-Wideband Radar Sensor". In: *IEEE Reviews in Biomedical Engineering* (2022), pp. 1–14. ISSN: 1937-3333, 1941-1189. DOI: 10.1109/RBME.2022.3212695. URL: https://ieeexplore.ieee.org/document/9913662/ (visited on 12/28/2023).

[Her07] Evelien Hermeling, Koen D. Reesink, Robert S. Reneman, and Arnold P.G. Hoeks. "Measurement of Local Pulse Wave Velocity: Effects of Signal Processing on Precision". In: *Ultrasound in Medicine & Biology* 33.5 (May 2007), pp. 774–781. ISSN: 03015629. DOI: 10.1016/j.ultrasmedbio.2006.11.018. URL: https://linkinghub.elsevier.com/retrieve/pii/S030156290601934X (visited on 12/27/2023).

[Her22] Liv Herzer, Annika Muecke, Robert Richer, Nils C. Albrecht, Markus Heyder, Katharina M. Jaeger, Veronika Koenig, Alexander Koelpin, Nicolas Rohleder, and Bjoern M. Eskofier. "Influence of Sensor Position and Body Movements on Radar-Based Heart Rate Monitoring". In: *2022 IEEE-EMBS International Conference on Biomedical and Health Informatics (BHI)*. 2022 IEEE-EMBS International Conference on Biomedical and Health Informatics (BHI). Ioannina, Greece: IEEE, Sept. 27, 2022, pp. 1–4. ISBN: 978-1-66548-791-7. DOI: 10.1109/BHI56158.2022.9926775. URL: https://ieeexplore.ieee.org/document/9926775/ (visited on 11/28/2023).

[Kah18] Martina Kahl-Scholz, ed. *Basisdiagnostik in der Inneren Medizin: Perkussion, Auskultation, Palpation*. Springer-Lehrbuch. Berlin, Heidelberg: Springer Berlin Heidelberg, 2018. ISBN: 978-3-662-56153-9. DOI: 10.1007/978-3-662-56153-9. URL: http://link.springer.com/10.1007/978-3-662-56153-9 (visited on 12/29/2023).

[Keb20] Mamady Kebe, Rida Gadhafi, Baker Mohammad, Mihai Sanduleanu, Hani Saleh, and Mahmoud Al-Qutayri. "Human Vital Signs Detection Methods and Potential Using Radars: A Review". In: *Sensors* 20.5 (5 Jan. 2020), p. 1454. ISSN: 1424-8220. DOI: 10.3390/s20051454. URL: https://www.mdpi.com/1424-8220/20/5/1454 (visited on 12/28/2023).

[Kla11] Richard Klabunde. *Cardiovascular Physiology Concepts*. Lippincott Williams & Wilkins, Nov. 3, 2011. 257 pp. ISBN: 978-1-4511-1384-6. Google Books: 27ExgvGnOagC.

[Kon97] T Kondo, T Uhlig, P Pemberton, and Pd Sly. "Laser Monitoring of Chest Wall Displacement". In: *European Respiratory Journal* 10.8 (Aug. 1, 1997), pp. 1865–1869. ISSN: 0903-1936, 1399-3003. DOI: 10.1183/09031936.97.10081865. URL: http://erj.ersjournals.com/lookup/doi/10.1183/09031936.97.10081865 (visited on 12/25/2023).

[Kub70] W. G. Kubicek, R. P. Patterson, and D. A. Witsoe. "Impedance Cardiography as a Noninvasive Method of Monitoring Cardiac Function and Other Parameters of the Cardiovascular System*". In: *Annals of the New York Academy of Sciences* 170.2 (1970), pp. 724–732. ISSN: 1749-6632. DOI: 10.1111/j.1749-6632.1970.tb17735.x. URL: https://onlinelibrary.wiley.com/doi/abs/10.1111/j.1749-6632.1970.tb17735.x (visited on 11/26/2023).

[Lau06] S. Laurent, J. Cockcroft, L. Van Bortel, P. Boutouyrie, C. Giannattasio, D. Hayoz, B. Pannier, C. Vlachopoulos, I. Wilkinson, H. Struijker-Boudier, and on behalf of the European Network for Non-invasive Investigation of Large Arteries. "Expert Consen-

sus Document on Arterial Stiffness: Methodological Issues and Clinical Applications". In: *European Heart Journal* 27.21 (Sept. 25, 2006), pp. 2588–2605. ISSN: 0195-668X, 1522-9645. DOI: 10.1093/eurheartj/ehl254. URL: https://academic.oup.com/eurheartj/article-lookup/doi/10.1093/eurheartj/ehl254 (visited on 12/26/2023).

[Lec23] Lecturio. *Lecturio Medical - Cardiac Cycle*. 2023. URL: https://www.lecturio.com/concepts/cardiac-cycle/ (visited on 11/24/2023).

[Lev13] J. R. Levick. *An Introduction to Cardiovascular Physiology*. Butterworth-Heinemann, Oct. 22, 2013. 288 pp. ISBN: 978-1-4831-8384-8. Google Books: nL_dAgAAQBAJ.

[Li13] Changzhi Li, Victor M. Lubecke, Olga Boric-Lubecke, and Jenshan Lin. "A Review on Recent Advances in Doppler Radar Sensors for Noncontact Healthcare Monitoring". In: *IEEE Transactions on Microwave Theory and Techniques* 61.5 (May 2013), pp. 2046–2060. ISSN: 0018-9480, 1557-9670. DOI: 10.1109/TMTT.2013.2256924. URL: http://ieeexplore.ieee.org/document/6504804/ (visited on 07/28/2023).

[Lin14] Jenshan Lin and Wenhsing Wu. "Vital Sign Radars: Past, Present, and Future". In: *WAMICON 2014*. 2014 IEEE 15th Annual IEEE Wireless and Microwave Technology Conference (WAMICON). Tampa, FL, USA: IEEE, June 2014, pp. 1–4. ISBN: 978-1-4799-4608-2. DOI: 10.1109/WAMICON.2014.6857798. URL: http://ieeexplore.ieee.org/document/6857798/ (visited on 07/30/2023).

[Loh22] Hui Wen Loh, Shuting Xu, Oliver Faust, Chui Ping Ooi, Prabal Datta Barua, Subrata Chakraborty, Ru-San Tan, Filippo Molinari, and U Rajendra Acharya. "Application of Photoplethysmography Signals for Healthcare Systems: An in-Depth Review". In: *Computer Methods and Programs in Biomedicine* 216 (Apr. 2022), p. 106677. ISSN: 01692607. DOI: 10.1016/j.cmpb.2022.106677. URL: https://linkinghub.elsevier.com/retrieve/pii/S0169260722000621 (visited on 12/23/2023).

[Mak21] Dominique Makowski, Tam Pham, Zen J. Lau, Jan C. Brammer, François Lespinasse, Hung Pham, Christopher Schölzel, and S. H. Annabel Chen. "NeuroKit2: A Python Toolbox for Neurophysiological Signal Processing". In: *Behavior Research Methods* 53.4 (Aug. 2021), pp. 1689–1696. ISSN: 1554-3528. DOI: 10.3758/s13428-020-01516-y. URL: https://link.springer.com/10.3758/s13428-020-01516-y (visited on 11/27/2023).

[Man13] Giuseppe Mancia et al. "2013 ESH/ESC Guidelines for the Management of Arterial Hypertension: The Task Force for the Management of Arterial Hypertension of the European Society of Hypertension (ESH) and of the European Society of Cardiology

(ESC)". In: *European Heart Journal* 34.28 (July 2013), pp. 2159–2219. ISSN: 1522-9645. DOI: 10.1093/eurheartj/eht151. pmid: 23771844.

[Mar06] Andrés Martínez, Estrella Everss, José Luis Rojo-Álvarez, and Domingo Pascual Fig. "A Systematic Review of the Literature on Home Monitoring for Patients with He..." In: *Journal of Telemedicine and Telecare* 12.5 (July 2006), pp. 234–241. DOI: 10.1258/135763306777889109.

[McG16] Susan P. McGrath, Andreas H. Taenzer, Nancy Karon, and George Blike. "Surveillance Monitoring Management for General Care Units: Strategy, Design, and Implementation". In: *The Joint Commission Journal on Quality and Patient Safety* 42.7 (July 2016), pp. 293–302. ISSN: 15537250. DOI: 10.1016/S1553-7250(16)42040-4. URL: https://linkinghub.elsevier.com/retrieve/pii/S1553725016420404 (visited on 08/03/2023).

[Mic19] Fabian Michler, Kilin Shi, Sven Schellenberger, Tobias Steigleder, Anke Malessa, Laura Hameyer, Nina Neumann, Fabian Lurz, Christoph Ostgathe, Robert Weigel, and Alexander Koelpin. "A Clinically Evaluated Interferometric Continuous-Wave Radar System for the Contactless Measurement of Human Vital Parameters". In: *Sensors* 19.11 (May 31, 2019), p. 2492. ISSN: 1424-8220. DOI: 10.3390/s19112492. URL: https://www.mdpi.com/1424-8220/19/11/2492 (visited on 04/18/2023).

[Mil22] M.G. Manisha Milani, Pg Emeroylariffion Abas, and Liyanage C. De Silva. "A Critical Review of Heart Sound Signal Segmentation Algorithms". In: *Smart Health* 24 (June 2022), p. 100283. ISSN: 23526483. DOI: 10.1016/j.smhl.2022.100283. URL: https://linkinghub.elsevier.com/retrieve/pii/S2352648322000186 (visited on 10/05/2023).

[Mil90] William R. Milnor. *Cardiovascular Physiology*. Oxford University Press, 1990. 526 pp. ISBN: 978-0-19-505884-0. Google Books: 1duFI886FxIC.

[Mur20] Christopher J L Murray et al. "Global Burden of 87 Risk Factors in 204 Countries and Territories, 1990–2019: A Systematic Analysis for the Global Burden of Disease Study 2019". In: *The Lancet* 396.10258 (Oct. 2020), pp. 1223–1249. ISSN: 01406736. DOI: 10.1016/S0140-6736(20)30752-2. URL: https://linkinghub.elsevier.com/retrieve/pii/S0140673620307522 (visited on 08/18/2023).

[Nab20] P. M. Nabeel, V. Raj Kiran, Jayaraj Joseph, V. V. Abhidev, and Mohanasankar Sivaprakasam. "Local Pulse Wave Velocity: Theory, Methods, Advancements, and Clinical Applications". In: *IEEE Reviews in Biomedical Engineering* 13 (2020), pp. 74–112.

ISSN: 1937-3333, 1941-1189. DOI: 10.1109/RBME.2019.2931587. URL: https://ieeexplore.ieee.org/document/8778763/ (visited on 12/26/2023).

[Nag15] Mohsen Naghavi, Haidong Wang, Rafael Lozano, Adrian Davis, Xiaofeng Liang, Maigeng Zhou, and Stein Emil Vollset. "Global, Regional, and National Age–Sex Specific All-Cause and Cause-Specific Mortality for 240 Causes of Death, 1990–2013: A Systematic Analysis for the Global Burden of Disease Study 2013". In: *The Lancet* 385.9963 (Jan. 10, 2015), pp. 117–171. ISSN: 0140-6736. DOI: 10.1016/S0140-6736(14)61682-2. URL: https://www.sciencedirect.com/science/article/pii/S0140673614616822 (visited on 12/30/2023).

[Niz22] Nusrat Binta Nizam, Shoyad Ibn Sabur Khan Nuhash, and Taufiq Hasan. "Hilbert-Envelope Features for Cardiac Disease Classification from Noisy Phonocardiograms". In: *Biomedical Signal Processing and Control* 78 (Sept. 2022), p. 103864. ISSN: 17468094. DOI: 10.1016/j.bspc.2022.103864. URL: https://linkinghub.elsevier.com/retrieve/pii/S1746809422003780 (visited on 01/03/2024).

[Nos19] Mehrdad Nosrati and Negar Tavassolian. "Accurate Doppler Radar-Based Cardiopulmonary Sensing Using Chest-Wall Acceleration". In: *IEEE Journal of Electromagnetics, RF and Microwaves in Medicine and Biology* 3.1 (Mar. 2019), pp. 41–47. ISSN: 2469-7257. DOI: 10.1109/JERM.2018.2879452. URL: https://ieeexplore.ieee.org/document/8520794 (visited on 12/25/2023).

[Par22] Junyung Park, Hyeon Seok Seok, Sang-Su Kim, and Hangsik Shin. "Photoplethysmogram Analysis and Applications: An Integrative Review". In: *Frontiers in Physiology* 12 (Mar. 1, 2022), p. 808451. ISSN: 1664-042X. DOI: 10.3389/fphys.2021.808451. URL: https://www.frontiersin.org/articles/10.3389/fphys.2021.808451/full (visited on 11/24/2023).

[Pat23] Giacomo Paterniani, Daria Sgreccia, Alessandro Davoli, Giorgio Guerzoni, Pasquale Di Viesti, Anna Chiara Valenti, Marco Vitolo, Giorgio M. Vitetta, and Giuseppe Boriani. "Radar-Based Monitoring of Vital Signs: A Tutorial Overview". In: *Proceedings of the IEEE* 111.3 (Mar. 2023), pp. 277–317. ISSN: 0018-9219, 1558-2256. DOI: 10.1109/JPROC.2023.3244362. URL: https://ieeexplore.ieee.org/document/10049295/ (visited on 04/21/2023).

[Per15] Tânia Pereira, Carlos Correia, and João Cardoso. "Novel Methods for Pulse Wave Velocity Measurement". In: *Journal of Medical and Biological Engineering* 35.5 (Oct. 2015), pp. 555–565. ISSN: 1609-0985, 2199-4757. DOI: 10.1007/s40846-015-

0086-8. URL: http://link.springer.com/10.1007/s40846-015-0086-8 (visited on 12/26/2023).

[Ram89] G. Ramachandran and M. Singh. "Three-Dimensional Reconstruction of Cardiac Displacement Patterns on the Chest Wall during the P, QRS and T-segments of the ECG by Laser Speckle Inteferometry". In: *Medical & Biological Engineering & Computing* 27.5 (Sept. 1989), pp. 525–530. ISSN: 0140-0118, 1741-0444. DOI: 10.1007/BF02441473. URL: http://link.springer.com/10.1007/BF02441473 (visited on 12/25/2023).

[Rot18] Gregory A Roth et al. "Global, Regional, and National Age-Sex-Specific Mortality for 282 Causes of Death in 195 Countries and Territories, 1980–2017: A Systematic Analysis for the Global Burden of Disease Study 2017". In: *The Lancet* 392.10159 (Nov. 2018), pp. 1736–1788. ISSN: 01406736. DOI: 10.1016/S0140-6736(18)32203-7. URL: https://linkinghub.elsevier.com/retrieve/pii/S0140673618322037 (visited on 08/18/2023).

[Rui09] Mariana Ruiz Villarreal. *Simplified Diagram of the Human Circulatory System in Anterior View*. 2009. URL: https://commons.wikimedia.org/wiki/File:Circulatory_System_en.svg.

[Sai16] Mehak Saini. "Proposed Algorithm for Implementation of Shannon Energy Envelope for Heart Sound Analysis". In: 7.1 (2016).

[Sch20a] Sven Schellenberger, Kilin Shi, Fabian Michler, Fabian Lurz, Robert Weigel, and Alexander Koelpin. "Continuous In-Bed Monitoring of Vital Signs Using a Multi Radar Setup for Freely Moving Patients". In: *Sensors* 20.20 (Oct. 15, 2020), p. 5827. ISSN: 1424-8220. DOI: 10.3390/s20205827. URL: https://www.mdpi.com/1424-8220/20/20/5827 (visited on 04/21/2023).

[Sch20b] Sven Schellenberger, Kilin Shi, Tobias Steigleder, Anke Malessa, Fabian Michler, Laura Hameyer, Nina Neumann, Fabian Lurz, Robert Weigel, Christoph Ostgathe, and Alexander Koelpin. "A Dataset of Clinically Recorded Radar Vital Signs with Synchronised Reference Sensor Signals". In: *Scientific Data* 7.1 (Sept. 8, 2020), p. 291. ISSN: 2052-4463. DOI: 10.1038/s41597-020-00629-5. URL: https://www.nature.com/articles/s41597-020-00629-5 (visited on 04/18/2023).

[She90] Andrew Sherwood(Chair), Michael T. Allen, Jochen Fahrenberg, Robert M. Kelsey, William R. Lovallo, and Lorenz J.P. van Doornen. "Methodological Guidelines for Impedance Cardiography". In: *Psychophysiology* 27.1 (1990), pp. 1–23. ISSN: 1469-

8986. DOI: 10.1111/j.1469-8986.1990.tb02171.x. URL: https://onlinelibrary.wiley.com/doi/abs/10.1111/j.1469-8986.1990.tb02171.x (visited on 11/26/2023).

[Shi18] Kilin Shi, Christoph Will, Tobias Steigleder, Fabian Michler, Robert Weigel, Christoph Ostgathe, and Alexander Koelpin. "A Contactless System for Continuous Vital Sign Monitoring in Palliative and Intensive Care". In: *2018 Annual IEEE International Systems Conference (SysCon)*. 2018 Annual IEEE International Systems Conference (SysCon). Vancouver, BC: IEEE, Apr. 2018, pp. 1–8. ISBN: 978-1-5386-3664-0. DOI: 10.1109/SYSCON.2018.8369507. URL: https://ieeexplore.ieee.org/document/8369507/ (visited on 07/31/2023).

[Shi19] Kilin Shi, Sven Schellenberger, Leon Weber, Jan Philipp Wiedemann, Fabian Michler, Tobias Steigleder, Anke Malessa, Fabian Lurz, Christoph Ostgathe, Robert Weigel, and Alexander Koelpin. "Segmentation of Radar-Recorded Heart Sound Signals Using Bidirectional LSTM Networks". In: *2019 41st Annual International Conference of the IEEE Engineering in Medicine and Biology Society (EMBC)*. 2019 41st Annual International Conference of the IEEE Engineering in Medicine and Biology Society (EMBC). July 2019, pp. 6677–6680. DOI: 10.1109/EMBC.2019.8857863. URL: https://ieeexplore.ieee.org/document/8857863 (visited on 11/29/2023).

[Shi20a] Kilin Shi, Sven Schellenberger, Fabian Michler, Tobias Steigleder, Anke Malessa, Fabian Lurz, Christoph Ostgathe, Robert Weigel, and Alexander Koelpin. "Automatic Signal Quality Index Determination of Radar-Recorded Heart Sound Signals Using Ensemble Classification". In: *IEEE Transactions on Biomedical Engineering* 67.3 (Mar. 2020), pp. 773–785. ISSN: 0018-9294, 1558-2531. DOI: 10.1109/TBME.2019.2921071. URL: https://ieeexplore.ieee.org/document/8731709/ (visited on 04/18/2023).

[Shi20b] Kilin Shi, Sven Schellenberger, Christoph Will, Tobias Steigleder, Fabian Michler, Jonas Fuchs, Robert Weigel, Christoph Ostgathe, and Alexander Koelpin. "A Dataset of Radar-Recorded Heart Sounds and Vital Signs Including Synchronised Reference Sensor Signals". In: *Scientific Data* 7.1 (Feb. 13, 2020), p. 50. ISSN: 2052-4463. DOI: 10.1038/s41597-020-0390-1. URL: https://www.nature.com/articles/s41597-020-0390-1 (visited on 04/18/2023).

[Spr15] David Springer, Lionel Tarassenko, and Gari Clifford. "Logistic Regression-HSMM-based Heart Sound Segmentation". In: *IEEE Transactions on Biomedical Engineering*

(2015), pp. 1–1. ISSN: 0018-9294, 1558-2531. DOI: 10.1109/TBME.2015.2475278. URL: http://ieeexplore.ieee.org/document/7234876/ (visited on 07/30/2023).

[Spr16] David B. Springer, Thomas Brennan, Ntobeko Ntusi, Hassan Y. Abdelrahman, Liesl J. Zühlke, Bongani M. Mayosi, Lionel Tarassenko, and Gari D. Clifford. "Automated Signal Quality Assessment of Mobile Phone-Recorded Heart Sound Signals". In: *Journal of Medical Engineering & Technology* 40.7-8 (2016), pp. 342–355. ISSN: 1464-522X. DOI: 10.1080/03091902.2016.1213902. pmid: 27659352.

[Ste14] Jan Steffel and Thomas Lüscher. *Herz-Kreislauf*. Springer-Lehrbuch. Berlin, Heidelberg: Springer Berlin Heidelberg, 2014. ISBN: 978-3-642-55112-3. DOI: 10.1007/978-3-642-55112-3. URL: http://link.springer.com/10.1007/978-3-642-55112-3 (visited on 11/26/2023).

[Sys13] BIOPAC Systems. *SS2L ELECTRODE LEAD SET*. Dec. 19, 2013. URL: https://www.biopac.com/wp-content/uploads/SS2L.pdf (visited on 12/31/2023).

[Sys18] BIOPAC Systems. *PULSE PHOTOPLETHYSMOGRAM TRANSDUCERS*. Apr. 24, 2018. URL: https://www.biopac.com/wp-content/uploads/Pulse-Transducer.pdf (visited on 12/31/2023).

[Sys21] BIOPAC Systems. *SS31LA NONINVASIVE IMPEDANCE CARDIOGRAPHY MODULE*. Dec. 6, 2021. URL: https://www.biopac.com/wp-content/uploads/SS31LA.pdf (visited on 12/31/2023).

[Sys22a] BIOPAC Systems. *MP ACQUISITION UNITS*. Aug. 4, 2022. URL: https://www.biopac.com/wp-content/uploads/MP36-MP46.pdf (visited on 12/31/2023).

[Sys22b] BIOPAC Systems. *TSD108A AND SS17LA PHYSIOLOGICAL SOUNDS TRANSDUCER (CONTACT MICROPHONE)*. Mar. 11, 2022. URL: https://www.biopac.com/wp-content/uploads/Contact-Microphone.pdf (visited on 12/31/2023).

[Sys23] BIOPAC Systems. *AcqKnowledge 5 Software Guide*. May 10, 2023. URL: https://www.biopac.com/wp-content/uploads/AcqKnowledge-5-Software-Guide.pdf (visited on 12/31/2023).

[Van07] Rutger W. Van Der Meer, Michaela Diamant, Jos J. M. Westenberg, Joost Doornbos, Jeroen J. Bax, Albert De Roos, and Hildo J. Lamb. "Magnetic Resonance Assessment of Aortic Pulse Wave Velocity, Aortic Distensibility, and Cardiac Function in Uncomplicated Type 2 Diabetes Mellitus". In: *Journal of Cardiovascular Magnetic Resonance* 9.4 (July 2007), pp. 645–651. ISSN: 1097-6647. DOI: 10.1080/10976640601093703.

URL: http://www.informaworld.com/openurl?genre=article&doi=10.1080/10976640601093703&magic=crossref%7C%7CD404A21C5BB053405B1A640AFFD44AE3 (visited on 12/27/2023).

[Vin13] Gabor Vinci, Stefan Lindner, Francesco Barbon, Sebastian Mann, Maximilian Hofmann, Alexander Duda, Robert Weigel, and Alexander Koelpin. "Six-Port Radar Sensor for Remote Respiration Rate and Heartbeat Vital-Sign Monitoring". In: *IEEE Transactions on Microwave Theory and Techniques* 61.5 (May 2013), pp. 2093–2100. ISSN: 0018-9480, 1557-9670. DOI: 10.1109/TMTT.2013.2247055. URL: http://ieeexplore.ieee.org/document/6473856/ (visited on 12/27/2023).

[Vla11] Charalambos Vlachopoulos, Michael O'Rourke, and Wilmer W. Nichols. *McDonald's Blood Flow in Arteries: Theoretical, Experimental and Clinical Principles*. CRC Press, July 29, 2011. 758 pp. ISBN: 978-1-4441-2878-9. Google Books: byrSBQAAQBAJ.

[Wan15] Zhen Wang, Yong Yang, Li-jun Yuan, Jie Liu, Yun-you Duan, and Tie-sheng Cao. "Noninvasive Method for Measuring Local Pulse Wave Velocity by Dual Pulse Wave Doppler: In Vitro and In Vivo Studies". In: *PLOS ONE* 10.3 (Mar. 18, 2015). Ed. by Yan Li, e0120482. ISSN: 1932-6203. DOI: 10.1371/journal.pone.0120482. URL: https://dx.plos.org/10.1371/journal.pone.0120482 (visited on 12/26/2023).

[Wil17a] Christoph Will, Kilin Shi, Sven Schellenberger, Tobias Steigleder, Fabian Michler, Robert Weigel, Christoph Ostgathe, and Alexander Koelpin. "Local Pulse Wave Detection Using Continuous Wave Radar Systems". In: *IEEE Journal of Electromagnetics, RF and Microwaves in Medicine and Biology* 1.2 (Dec. 2017), pp. 81–89. ISSN: 2469-7249, 2469-7257. DOI: 10.1109/JERM.2017.2766567. URL: https://ieeexplore.ieee.org/document/8082495/ (visited on 04/18/2023).

[Wil17b] Christoph Will, Kilin Shi, Robert Weigel, and Alexander Koelpin. "Advanced Template Matching Algorithm for Instantaneous Heartbeat Detection Using Continuous Wave Radar Systems". In: *2017 First IEEE MTT-S International Microwave Bio Conference (IMBIOC)*. 2017 First IEEE MTT-S International Microwave Bio Conference (IMBIOC). Gothenburg, Sweden: IEEE, May 2017, pp. 1–4. ISBN: 978-1-5386-1713-7. DOI: 10.1109/IMBIOC.2017.7965797. URL: http://ieeexplore.ieee.org/document/7965797/ (visited on 04/21/2023).

[Wil18] Christoph Will, Kilin Shi, Sven Schellenberger, Tobias Steigleder, Fabian Michler, Jonas Fuchs, Robert Weigel, Christoph Ostgathe, and Alexander Koelpin. "Radar-Based Heart Sound Detection". In: *Scientific Reports* 8.1 (July 26, 2018), p. 11551.

ISSN: 2045-2322. DOI: 10.1038/s41598-018-29984-5. URL: https://www.nature.com/articles/s41598-018-29984-5 (visited on 04/18/2023).

[Wol97] H. H. Woltjer, H. J. Bogaard, and P. M. J. M. De Vries. "The Technique of Impedance Cardiography". In: *European Heart Journal* 18.9 (Sept. 1, 1997), pp. 1396–1403. ISSN: 0195-668X, 1522-9645. DOI: 10.1093/oxfordjournals.eurheartj.a015464. URL: https://academic.oup.com/eurheartj/article-lookup/doi/10.1093/oxfordjournals.eurheartj.a015464 (visited on 12/24/2023).

[Wu21] Hao Wu, Ganguang Yang, Kanhao Zhu, Shaoyu Liu, Wei Guo, Zhuo Jiang, and Zhuo Li. "Materials, Devices, and Systems of On-Skin Electrodes for Electrophysiological Monitoring and Human–Machine Interfaces". In: *Advanced Science* 8.2 (Jan. 2021), p. 2001938. ISSN: 2198-3844, 2198-3844. DOI: 10.1002/advs.202001938. URL: https://onlinelibrary.wiley.com/doi/10.1002/advs.202001938 (visited on 12/30/2023).

[Yao22] Yang Yao, Shuran Zhou, Jordi Alastruey, Liling Hao, Stephen E. Greenwald, Yuelan Zhang, Lin Xu, Lisheng Xu, and Yudong Yao. "Estimation of Central Pulse Wave Velocity from Radial Pulse Wave Analysis". In: *Computer Methods and Programs in Biomedicine* 219 (June 2022), p. 106781. ISSN: 01692607. DOI: 10.1016/j.cmpb.2022.106781. URL: https://linkinghub.elsevier.com/retrieve/pii/S0169260722001675 (visited on 12/27/2023).